MACHINE LEARNING BASED HIGH-THROUGHPUT PHENOTYPING FRAMEWORK FOR CROP YIELD PREDICTION USING UNMANNED AIRCRAFT SYSTEMS

by

Akash Ashapure

A Dissertation

Submitted to the Faculty of Purdue University

In Partial Fulfillment of the Requirements for the degree of

Doctor of Philosophy

Lyles School of Civil Engineering

West Lafayette, Indiana

December 2021

THE PURDUE UNIVERSITY GRADUATE SCHOOL

STATEMENT OF COMMITTEE APPROVAL

Dr. Jinha Jung, Chair

Lyles School of Civil Engineering

Dr. Melba M. Crawford

Lyles School of Civil Engineering

Dr. Ayman F. Habib

Lyles School of Civil Engineering

Dr. Murilo M. Maeda

Texas A&M AgriLife Extension, Lubbock, TX

Approved by:

Dr. Dulcy Abraham

Dedicated to my Advisor Dr. Jinha Jung

for his immeasurable support and having faith in me

ACKNOWLEDGMENTS

I have many people to thank for helping me get through this dissertation. First of all, I express my profound appreciation to my advisor, Dr. Jinha Jung, for his unrelenting patience and encouragement. It has been both a pleasure and a privilege for me to work with him. I would not have made it without his unwavering support, helpful advice, and constructive criticism at every stage of this study.

I wish to thank Dr. Melba M. Crawford, Dr. Ayman Habib, and Dr. Murilo M. Maeda for serving on my dissertation committee and providing valuable suggestions. The members of the Texas A&M Agrilife Research Center at Corpus Christi, Dr. Juan Landivar-Bowles, Dr. Anjin Chang, Dr. Mahendra Bhandari, and Dr. Nothabo Dube, who have contributed immensely to my personal and professional time at Texas A&M University-Corpus Christi and later in Purdue University. The group has been a source of friendships as well as good advice and collaboration. I would also like to thank Dr. Dulcy M. Abraham and Ms. Jenny Ricksy for their extended support. Time has flown by rather quickly. But some of my fondest memories will remain with me forever. I will cherish the pleasurable company of my friends, Dr. Sungchan Oh, Joshua Carpenter, Hunsoo Song, Tarutal Ghosh Mondal, Shivaram Gopal, Sri Tapaswi Nori, among many others, who were indeed like my family away from home.

I will forever be grateful to my parents and family for their years of sacrifice and continued support, which has made immense contributions to my life. This dissertation stands as a testament to their unfailing love and blessings. Finally, I would like to extend my sincere thanks to one and all who, directly or indirectly, have lent a hand in this venture.

TABLE OF CONTENTS

LIST OF TABLES

LIST OF FIGURES

LIST OF ABBREVIATIONS

UAS:	Unmanned Aircraft Systems
HTTP:	High Throughput Phenotyping
ANN:	Artificial Neural Network
SVR:	Support Vector Regression
RFR:	Random Forest Regression
RNN:	Recurrent Neural Network
LSTM:	Long Short-term Memory
CC:	Canopy Cover
CH:	Canopy Height
CV:	Canopy Volume
NDVI:	Normalized Difference Vegetation Index
ExG:	Excess Greenness Index
RGBVI:	Red Green Blue Vegetation Index
MGRVI:	Modified Green Red Vegetation Index
BC:	Boll Count
BS:	Boll Size
BV:	Boll Volume
CNN:	Convolutional Neural Network
VI:	Vegetation Index
NT:	No-Tillage
CT:	Conventional-Tillage
GPS:	Global Positioning System
GCP:	Ground Control Point
PPK:	Post Processed Kinematic

ABSTRACT

Estimating crop yield is essential to ensure agricultural stability, economic viability, and global food security. Provided with accurate crop yield estimation before harvest, farmers, breeders, and agriculture researchers can perform crop evaluation, genotype selection, and maximize yield by timely intervention. Remote sensing is often used to provide information about important canopy state variables for crop yield estimation. However, until recently, a critical bottleneck in such research was the lack of high-throughput sensing technologies for effective and rapid evaluation of expressed phenotypes under field conditions for holistic data-driven decision making. Recent years have witnessed enormous growth in the application of unmanned aircraft systems (UAS) for precision agriculture. UAS has the potential to provide information on crops quantitatively and, above all, nondestructively. This dissertation aims at utilizing UAS data to develop a machine learning based high-throughput phenotyping framework for crop yield estimation. In this research, plant parameters such as canopy height (CH), canopy cover (CC), canopy volume (CV), normalized difference vegetation index (NDVI), and excessive greenness index (ExG) were extracted from fine spatial resolution UAS based RGB and multispectral images collected weekly throughout the growing season. Initially, a comparative study was conducted to compare two management practices in cotton: conventional tillage (CT) and no-tillage (NT). This initial study was designed to test the reliability of the UAS derived plant parameters, and results revealed a significant difference in cotton growth under CT and NT. Unlike manual measurements, which rely on limited samples, UAS technology provided the capability to exploit the entire population, which makes UAS derived data more robust and reliable.

Additionally, an inter-comparison study was designed to compare CC derived from RGB and multispectral data over multiple flights during the growing season of the cotton crop. This study demonstrated that using a morphological closing operation after the thresholding significantly improved the RGB-based CC modeling. A CC model that uses a multispectral sensor is considered more stable and accurate in the literature (Roth and Streit, 2018; Xu et al., 2019). In contrast, the RGB-based CC model is unstable and fails to identify canopy pixels when cotton

leaves change color after canopy maturation. The proposed RGB-based CC model provides an affordable alternative to the multispectral sensors that are more sensitive and expensive.

After assessing the reliability of UAS derived canopy parameters, a novel machine learning framework was developed for cotton yield estimation using multi-temporal UAS data. The proposed machine learning model takes three types of crop features derived from UAS data to predict the yield. The three types of crop features are multi-temporal canopy features, non-temporal features (cotton boll count, boll size, boll volume), and irrigation status. The developed model provided a high coefficient of determination (R^2 ~ 0.9). Additionally, redundant features were removed using correlation analysis, and the relative significance of each input feature was determined using sensitivity analysis. Finally, an experiment was performed to investigate how early the model can accurately predict yield. It was observed that even at 70 days after planting, the model predicted yield with reasonable accuracy (R^2 of 0.71 over test set). This study reveals that UAS derived multi-temporal data along with non-temporal and qualitative data can be combined within a machine learning framework to provide a reliable crop yield estimation.

UAS technology is proven to be robust and reliable. It efficiently works over small-size research fields or breeding trial fields. However, extensive aerial coverage using UAS is not practically feasible. Alternatively, satellite images have the advantage of covering a vast area, but they provide coarser spatial resolution data. To overcome the limitation of UAS and satellite sensors, this study explored deep learning-based methodologies to incorporate UAS derived canopy attributes as additional information to improve the satellite-based yield estimation. It was accomplished through cross-task knowledge transfer architecture and modality hallucination architecture. The main idea of this approach is to combine a multi-temporal satellite-based representation with an additional, or complementary UAS derived representation to improve crop yield estimation so that the models can predict yield without utilizing UAS derived representation at the test time. A significant improvement in the prediction accuracy was observed using cross-task knowledge transfer and modality hallucination architecture. Additionally, the generalization capability of the proposed models was demonstrated by training on one experiment field and predicting crop yield for another field.

1. INTRODUCTION

1.1 Motivation

Crops are susceptible to management practices and environmental conditions (Swain et al., 2007). Consequently, it is critical for agricultural researchers, breeders, or farmers to identify where variations exist in crops in a timely fashion to take necessary action accordingly. Manual measurements of agronomic characteristics are labor-intensive and time-consuming. Thus, a system that could help stabilize or potentially help increase agricultural productivity while mediating the overall impact on the environment would be an asset to society (Zhang and Kovacs, 2012). As a solution, remote-sensing technology offers a more efficient way to obtain a large-scale mapping of plant attributes. Specifically, numerous studies have demonstrated that remote sensing has been successfully providing a means to obtain extensive spatial information from the landscape at a global scale (Davi et al., 2006; Hu et al., 2007; Lamonaca et al., 2008; Pellikka et al., 2009; Propastin and Panferov, 2013). Early research done in this direction includes remote sensing data acquired using satellites and manned aircrafts. However, the spatial resolution and turnaround time of the satellite data often fails to meet regional or local objectives. Airborne platforms could obtain scale-appropriate remote sensing data, but they are often costly, preventing high temporal resolution data collection. Due to technological advances, recent years have witnessed enormous growth in unmanned aircraft systems (UAS) in various applications, including precision agriculture. Unlike ground-based high-throughput phenotyping (HTP), UAS can quickly cover an entire experiment, providing a rapid assessment of the crop while minimizing the effect of change in environmental conditions, such as wind speed, rain, cloud cover, and sunlight. UAS can provide high spatial and temporal resolution, providing the capability of generating insightful information for numerous applications, such as crop disease identification, crop growth modeling, and crop yield estimation.

Crop yield prediction is critical for farmers, breeders, and agriculture scientists, especially in the early stages, as it could inform crop management strategies and help in crop evaluation. An enormous amount of research is available in the literature regarding conventional ground sensing

methods to estimate crop yield (Feng et al., 2018). However, conventional methods are exhaustive, time-consuming, labor-intensive, and often not scalable due to resource availability constraints. In the literature, satellite remote sensing data have been extensively utilized for crop yield estimation (Ferencz et al., 2004; Hunt et al., 2019; Meng et al., 2019; Novelli et al., 2019; Sayago and Bocco, 2018; Singh et al., 2002). Though satellite remote sensing data is valuable for extensive areal coverage, spatial resolution is still a concern for many precision agriculture applications. The ground yield maps for breeding trials generally require higher spatial resolution. Moreover, optical satellite images may suffer from occlusion by clouds, and their revisit time is also not flexible.

Recent developments in exploiting UAS data for yield estimation have revealed that UAS-based remote sensing has the potential to accurately estimate crop yield (Weiss et al., 2020). Recent years have witnessed the emergence of machine learning regression models such as artificial neural networks (ANN), support vector regression (SVR), random forest regression (RFR), and Gaussian process regression. These models have been successfully deployed to determine an empirical relationship between crop yield and crop canopy feature-set derived from UAS containing canopy attributes, vegetation indices (Gandhi et al., 2016; Gopal and Bhargavi, 2019; Yu et al., 2016). Recently, deep learning models are also gaining popularity for accurate crop yield prediction (Khaki et al., 2019; Khaki et al., 2020; Kim et al., 2019; Tri et al., 2017; Wang et al., 2018; You et al., 2017). However, recent deep learning-based methodologies involve utilizing multi-year weather data along with coarser spatial resolution satellite data for yield prediction over a large area. Moreover, the success of deep learning-based yield estimation models is mainly dependent on a large number of training samples, which makes them unsuitable for small-scale experiments with limited training samples.

Early research utilizing UAS driven crop canopy feature-sets mostly demonstrated correlation of crop yield with reflectance in the spectral bands and vegetation indices derived from UAS based sensors (Nebiker et al., 2016; Stroppiana et al., 2015; Zhou et al., 2017). Later, UAS based image-driven crop canopy attributes, such as canopy height, canopy volume, and canopy cover, were also utilized to estimate crop yield (Feng et al., 2018; Stanton et al., 2017). These studies used a single or relatively few regression parameters for crop yield estimation. Exploring

the full potential of UAS derived multi-temporal canopy attributes and vegetation indices for crop yield estimation is unprecedented in the literature. Moreover, it is also essential to investigate how early crop yield estimation can be successfully made in the crop growing season. Information is scarce in the literature regarding the suitability of UAS derived various canopy attributes as input features for machine learning modeling to estimate crop yield. Additionally, the reliability of UAS derived canopy attributes is also under question. Furthermore, one of the vital canopy attributes: canopy cover needs a thorough investigation pertaining to finding the most accurate canopy cover estimation method. This dissertation aims at filling these research gaps by conducting a reliability assessment of canopy attributes over different cropping systems, conducting a comparative study for various RGB and multi-spectral based CC estimation, and investigating the suitability of various canopy attributes for machine learning based crop yield estimation.

As mentioned earlier, crop yield prediction before harvest is essential for farmers, breeders, and researchers for improved field management, crop performance evaluation, crop marketing, and genotype selection. However, crop yield estimation has a broader impact when applied to larger areas. Crop yield estimation at national and regional levels is an important metric for the decision-makers, such as crop insurance companies, food companies, and government agencies, to help ensure agricultural stability, economic viability, and global food security. Despite the need for large area crop yield estimation, limited battery, flight time, and large size of the collected data prevent UAS from covering large areas. On the other hand, satellite data cover a larger area but provide coarser spatial and temporal resolution than UAS imagery. As mentioned earlier, satellite remote sensing data have been extensively utilized for crop yield estimation, and an ample number of studies are found in the literature using UAS derived data for yield estimation. However, there is no existing literature combining UAS and satellite data for yield estimation. This dissertation also aims at addressing this research gap by combining UAS's ability to provide precise high spatial resolution data with the extensive areal coverage provided by satellite data to estimate crop yield.

1.2 Research objective

This research is based on the observation that there is an increasing need for accurate and timely crop yield estimation. Therefore, the overall goal of this research is to develop new remote sensing-based methods for crop yield estimation. The specific objectives of this dissertation are as follows:

The first objective is to utilize UAS data collected over the season for crop yield estimation, which includes developing a novel machine learning framework for yield estimation, and determining the optimal input feature set, along with the relative significance of each variable in the input feature set. Additionally, this study aims to determine how early crop yield estimation can be achieved in the growing season.

UAS efficiently works over small-size research or breeding trial fields. However, extensive aerial coverage is not practically feasible. Nevertheless, satellite images cover a vast area but provide coarser spatial resolution. To overcome these limitations, the second objective of this dissertation is to combine UAS and satellite data for large-area crop yield estimation. Considering the limited availability of UAS derived information, applying traditional data fusion models is not feasible. This study investigates deep learning methodologies that eliminate the need for UAS data during test time to overcome this challenge.

1.3 Overview of the dissertation

The main objective of this dissertation is to develop new remote sensing-based methods for crop yield estimation. To achieve this research objective, first, the reliability of UAS-derived canopy parameters was tested; subsequently, a comparative study of canopy cover was performed; and later, a method for determining crop yield from UAS was proposed. Finally, the knowledge acquired through the preceding three tasks was leveraged to investigate machine learning models for integrating satellite and UAS data for large-area crop yield estimation.

Chapter 2 determines the reliability of UAS-derived canopy parameters through a project using multi-temporal UAS data for comparing two management practices in cotton, Conventional-Tillage, and No-Tillage (Ashapure et al., 2019b).

Chapter 3 compares RGB and multispectral sensor-based cotton canopy cover models and proposes an RGB-based canopy cover estimation methodology, which provides an affordable alternative to more sensitive and expensive multispectral sensors (Ashapure et al., 2019a).

In chapter 4, a machine learning based cotton yield estimation framework using multi-temporal UAS data is proposed. In addition to building the machine learning-based framework, this chapter tests how early in the season the crop yield can be reliably predicted and also determines the relative significance of individual canopy features in the prediction model (Ashapure et al., 2020a).

Finally, in Chapter 5, a deep learning-based modality fusion methodology is proposed based on cross task knowledge transfer and modality hallucination to utilize UAS-derived canopy parameters as side information to improve multi-temporal satellite-based crop yield prediction. Proposed models eliminate the need for UAS data during the test time.

Finally, a summary and conclusion are provided.

2. UAS BASED CROPPING SYSTEM EFFECT ASSESSMENT

2.1 Background

The main focus of this dissertation is to develop a machine learning based high-throughput phenotyping framework for crop yield prediction using UAS derived plant parameters such as canopy height (CH), canopy cover (CC), canopy volume (CV), and vegetation indices. However, assessing the reliability of these plant parameters is important before utilizing them as input to the yield prediction models. To investigate the reliability of the UAS derived plant parameters, this study aims to develop a framework to detect conventional tillage (CT) and no-tillage (NT) cropping system effects on cotton growth and development using multi-temporal UAS data. Conventional tillage is the most commonly adopted management practice in U.S. agriculture (Triplett and Dick, 2008). It consists of tilling the soil before planting to control weeds and primarily creating seedbeds for uniform crop establishment. However, the development of new technology and the introduction of new efficient herbicides enabled the adoption of alternate management practices, such as reduced tillage and no-tillage systems. The latter consists of planting crops in unprepared soil with at least 30% mulch cover (Giller et al., 2015). NT systems capture and store water more efficiently, reduce erosion and degradation of soil structure, decrease input costs and, consequently, sustain long-term crop production (Pittelkow et al., 2015b; Triplett and Dick, 2008). Short-term impacts of the NT systems on crop yields are still considered variable. A solid understanding of the factors affecting productivity is needed to support evidence-based management decisions. Therefore, there is a need to assess the performance of CT and NT systems.

Content of this chapter is published as follows: Ashapure, A., Jung, J., Yeom, J., Chang, A., Maeda, M., Maeda, A., & Landivar, J. (2019). A novel framework to detect conventional tillage and no-tillage cropping system effect on cotton growth and development using multi-temporal UAS data. *ISPRS Journal of Photogrammetry and Remote Sensing*, *152*, 49-64.

2.1.1 Scope and contribution

It is vital to extend the application of UAS derived plant parameters to quantify agronomic differences in crop plants under different cropping systems, which will help agriculture scientists, farmers, and breeders make evidence-based management decisions. Traditionally, they rely on taking manual measurements of agronomic characteristics, which is labor-intensive and time-consuming. Moreover, experiments utilizing manual measurements rely on only a few samples, leading to statistical uncertainty depending on the sample size. As a solution, remote-sensing technology offers a more efficient way to obtain a large-scale mapping of plant parameters. High-throughput, automated phenotyping approaches for plant parameters are required to facilitate the assessment of large breeding populations, or precision agriculture approaches. UAS has emerged to serve this need by providing unprecedented spatial, spectral, and temporal resolution data (Roth et al., 2018; Singh and Frazier, 2018). An ample amount of research can be found in the literature exploring UAS derived canopy parameters (Calders et al., 2015; Chianucci et al., 2016; Hassan et al., 2018; Lucieer et al., 2014; Stanton et al., 2017). However, there is no literature attempting to quantify agronomic differences in crop plants under different cropping systems using UAS data. The present study aims to fill this gap by proposing a novel framework to use multi-temporal UAS data to compare two management practices in cotton, CT, and NT. Furthermore, the main contribution of the present study is to assess the reliability of UAS derived plant canopy parameters to be used as input to the yield estimation model.

2.2 Study area, sensors, and platforms

The study was conducted at the Texas A&M AgriLife Research and Extension Center at Corpus Christi, Texas (latitude 27°46’59” N, longitude 97°34’13” W) during the 2017 growing season. The cotton field considered in the study was part of a larger experiment as presented in Figure 2.2, which was initiated in 2011. The experiment was designed to study the long-term effects of NT on cotton and sorghum, where cotton and sorghum were rotated every year. Soil types in the study site are Victoria Clay series soils (Victoria-Lattas-Clareville). Cotton plots were established in a split-plot design with CT ($CT_1 – CT_4$) and NT ($NT_1 – NT_4$) practices as replications

in a non-irrigated field (Figure 2.1) where treatment within CT and NT replications was consistent. Three cotton varieties (Deltapine, 1044, and B2RF) were planted on March 25, 2017, and harvested on August 1, 2017. Each replication consisted of sixteen rows, 55m long and 0.97m apart. The total area of the experimental field was approximately 2.25 acres. Provided the experimental field was in a coastal area, wind speed and rain were the potential factors to be considered before every flight. Flights were conducted between 10:00 AM to 2:00 PM. The temperature variation throughout the growing season varies between 79°F to 96°F with an average humidity of 76%. Average monthly rainfall in the region ranges between 50 mm and 90 mm during the growing season (NWS, 2016).

The experimental field was divided into approximately one square meter grids to extract various plant canopy parameters. Any grids that did not contain any canopy and the grids around edges of the test field were removed from the analyses for fair comparison of cropping systems effects. Both RGB (Red, Green, and Blue) and MS (multispectral) sensors were used for this study. DJI Phantom 4 Pro (SZ DJI Technology Co., Ltd., Shenzhen, China) was used for RGB data collection. The weight of this UAS is 1.4 kg with a flight endurance of up to 30 minutes in mild weather conditions. It is equipped with a 3-axis gimbal-stabilized RGB sensor with 20 megapixels resolution, with a field of view (FOV) of 74°. Multispectral data was captured using a multirotor platform, DJI Matrice 100 (DJI, Shenzhen, China). The weight of this UAS is 2.4 kg with a flight endurance of up to 25 minutes in mild weather conditions. A multispectral sensor, SlantRange 3p (Slantrange Inc, San Diego, CA, USA), was mounted on the UAV. SlantRange 3p sensor has a resolution of 1280 × 1024, 4.8 micro meter pixel size, 12 mm focal length, and 28° FOV. The sensor is equipped with an integrated solar spectrometer for frame-to-frame radiometrically accurate reflectance measurements. The sensor captures four spectral bands, including green, red, red-edge, and near-infrared bands (peak wavelengths are presented in Table 2.1).

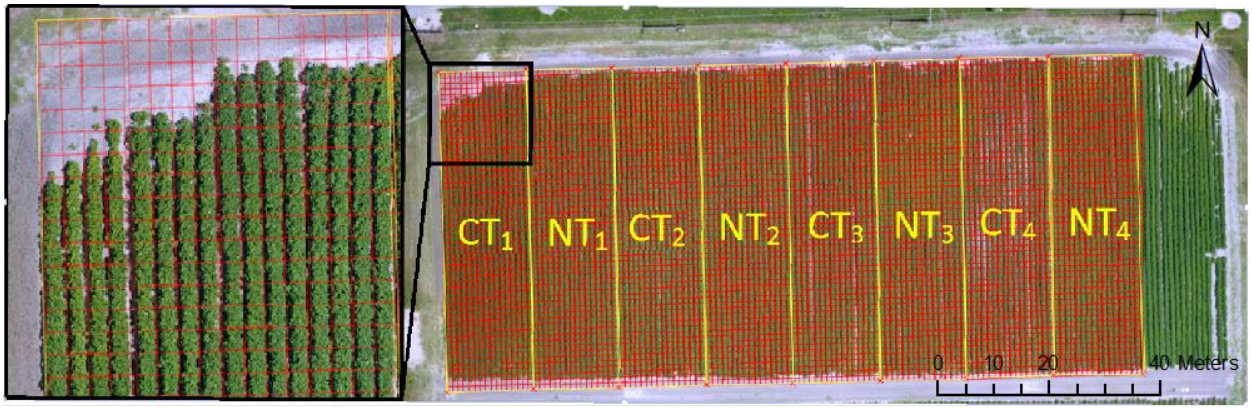

Figure 2.1. Experimental field setup consisted of cotton planted under Conventional-tillage (CT_1~ CT_4) and No-Tillage (NT_1~NT_4) treatments. Insert highlights grid system (1m x 1m) applied to the entire test field for data extraction. Experimental field setup is presented with RGB orthomosaic of the study area on June 7, 2017.

Figure 2.2. Distribution of ground control points (GCPs) on the larger experimental field comprising of alternate cotton and sorghum plots. The cotton plot considered in this experiment is highlighted by the dotted yellow rectangle.

Table 2.1. Peak wavelength and FWHM for bands present in SlantRange 3p sensor

SlantRange 3p sensor band	Peak wavelength (nm)	FWHM (nm)
Green	560	40
Red	655	35
Red-edge	710	20
Near-infrared	830	110

Table 2.2 presents flight specifications for both RGB and multispectral data. UAS considered in this study were equipped with a consumer-grade Global Positioning System (GPS) which did not have satisfactory location accuracy for aerial mapping applications. To overcome this problem, 14 well-distributed permanent ground control points (GCPs) with high reflectance were installed over the study area (Figure 2.2). GCPs were surveyed every time the UAS data was collected using a dual-frequency, post-processed kinematic (PPK) GPS, model 20Hz V-Map Air (Micro Aerial Project L.L.C., Gainesville, FL). After each flight, the collected raw UAS data was processed using Agisoft Photoscan Pro software (Agisoft LLC, St. Petersburg, Russia). The software uses structure-from-motion to generate DSM and orthomosaic. Unlike traditional photogrammetry, SfM uses information extracted from multiple overlapped (~80-90%) images to generate a 3D point cloud without the need for precise camera calibration parameters (Westoby et al., 2012). In SfM processing, key points from overlapping images are initially identified using a feature matching algorithm such as scale-invariant feature transform (SIFT)(Lowe, 2004). Using bundle block adjustment, interior and exterior orientation parameters are computed by providing the key points identified using SIFT and coordinates for GCPs. Further, 3D coordinates of the matching points are computed. Now that the camera positions and orientations are known, multi-view stereo (MVS) processing is used to systematically step through the images and use the principles of stereo viewing to increase the number of points, creating the dense point cloud. After densification of the point cloud, a digital surface model (DSM) was generated. Finally, the DSM is used to project every image pixel to generate an orthorectified mosaic or an orthomosaic. Absolute georeferencing accuracy of the UAS generated DSM and orthomosaics was not computed. However, the relative accuracy of multi-temporal data was observed to be centimeter-level on visual inspection, i.e., 2 cm in planimetry and 3 cm in altimetry.

Canopy attributes and vegetation indices computation procedure is presented in Appendix A.1. Manual height measurements were also taken throughout the season every week to validate UAS-based CH data collection (ground-truthing). A ruler was used to measure the cotton plant height (apex height). The ground measured height was presented for all the individual replications by averaging measurements from the heights of ten random plants per row collected only from two middle rows of the replication.

Table 2.2. UAS data collection timeline and sensor-wise flight specifications.

Date	Flight Altitude (RGB)	Flight Altitude (Multispectral)	Overlap (RGB)	Overlap (Multispectral)	Spatial Resolution, RGB (cm)	Spatial Resolution, multispectral (cm)
20 May, 2017	30m	40m	80%	60%	0.84	1.69
30 May, 2017	30m	40m	80%	60%	0.76	1.58
07 June, 2017	30m	40m	80%	60%	0.80	1.58
14 June, 2017	30m	40m	80%	60%	0.79	1.65
19 June, 2017	30m	40m	80%	60%	0.78	1.62
05 July, 2017	20m	40m	80%	60%	0.51	1.60
10 July, 2017	30m	40m	80%	60%	0.83	1.64
18 July, 2017	30m	40m	80%	60%	0.82	1.63

2.3 Methodology

Four canopy parameters were used to compare the effects of CT and NT cropping systems over the entire growing season- canopy height (CH), canopy cover (CC), canopy volume (CV), and normalized difference vegetation index (NDVI). These parameters were computed using the georeferenced orthomosaics, and digital surface models (DSM) generated from data captured using UAS every week (a detailed parameter computation procedure is presented in section A.1). Canopy parameters were obtained grid-wise, and the average of all the grids per cropping system was used to compare the cropping systems. A one-tailed test hypothesis was designed to compare cropping system effects. The hypothesis used Z statistics (Equation 2.1) with a 95% confidence interval. The null hypothesis (H_0) suggests that NT is not significantly greater than CT, and the alternate hypothesis (H_a) suggests that NT is significantly greater than CT at $\alpha = 0.05$.

$$Z = \frac{o_n - o_t}{\sqrt{\sigma_{o_n}^2 + \sigma_{o_t}^2}} \quad , \tag{2.1}$$

Where $Z \geq 1.645$ indicates a significant difference at 0.05 significance level, o_n and o_t represent the average NT and CT measurements per grid respectively and α the confidence level.

2.4 Results and discussion

2.4.1 Treatment effects on plant parameters

It can be observed in Figure 2.3 and Figure 2.4 that CH values steadily increased since the first date of data collection on May 20, reaching a plateau on June 14. A decrease of two centimeters in CH under NT and four centimeters in CH under CT was observed after June 14, which highlights one of the limitations of the current technology and methodology in resolving plant height once the plant canopy starts senescing (Figure 2.4). One of the reasons for the decrease in CH was the decrease in the 3D point cloud density, which makes it difficult to detect the actual highest point in the plant. Moreover, wind also contributes to the minor inaccuracies in height measurements. Lodging could also be a factor late in the season due to the increasing weight (cotton bolls) during the growing season. However, this is not seen every season/year, and it is highly dependent on environmental and crop conditions. Average CH measured for both CT and NT treatments indicated that plants growing under the NT treatment were relatively taller and that the difference steadily increased from two centimeters on May 30, 2017, to ten centimeters on July 10, 2017. Except for the first data collection date (May 20, 2017), statistical analyses confirmed that NT plants were significantly taller than those grown under the CT treatment (Table 2.3).

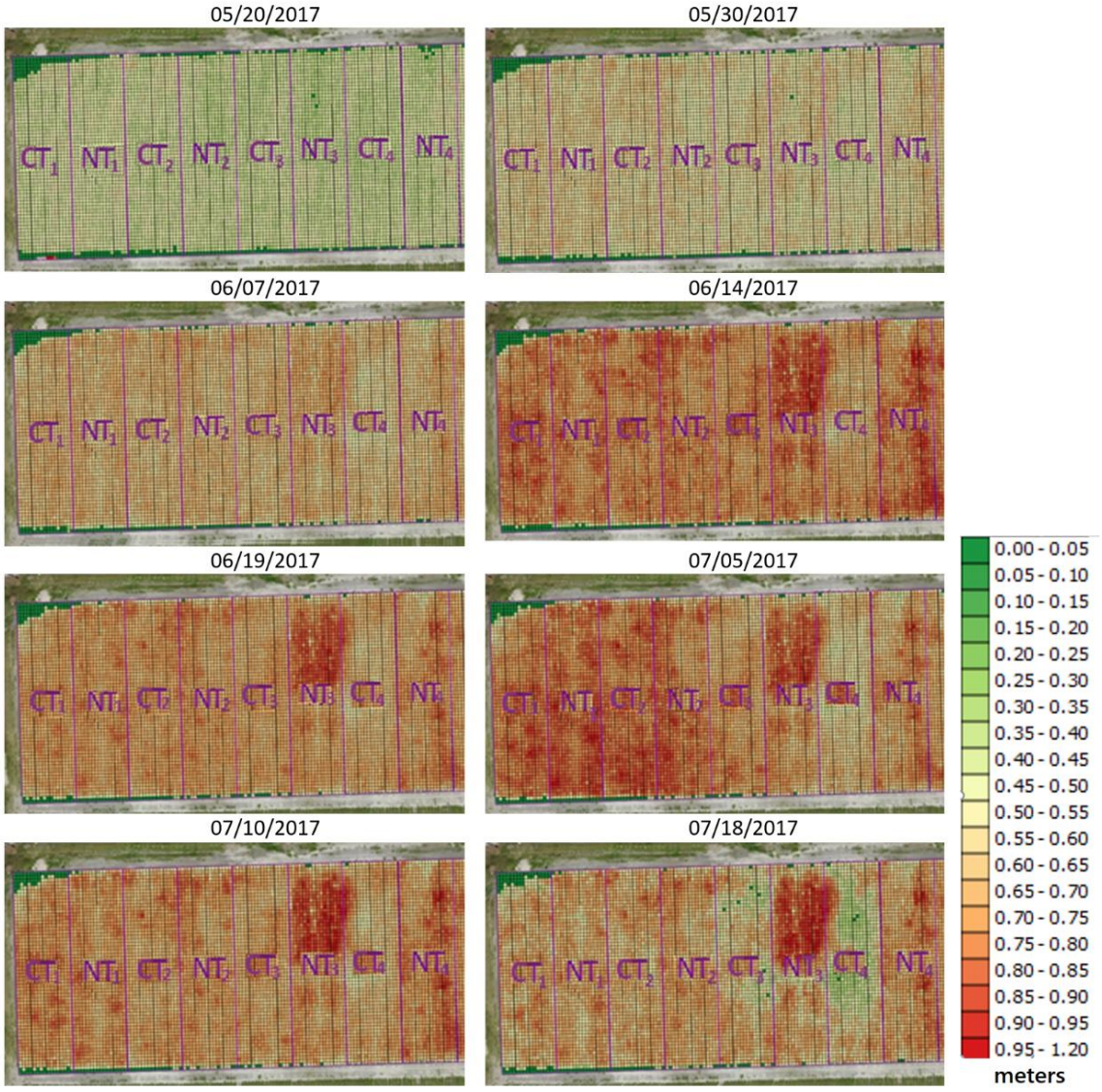

Figure 2.3. Canopy height grid maps for each flight in the growing season with legends.

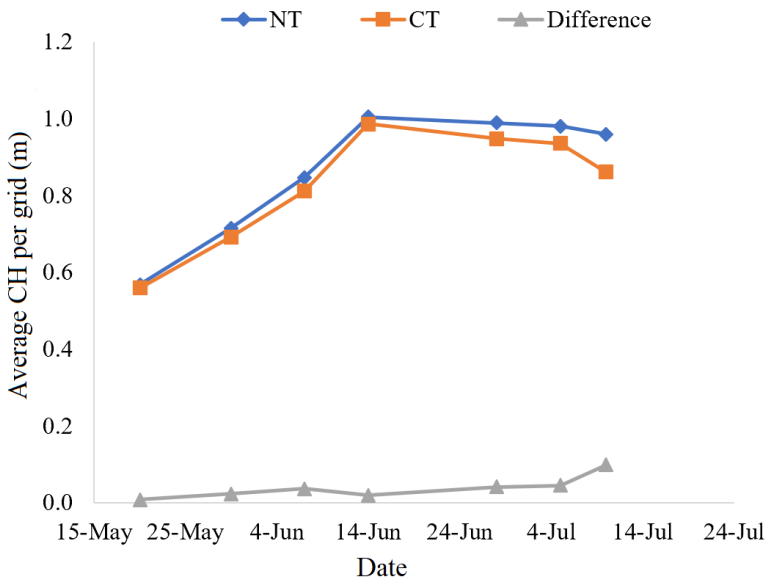

Figure 2.4. Average canopy height measured for conventional-tillage (CT) and no-tillage (NT) cropping systems and their difference at each flight.

Table 2.3. Average canopy height for conventional-tillage (CT) and no-tillage (NT) cropping systems with their standard deviation (SD) and Z statistics results at each flight.

Date	NT		CT		z value
	CH (m)	SD	CH (m)	SD	
20-May	0.57	0.06	0.56	0.05	1.41
30-May	0.71	0.05	0.69	0.06	**4.12**
7-Jun	0.85	0.06	0.81	0.06	**5.91**
14-Jun	1.00	0.08	0.99	0.09	**2.69**
28-Jun	0.99	0.08	0.95	0.11	**5.49**
5-Jul	0.98	0.08	0.94	0.08	**7.29**
10-Jul	0.96	0.10	0.86	0.16	**11.67**

Figure 2.5 presents the CC grid maps for each flight in the growing season. Much like CH, CC also consistently increased from 47% on May 20, 2017, to 95% on July 5, 2017, for NT plants (Figure 2.6). During the same time, CC for CT plants increased from 44% to 84%. However, CC reached its peak value on July 10, 26 days later than that of CH. Due to the fact that, even though the height of the plant reached its peak, the plant was still densifying; hence the biomass or the total areal coverage was still increasing. A decreasing trend was observed in CC under NT and CT

plants after July 10. Between July 18 and July 23, a decrease of 28% in CC for NT and 43% in CC for CT plants was observed due to the defoliation process, a common practice in cotton fields to prepare the crop for harvesting. It can also be observed that plants growing under the NT treatment had higher CC than the plants growing under the CT treatment, and the difference consistently increased from 3% to 25% between May 20 and July 23, 2017 (Figure 2.6). The statistical test confirmed that the NT plants had significantly higher CC than CT plants, with no exception (Table 2.4).

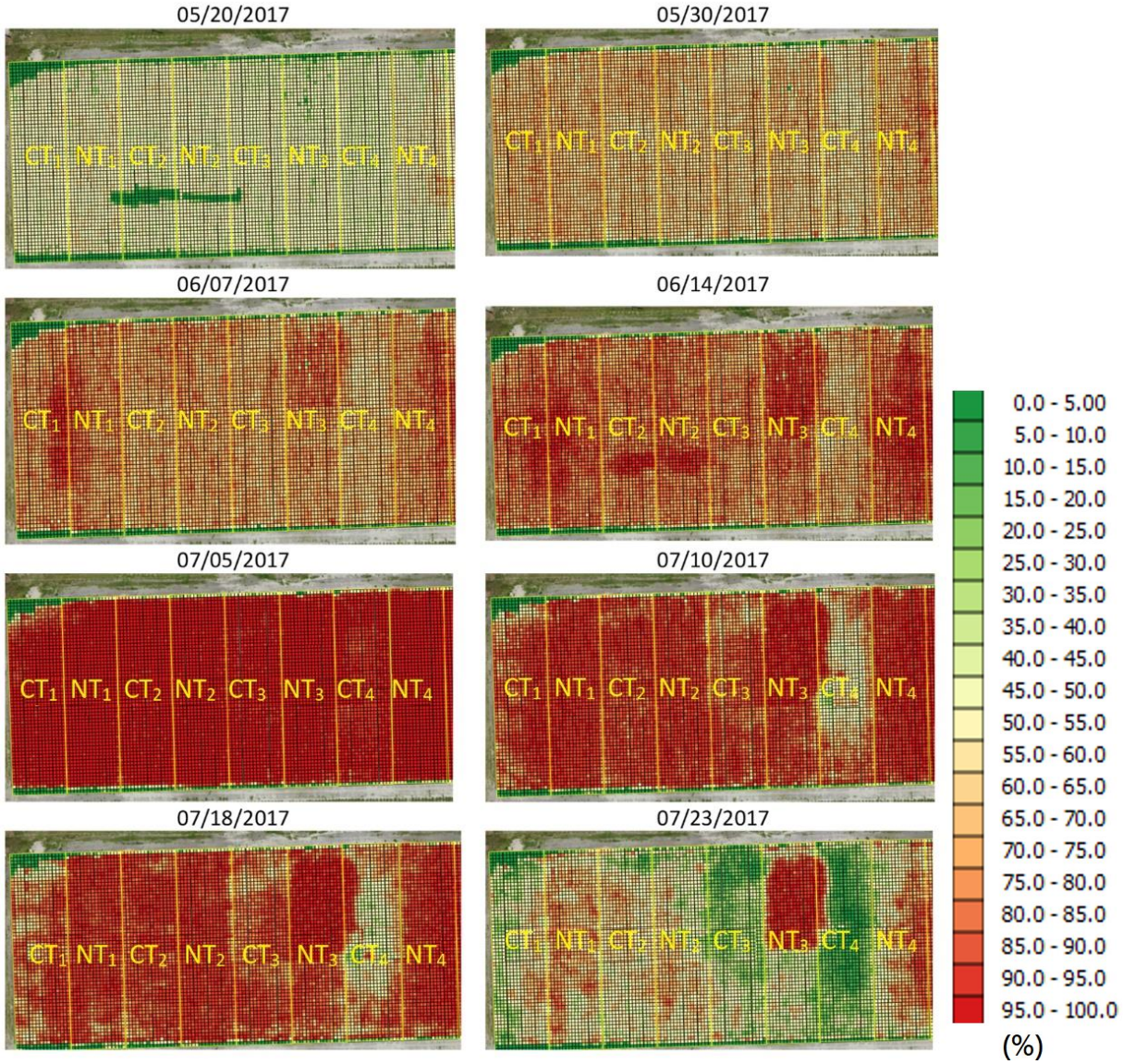

Figure 2.5. Canopy cover grid maps for each flight in the growing season with legends.

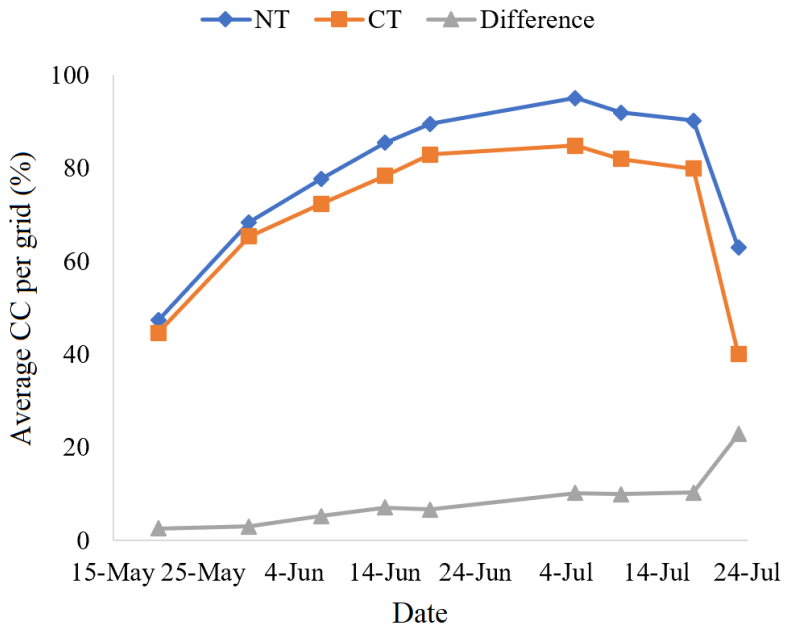

Figure 2.6. Average canopy cover (CC) measured for conventional-tillage (CT) and no-tillage (NT) cropping systems and their difference at each flight.

Table 2.4. Average canopy cover (CC) for conventional-tillage (CT) and no-tillage (NT) cropping systems with their standard deviation (SD) and Z statistics results at each flight.

Date	NT		CT		z value
	Average CC (%)	SD	Average CC (%)	SD	
20-May	47.28	8.02	44.64	7.95	**3.79**
30-May	68.34	6.55	65.28	6.56	**4.52**
7-Jun	77.71	6.85	72.38	7.86	**8.83**
14-Jun	85.41	6.93	78.28	8.31	**10.02**
5-Jul	89.50	5.54	82.86	8.44	**11.02**
10-Jul	95.05	0.68	84.80	2.49	**15.56**
18-Jul	91.91	4.82	81.93	14.02	**13.83**
23-Jul	63.20	6.09	38.14	15.13	**13.96**

Figure 2.7 presents the CV grid maps for each flight in the growing season. CH and CC reached their plateau on June 14 and July 10, respectively. Since CV is a function of both CH and CC, it reached a plateau on June 28, which falls in the middle of peak dates for CH and CC. Later in the season, between July 5 and July 18, a decrease of 0.15 m^3 for NT plants and 0.27 m^3 was

observed, attributed to the defoliation process (Figure 2.8). Comparable to CH and CC, NT plants had a significantly greater CV than CT plants, and the difference consistently increased from 0.01 m^3 to 0.11 m^3 between May 20 and July 18, 2017 (Table 2.5).

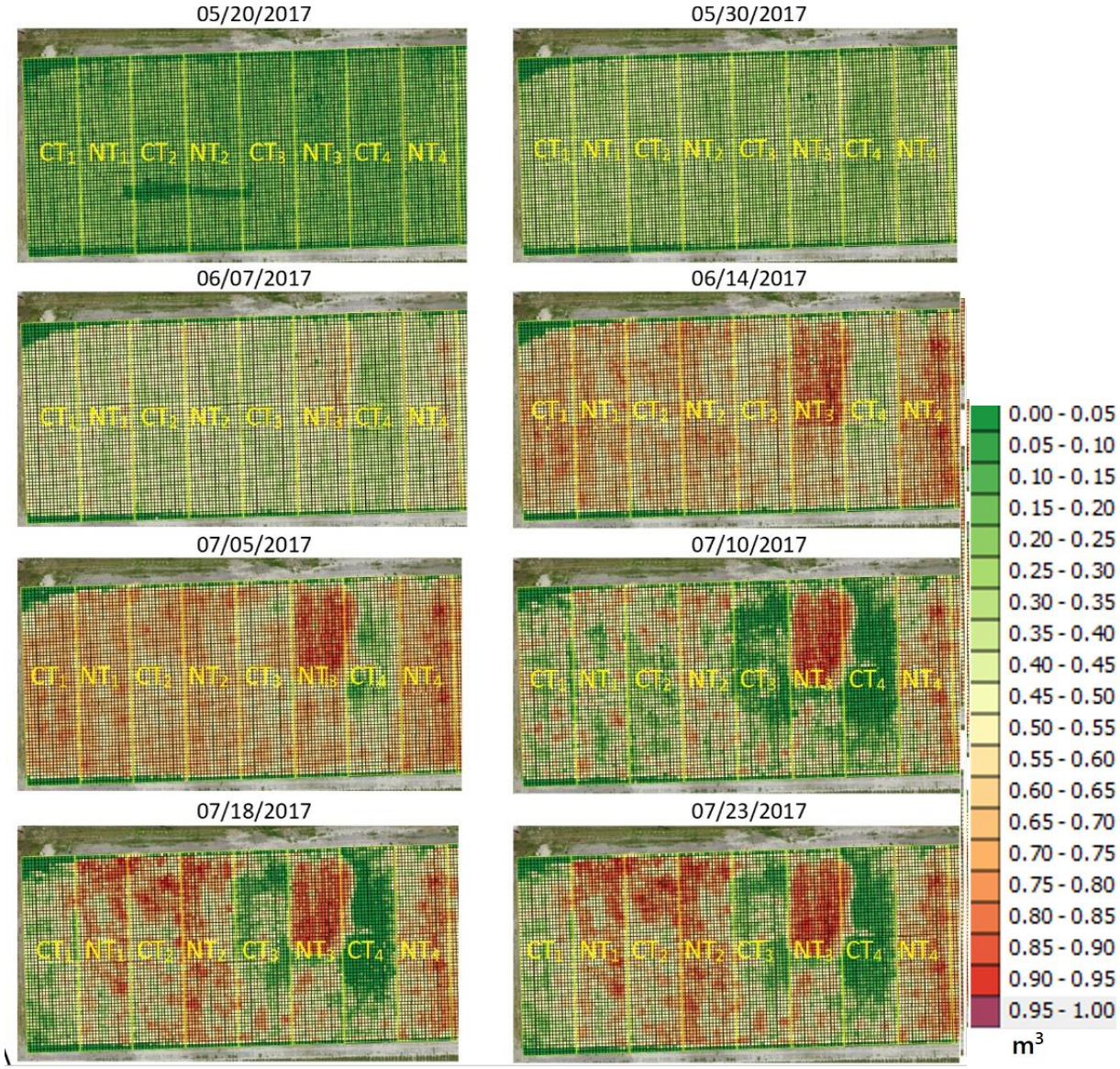

Figure 2.7. Canopy volume (CV) (m^3) grid maps for each flight in the growing season with legends.

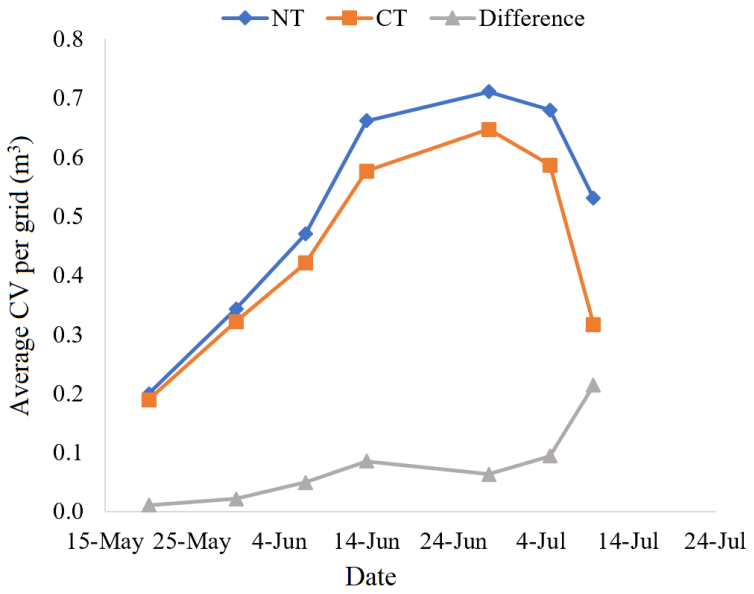

Figure 2.8. Average canopy volume (CV) measured for conventional-tillage (CT) and no-tillage (NT) cropping systems and their difference at each flight.

Table 2.5. Average canopy volume (CV) for conventional-tillage (CT) and no-tillage (NT) cropping systems with their standard deviation (SD) and Z statistics results at each flight.

Date	NT		CT		z value
	Average CV (m^3)	SD	Average CV (m^3)	SD	
20-May	0.20	0.05	0.19	0.04	**2.06**
30-May	0.34	0.06	0.32	0.05	**3.79**
7-Jun	0.47	0.08	0.42	0.07	**7.81**
14-Jun	0.66	0.09	0.58	0.11	**11.54**
28-Jun	0.71	0.09	0.65	0.14	**8.30**
5-Jul	0.68	0.09	0.59	0.13	**12.10**
18-Jul	0.53	0.19	0.32	0.20	**20.41**

NDVI is the canopy trait extracted from spectral information which indicates plant health (Novikova et al., 2020), unlike other quantitative parameters such as CC, CH, and CV. Figure 2.9 presents the NDVI grid maps for each flight in the growing season. Between May 20 and July 5, the average NDVI increased consistently (from 0.85 to 0.92 for NT plants and 0.82 to 0.90 for CT plants). After reaching their peak on July 5, NDVI values decreased over time for CT and NT systems (Figure 2.10). Moreover, it was also observed that plants under NT had greater average

NDVI than plants under the CT system. Table 2.6 suggested that the difference between NT and CT systems was statistically significant.

For July 10 and later, as plants matured, average NDVI values were 0.85 or lower, except for a patch on the upper side of NT_3, where NDVI values were still 0.9 or higher. A similar trait was observed in CH, CC, and CV grid maps (Figure 2.3, Figure 2.5, and Figure 2.7), where parameter values over the patch were significantly higher compared to the surrounding area. A slight depression in the surface area of the patch caused water accumulation, consequently greater water availability to plants which resulted in the different growth patterns of the plants in the patch area compared to the growth pattern of the plants in the surrounding area. To maintain the consistency of the experiment, the patch area was removed from the analysis for a fair comparison.

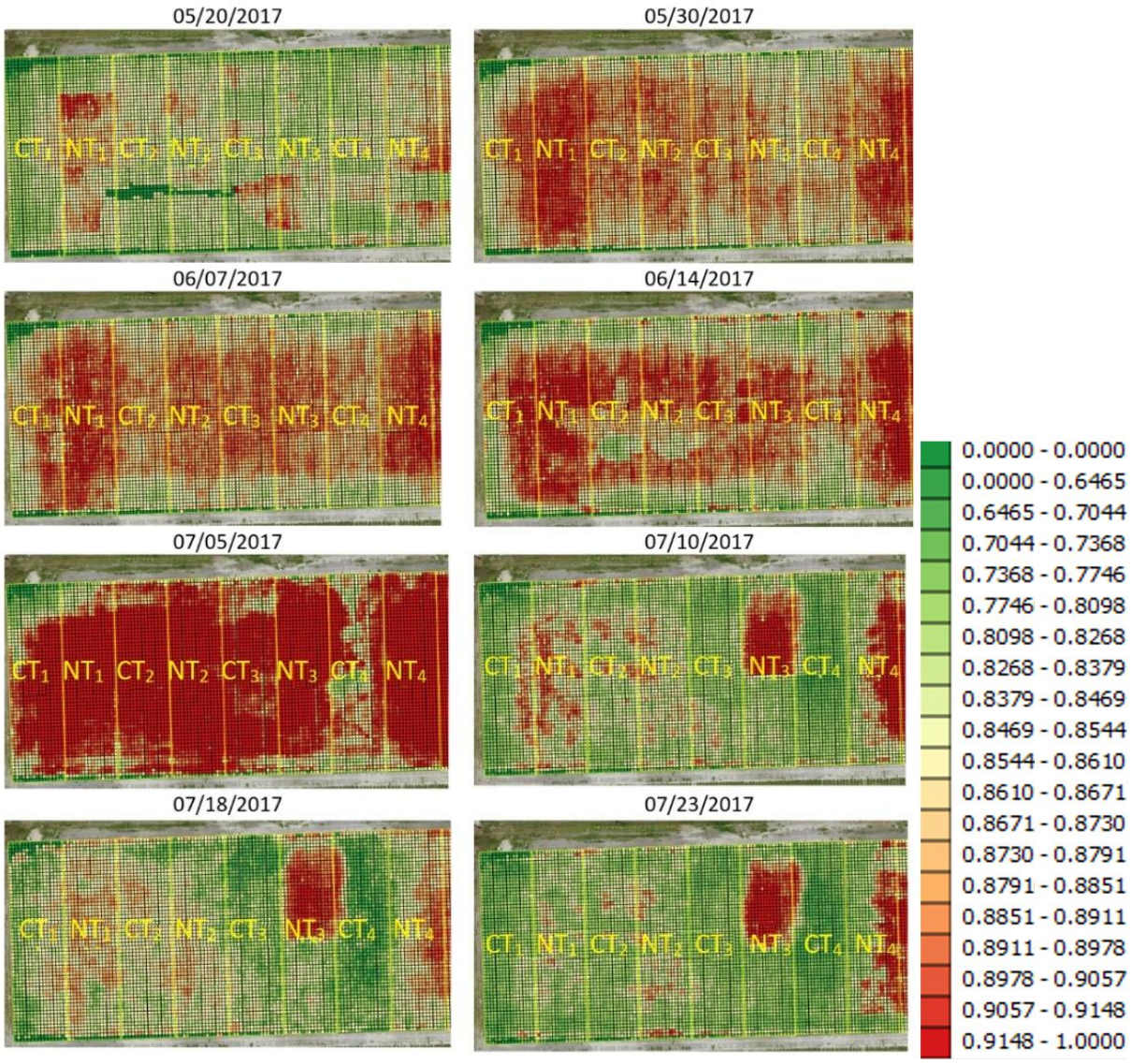

Figure 2.9. NDVI grid maps for each flight in the growing season with legends.

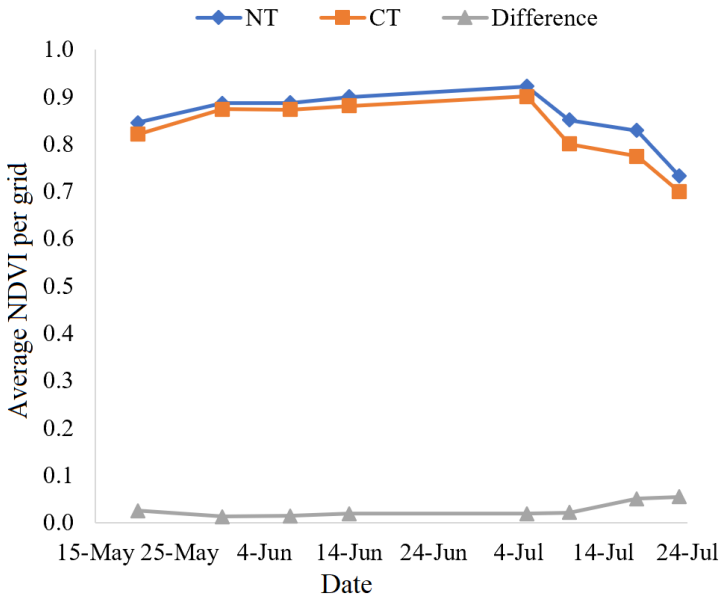

Figure 2.10. Average normalized difference vegetation index (NDVI) measured for conventional-tillage (CT) and no-tillage (NT) cropping systems and their difference at each flight.

Table 2.6. Average normalized difference vegetation index (NDVI) for conventional-tillage (CT) and no-tillage (NT) cropping systems with their standard deviation (SD) and Z statistics results at each flight.

Date	NT		CT		z value
	Average NDVI	SD	Average NDVI	SD	
20-May	0.85	0.07	0.82	0.10	**3.43**
30-May	0.89	0.02	0.87	0.02	**3.97**
7-Jun	0.89	0.02	0.87	0.02	**4.06**
14-Jun	0.90	0.02	0.88	0.03	**5.34**
5-Jul	0.92	0.03	0.90	0.04	**5.51**
10-Jul	0.85	0.04	0.80	0.05	**10.20**
18-Jul	0.83	0.05	0.77	0.05	**9.82**
23-Jul	0.73	0.04	0.70	0.03	**8.12**

Figure 2.11 presents replication-wise and overall yield (lb/ha) for CT and NT cropping systems. The yield was obtained using a modified 2-row cotton picker that allowed yield to be captured for each plot and row individually. Cotton picker only removes the seed cotton from the open boll, leaving plants in the field. After separating lint and seeds, samples were bagged, and

lint weights were obtained after harvest. The average yield was significantly higher in the NT system (3397 lb/ha) than the CT system (2885 lb/ha). While comparing neighboring replications, it was reported that NT yields were higher than CT, with the difference ranging from ~220 lb/ha to ~992 lb/ha, except for NT_2 and CT_2, where CT yield was 40 lb/ha higher compared to NT.

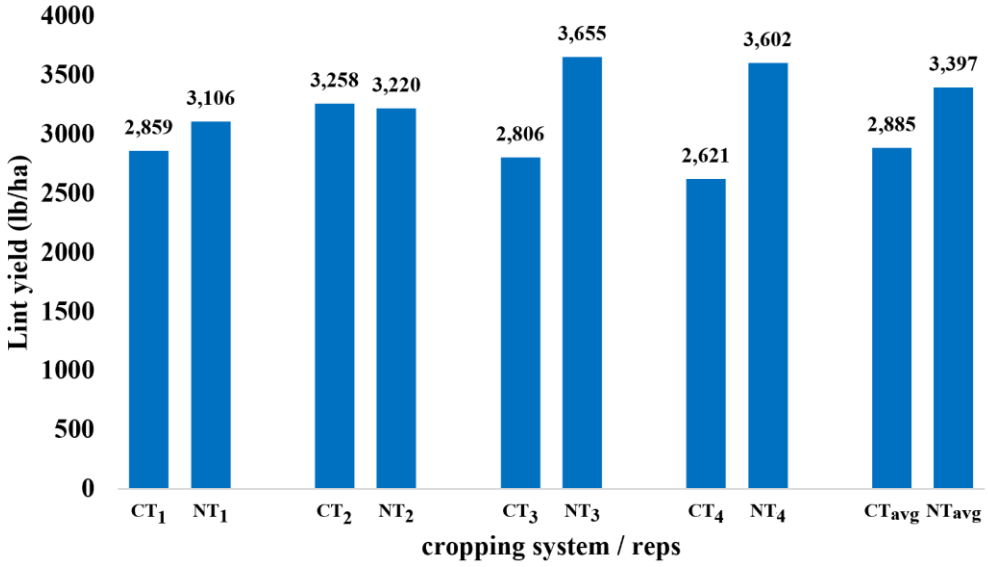

Figure 2.11. Replication-wise and overall yield (lb/ha) for conventional-tillage (CT) and no-tillage (NT) cropping systems.

Plants under the NT system had higher plant parameter values and higher yields than plants under the CT system in general. However, this should not be misconstrued as yield always has a positive correlation with plant parameters. It is important to have optimum plant size to maximize resources utilization. Previous studies (Freeland Jr et al., 2006) suggested that a large size canopy will use water and other inputs to maintain the vegetative structures and reduce the efficiency of leaves to translate the captured energy to yield, particularly in the case of indeterminate crops like cotton. If the plants continue to produce vegetative structures, the production of reproductive structures is neglected, resulting in a reduction of yield. Therefore, under a dryland environment, it is important to have optimum canopy size. Concurrently, a smaller canopy size will reduce the yield as the plant will not be able to capture enough solar radiation, which is the key component in photosynthesis and yield. Therefore, site-specific and region-specific studies need to be

performed to investigate the successful implementation of the NT cropping system, which is beyond the scope of this dissertation. The main focus of this study was to investigate how UAS technology can help to quantify the agronomic differences throughout the growing season in different cropping systems more efficiently and reliably than traditional methods. However, there are region-specific studies supporting the higher performance of the NT system over the CT system (Zhao et al., 2017). Previous crop residue substantially increases water infiltration and retention in the soil, and better soil moisture availability contributes to higher plant growth and performance. The residue left intact from previous years also contributes to the increase of organic matter in NT systems supporting microbial activity and biodiversity, allowing many organisms to flourish and make a commensal association with the crop (Guo et al., 2016). Moreover, since the soil is not being disturbed by disking, plowing, and cultivation, NT systems maintain soil structure and contribute to increased soil aggregate stability (Sapkota, 2012).

2.4.2 Neighboring replication comparison

Although yield analysis presented in Figure 2.11 suggested that the overall average yield for the NT system was significantly greater than the CT system, the neighboring plot-wise yield results did not confirm the same. It was reported that NT yields were higher than CT, with the difference ranging from ~220 lb/ha to ~992 lb/ha, except for NT_2 and CT_2, where CT yield was 40 lb/ha higher compared to NT. Furthermore, differences in the yield among the other replications were variable. This called for a neighboring replication-wise comparison of all the canopy parameters to see if the difference comes out to be commensurate with the yield analysis. Figure 2.12, Figure 2.13, Figure 2.14, and Figure 2.15 present the neighboring replications comparison of CT and NT cropping systems over CH, CC, CV, and NDVI, respectively.

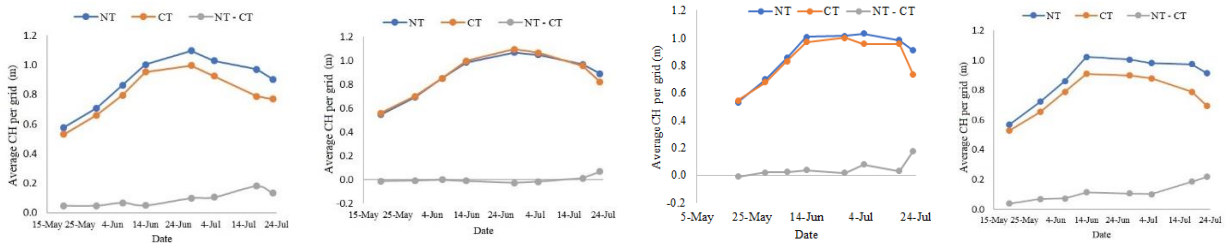

(a) (b) (c) (d)

Figure 2.12. Average canopy height (CH) measured for conventional-tillage (CT) and no-tillage (NT) cropping systems and their difference at each flight for (a) NT_1& CT_1, (b) NT_2 & CT_2, (c) NT_3 & CT_3, and (d) NT_4 & CT_4.

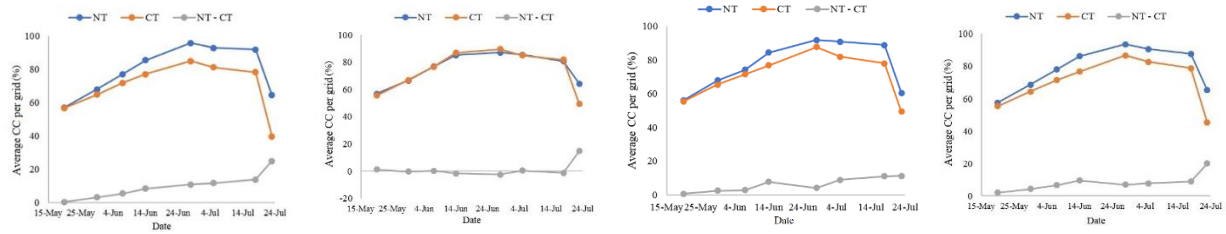

(a) (b) (c) (d)

Figure 2.13. Average canopy cover (CC) measured for conventional-tillage (CT) and no-tillage (NT) cropping systems and their difference at each flight for (a) NT_1& CT_1, (b) NT_2 & CT_2, (c) NT_3 & CT_3 and (d) NT_4 & CT_4

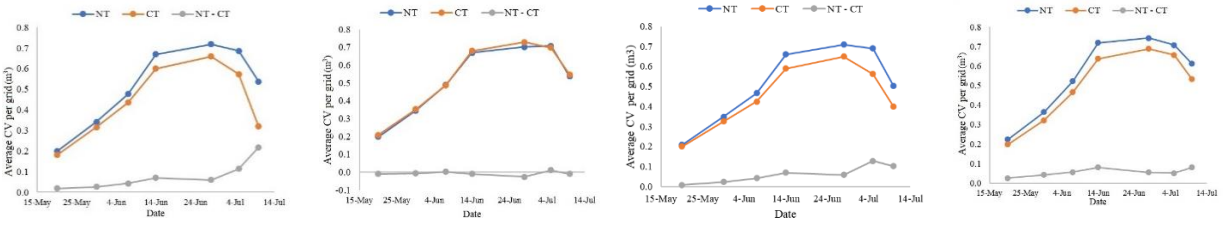

(a) (b) (c) (d)

Figure 2.14. Average canopy volume (CV) measured for conventional-tillage (CT) and no-tillage (NT) cropping systems and their difference at each flight for (a) NT_1& CT_1, (b) NT_2 & CT_2, (c) NT_3 & CT_3 and (d) NT_4 & CT_4

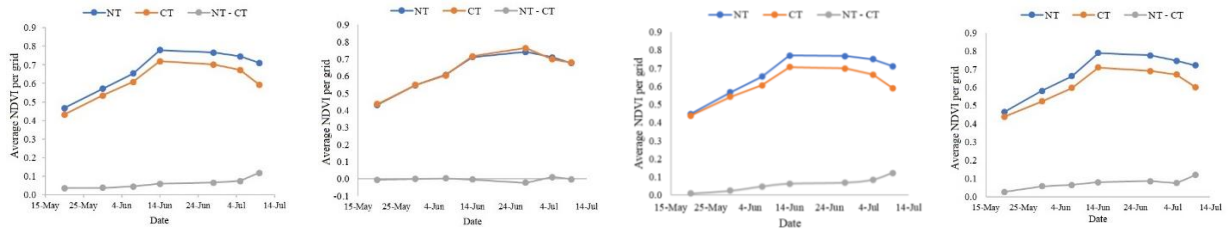

(a) (b) (c) (d)

Figure 2.15. Average normalized difference vegetation index (NDVI) measured for conventional-tillage (CT) and no-tillage (NT) cropping systems and their difference at each flight for (a) NT_1& CT_1, (b) NT_2 & CT_2, (c) NT_3 & CT_3, and (d) NT_4 & CT_4

Neighboring replication-wise comparison of canopy parameters suggested that canopy parameter values for the NT system are significantly higher than CT parameter values, except for plot CT_2 and NT_2. This distinct behavior possessed by parameter values for plot CT_2 and NT_2 is highly commensurate with the yield difference between CT_2 and NT_2 (Figure 2.11). It is evident that UAS based measurements facilitate tracking the behavior anomaly possessed by a different part of the field, which can eventually help agriculture scientists conduct a posterior analysis. It is most likely that yields obtained from the second replication were not impacted by tillage management due to field variation. NT_2 and CT_2 have similar canopy parameter values, whereas the other three replications differ. Greater canopy parameter values were measured in NT_1, NT_3, and NT_4 compared to CT_1, CT_3, and CT_4, respectively. The lack of difference between NT_2 and CT_2 was potentially due to a low-lying area of the field within NT_2 and CT_2 compared to the remaining replications, which is likely to hold soil moisture for a longer time period into the flash drought period of June and July 2017 (Zhang et al., 2021). However, soil moisture was not measured, and there may be other factors, such as residue in the NT plots, micro-environment of soil nutrients, among others which impacted seed emergence, stand count, and ultimately yield (Derpsch et al., 2014; Kennedy and Hutchinson, 2001).

2.4.3 Manual height measurements

Initially, manually measured average CH for both the cropping systems were compared with UAS derived average CH. Since manual CH measurements consisted of 10 measurements taken from only two middle rows per replication, UAS derived average CH measurements derived from grids in two middle rows of each replication were considered for the fair comparison. Comparable to UAS derived overall average CH (Figure 2.4), UAS derived average CH computed only from two middle rows of each replication also indicated that plants growing under the NT treatment were generally taller than plants growing under the CT treatment, and the difference steadily increased over time from one centimeter on May 20 to seven centimeters on July 23 (Figure 2.16). Although manually measured average CH indicated an overall increasing trend similar to UAS derived average CH, it indicated no statistical difference between treatments for half of the flights, as opposed to UAS derived measurements which indicated that the difference in the average CH under both treatments was significant for all the flights (Table 2.7). Manual measurements consisted of only ten randomly measured CH values over the middle two rows of each replication. Small sample size and large standard deviation of the manual measurements led to an inconclusive statistic regarding the overall trend of the average CH measurements compared to UAS based average CH measurements.

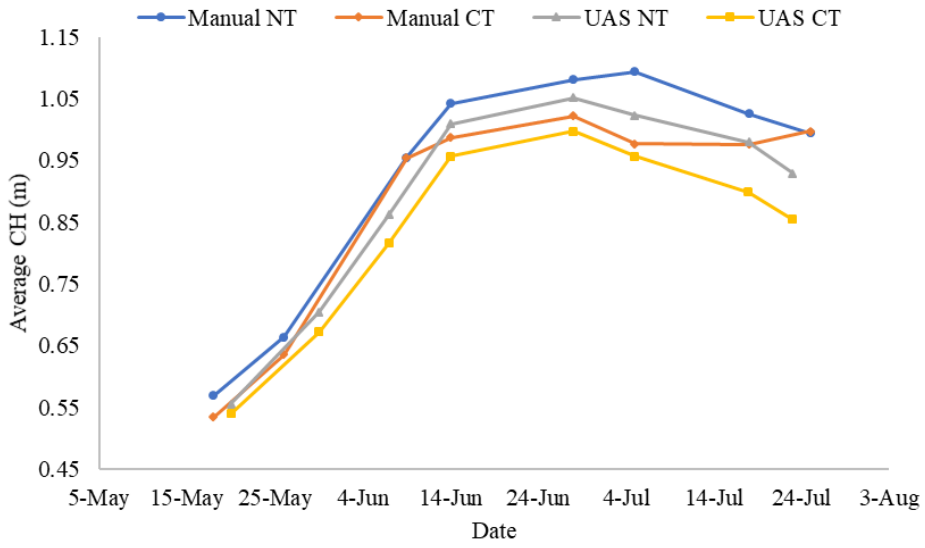

Figure 2.16. Manually measured average canopy height (CH) over a sample of 10 measurements in two middle rows per replication for conventional-tillage (CT) and no-tillage (NT) cropping system and UAS derived average CH considering only two middle rows per replication for CT and NT cropping system.

Table 2.7. UAS derived and manually measured average CH for CT and NT cropping systems with their standard deviation (SD), and Z statistics results at each flight.

	UAS-NT		UAS-CT				Manual-NT		Manual-CT		
Date	**Average CH (m)**	**SD**	**Average CH (m)**	**SD**	**z value**	**Date**	**Average CH (m)**	**SD**	**Average CH (m)**	**SD**	**z value**
20-May	0.55	0.03	0.54	0.04	1.71	18-May	0.56	0.04	0.53	0.04	**2.01**
30-May	0.70	0.04	0.67	0.08	**2.80**	26-May	0.66	0.04	0.63	0.06	1.41
7-Jun	0.86	0.06	0.81	0.08	**3.87**	9-Jun	0.95	0.052	0.95	0.07	0.03
14-Jun	1.00	0.03	0.95	0.06	**5.28**	14-Jun	1.04	0.15	0.98	0.10	1.84
28-Jun	1.05	0.02	0.99	0.06	**5.53**	28-Jun	1.08	0.08	1.02	0.09	**2.34**
5-Jul	1.02	0.04	0.95	0.08	**5.95**	5-Jul	1.09	0.06	0.97	0.06	**5.51**
18-Jul	0.97	0.05	0.89	0.08	**6.74**	18-Jul	1.02	0.08	0.97	0.05	**2.35**
23-Jul	0.92	0.08	0.85	0.14	**4.88**	25-Jul	0.99	0.03	0.99	0.03	-0.18

A neighboring replication-wise comparison was also performed between CT and NT cropping systems to investigate manually measured CH further. It was observed that neighboring replication-wise UAS-based height measurements create a smooth growth curve and follow a trend (Figure 2.12). In contrast, neighboring replication-wise manual measurements do not seem to be consistent, especially for CT (Figure 2.17). Sample size may play a significant role in shaping the trend of the data. While manual data collection consisted of measuring ten plants in the two middle rows of each replication, UAS measured the entire plant population of that replication.

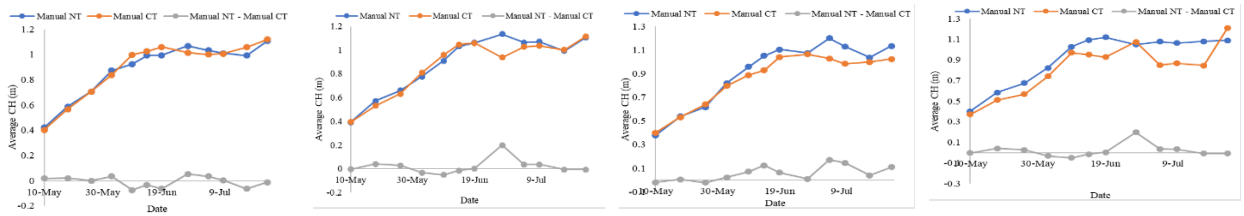

(**a**) (**b**) (**c**) (**d**)

Figure 2.17. Manually measured average canopy height (CH) over a sample of 10 measurements in two rows per replication for conventional-tillage (CT) and no-tillage (NT) cropping system and their difference at each flight for (a) NT_1 & CT_1, (b) NT_2 & CT_2, (c) NT_3 & CT_3, and (d) NT_4 & CT_4.

For UAS measurements, CH values under the NT system were significantly higher than that of CT, except for CT_2 and NT_2 (Figure 2.12). However, manual measurements suggest no significant difference between cropping systems, except for a few dates. Due to limited sample size and high standard deviation, manual CH measurements can be misleading and were not able to represent the actual trend of the overall plant population. Increasing sample size for manual measurements would result in a better representation of plant population; however, it can be time-consuming and labor-intensive. Moreover, manual CH measurements are always susceptible to human errors. On the other hand, UAS-based measurements are seamless, repeatable, and reliable.

UAS served as high precision and cost-effective technology to quantify the difference between cropping systems throughout the growing season. Manual measurements proved to be more challenging, especially in terms of sample size. Moreover, manually measuring canopy parameters like CC and CV is not practically feasible. These limitations in manual data collection make UAS-based data more robust and reliable. However, formulating a clear, outlined methodology during the UAS flight planning phase is critical to acquiring high-quality data. The quality of UAS data is the function of flying altitude, image forward and side overlaps, ground sample distance, and the completeness of the DTM reconstructed using the SfM pipeline. Additionally, weather conditions also significantly affect the quality of UAS data, especially the wind speed. Since our experimental setup was in the coastal region, the high wind had been the critical issue. Although all our flights were always conducted under 15mph wind speed, the movement of plant leaves during data collection impacts the quality of the point cloud and, in turn, the quality of UAS derived CHM. Moreover, since the canopy volume is also a function of canopy height, any error in the height measurements also affects the canopy volume measurement.

Parameters based on spectral information such as NDVI entirely depend on the type and quality of the multispectral sensor used. The SlantRange 3p sensor used in this study can be radiometrically calibrated with the incident light, allowing temporal NDVI maps to be compared despite changes in lighting conditions across different flights throughout the season. NDVI measurements can be obtained using other platforms, namely, ground-based sensors, UAS based and satellite-based multispectral sensors. Compared to ground-based NDVI measurements, UAS based data collection is faster, and it is not labor-intensive. Moreover, it is free from the restrictions associated with access to the field due to the application of pesticides or irrigation (Tattaris et al., 2016). Satellite-based NDVI measurement is more commonly reported in the literature using various satellite platforms such as Landsat-8, SPOT-5, MODIS, Sentinel-2, and WorldView-2, to name a few (Valderrama-Landeros et al., 2018). Recently, UAS has gained more popularity for NDVI computation (Stanton et al., 2017). Although satellite images have the advantage to cover a vast area, UAS based sensors are preferable for NDVI computation because of their ability to discard non-canopy pixels from the image, which is not possible with satellite-based coarser spatial

resolution images. Temporal monitoring of crops requires short revisit times, which is costly and ineffective with satellite sensors (Ghazal et al., 2015). Moreover, UAS based sensors are less affected by environmental effects such as water vapor, occlusion by cloud, temperature change. However, UAS technology also has limitations, such as limited operation time (battery capacity) and short-range, questioning its applicability over large areas (Yue et al., 2019).

The objective of this study was to quantify agronomic differences in cotton plants under CT and NT cropping systems in the Coastal Bend of Texas. Overall averages and neighboring replications comparison of UAS-based measurements revealed that the NT cropping system resulted in the taller canopy, higher percentage CC, biomass (CV), NDVI, and also, higher yield than CT. NT systems not only have the potential to sustain or improve yield but nonetheless can also benefit farmers through a reduction in labor. According to the study (Staropoli, 2016), NT systems can save up to 225 hours of labor per year for a 500-acre farm. NT systems improve water infiltration and storage, help rebuild organic matter, decrease erosion risk, and support microbial activity. Overall, NT systems are often more sustainable than CT practices. Moreover, the NT system is more efficient in saving fuel costs by reducing tractor passes compared to the CT system, reducing the farming's global warming footprint. Despite all the advantages, a global meta-analysis performed to investigate the circumstances when NT system yields more revealed that NT system performance is highly context-dependent (Pittelkow et al., 2015b). High yield in dry climates under the NT system is attributed to better water infiltration and more significant soil moisture conservation. On the contrary, the yield deteriorates when using the same NT system in humid climates, which is caused by fungal diseases developed due to elevated moisture levels in the soil. However, as per a meta-study, the decline in the yield in humid climates can be unrelated to the cropping system (Pittelkow et al., 2015a). Hence, site-specific and region-specific studies need to be performed to investigate the successful implementation of the NT cropping system. In addition, UAS technology can help to quantify the agronomic differences throughout the growing season in different cropping systems more efficiently and reliably than traditional methods.

2.5 Conclusion

This study presented a novel approach to assess the reliability of multi-temporal UAS data to compare CT and NT cotton cropping systems. CH, CC, CV, and NDVI were the four canopy parameters used to quantify differences between cropping systems. Overall averages and neighboring replications comparisons between cropping systems were performed, and results revealed that NT values were significantly higher than CT when UAS-based measurements were considered. NT had a taller canopy, higher CC, higher biomass, higher NDVI, and higher yield compared to CT. UAS-based parameter estimation is more efficient than manual data in terms of time, cost, and labor. Moreover, unlike manual measurements that rely on limited samples, UAS technology provides the capability to exploit the entire population. This makes UAS derived data more robust and reliable. UAS also permits modifying sample size according to the objective of the experiment with less effort. In other words, UAS technology has revolutionized the way we can perform varying degrees of analysis with canopy parameters over a temporal scale. In the future, this study could be extended to other crops and different management practices. Different data collection frequency, varying grid size, and varying sample size could also be an option to analyze different outputs.

3. A COMPARATIVE STUDY OF RGB AND MULTISPECTRAL SENSOR BASED COTTON CANOPY COVER MODELLING

3.1 Background

Canopy cover (CC) is commonly expressed as the percentage of total ground areal coverage by the vertical projection of plant canopy. Plant canopy cover is strongly related to crop growth, water use, and photosynthesis, making it an important trait to be observed throughout the growing season (Trout et al., 2008). In addition, CC is an essential ancillary variable in estimating the Leaf Area Index (LAI) (Nielsen et al., 2012). Recently, UAS has emerged as an alternate to the satellite, airborne imaging sensors or LiDAR sensors to estimate CC, which is more affordable and could provide higher temporal and spatial resolution (Ashapure et al., 2019c; Chianucci et al., 2016; Chu et al., 2016; Fernandez-Gallego et al., 2018; Holman et al., 2016). CC computation using multispectral (MS) sensors gained more popularity over RGB sensors. MS sensors are stable over time due to their irradiance sensor (Clevers et al., 2017; Pauly, 2014; Roth and Streit, 2018; Xu et al., 2019). However, numerous studies have suggested that MS sensors are relatively more expensive compared to RGB sensors (Fuentes-Peailillo et al., 2018; Gracia-Romero et al., 2017; Heidarian Dehkordi et al., 2020; Herzig et al., 2021; Marcial-Pablo et al., 2019). Manfreda et al. (2018) provided a cost comparison of state-of-the-art RGB and MS sensors widely used in remote sensing applications. The authors reported that the cost of commonly used RGB sensors ranges from $500 to $3,400, with an average cost of $1630. On the other hand, MS sensors have a price range of $300 to $34,000, with an average value of $11,000 at the time of publication. Additionally, MS sensors impose a higher payload weight on the UAV compared to consumer-grade RGB sensors (Grybas and Congalton, 2021; Herzig et al., 2021; Zheng et al., 2018). To have higher accuracy of CC estimation, several studies in the past have relied on MS sensors. Even though

Content of this chapter is published as follows: Ashapure, A., Jung, J., Chang, A., Oh, S., Maeda, M., & Landivar, J. (2019). A comparative study of RGB and multispectral sensor-based cotton canopy cover modelling using multi-temporal UAS data. *Remote Sensing*, *11*(23), 2757.

there exists a large body of literature focusing on the use of MS sensor for CC estimation, adequate attention has not been paid to explore the limited spectral information provided by RGB sensors to estimate CC. This study aims to fill this knowledge gap present in this important area of research by investigating an RGB sensor based CC estimation method.

RGB-based CC estimation methods can be divided into two categories: thresholding and pixel classification. Thresholding methods require specifying the color thresholds or the ratios to identify the canopy pixels. Pixel classification methods use a supervised or unsupervised pixel-wise classification method to identify canopy pixels. In this study, K-means clustering is used to perform pixel-based segmentation. However, other conventional segmentation could also be adopted, such as Graph-cut, Fuzzy C-mean, level set segmentation, etc., without the loss of generalization (Brox and Weickert, 2006; Chuai-Aree et al., 2001; Yi and Moon, 2012). Although pixel classification methods are highly accurate, they are time-consuming and computationally extensive. Therefore, it is vital to compare various CC estimation methods to find the most affordable, accurate, and computationally efficient CC estimation.

3.1.1 Scope and contribution

Despite there being significant literature exploring RGB-based CC estimation (Fang et al., 2016; Lima-Cueto et al., 2019; Marcial-Pablo et al., 2019; Torres-Sánchez et al., 2014), there is a scarcity of research that compares different CC estimations throughout the crop growing season. A consistent observation in these case studies was that RGB-based CC estimation is inaccurate in the late season. Additionally, improving RGB sensor-based CC estimation performance in the late season is not discussed in the literature. The ability to accurately estimate CC in the late season is important for an indeterminate perennial crop such as cotton, which is grown and managed as an annual crop. Its indeterminate growth pattern allows the crop to simultaneously produce vegetative and reproductive structures. As the fruit load develops, the demand for carbohydrates and nutrients increases in proportion to the number of developing fruits. However, the supply of carbohydrates reaches a limit which is set by canopy light interception. When the demand for carbohydrates exceeds the supply, the crop temporarily pauses its vegetative growth and begins a phenomenon

commonly named “cutout” (Landivar et al., 2010), which represents physiological maturity. In the case of abundant availability of nutrients and water available in the soil, the plant continues to grow its vegetative parts. In this condition, a growth regulator is applied to restrict the vegetative growth so that the plant directs its energy to reproductive parts. Considering the cutout and the application of growth regulators, CC estimation in the late season is essential for managing the cotton crop. This study compared RGB-based CC estimation methods with MS sensor-based CC estimation and proposed an improved RGB-based CC estimation approach to address this knowledge gap. The proposed CC estimation approach will provide a more affordable option to breeders and agriculture scientists.

3.2 Study area, sensors, and platforms

A field experiment was established at the Texas A&M AgriLife Research and Extension Center in Corpus Christi, TX (Latitude 27°46’59” N and longitude 97°34’13” W) in 2017 and 2018, respectively. The trial consisted of five cotton genotypes in 2017 and ten genotypes in 2018 from the Texas A&M AgriLife Cotton Breeding Program (presented in Figure 3.1). Genotype details are still confidential and not released by the breeders till the writing of this dissertation. Soil types in the study site were Victoria Clay series soils (Victoria-Lattas-Clareville). For the 2017 experiment, seeds were planted on March 22, 2017, and machine harvested on August 5, 2017. For the 2018 experiment, seeds were planted on March 14, 2018, and machine harvested on August 1, 2018, in a skip or solid row pattern (i.e., one- and two-row plots, respectively), and each genotype was replicated four times. The fields were divided into 1m x 1m size grids. The number of grids in the 2017 and 2018 experiments was 300 and 600, respectively. The total area of the experimental field was approximately 1.6 acres in 2017 and approximately 5.1 acres in 2018. Provided the experimental field was in a coastal area, wind speed and rain were the potential factors to be considered before every flight. Flights were conducted between 10:00 AM to 2:00 PM. The temperature variation throughout the growing season varied between 79°F to 96°F with an average humidity of 76%. Average monthly rainfall in the region ranges between 50 mm and 90 mm during the growing season (NWS, 2016).

Both RGB (Red, Green, and Blue) and MS (multispectral) sensors were used for this study. DJI Phantom 4 Pro (SZ DJI Technology Co., Ltd., Shenzhen, China) was used for RGB data collection. The weight of this UAS is 1.4 kg with a flight endurance of up to 30 minutes in mild weather conditions. It is equipped with a 3-axis gimbal-stabilized RGB sensor with 20 megapixels resolution, with an FOV of 74°. Multispectral data was captured using a multirotor platform, DJI Matrice 100 (DJI, Shenzhen, China). The weight of this UAS is 2.4 kg with a flight endurance of up to 25 minutes in mild weather conditions. A multispectral sensor, SlantRange 3p (Slantrange Inc, San Diego, CA, USA), was mounted on the UAV. SlantRange 3p sensor has a resolution of 1280 × 1024, 4.8 micro meter pixel size, 12 mm focal length, and 28° FOV. The sensor is equipped with an integrated solar spectrometer for frame-to-frame radiometrically accurate reflectance measurements. The sensor captures four spectral bands, including green, red, red-edge, and near-infrared bands (peak wavelengths are presented in Table 3.1). Table 3.2 presents flight specifications for both RGB and multispectral data. UAS considered in this study were equipped with a consumer-grade GPS which did not have satisfactory location accuracy for aerial mapping applications. To overcome this problem, six well-distributed permanent GCPs in the 2017 experiment and fifteen well-distributed GCPs in 2018 experiments (Figure 3.2) with high reflectance were installed over the study area. GCPs were surveyed every time the UAS data was collected using a dual-frequency, post-processed kinematic (PPK) GPS, model 20Hz V-Map Air (Micro Aerial Project L.L.C., Gainesville, FL). After each flight, the collected raw UAS data was processed using Agisoft Photoscan Pro software (Agisoft LLC, St. Petersburg, Russia). The details of UAS data processing for this study are described in section 2.2.

(**a**) (**b**)

Figure 3.1. Experimental field setup consisted of cotton in a skip or solid row pattern in (**a**) Year 2017 and (**b**) Year 2018. Experimental field setup is presented with RGB orthomosaic of the study area on June 7, 2017, and June 6, 2018.

(**a**) (**b**)

Figure 3.2. Distribution of ground control points (GCPs) on the experimental field in (a) Year 2017 and (b) Year 2018.

Table 3.1. Peak wavelength and FWHM for bands present in SlantRange 3p sensor.

SlantRange 3p sensor band	Peak wavelength (nm)	FWHM (nm)
Green	560	40
Red	655	35
Red-edge	710	20
Near-infrared	830	110

Table 3.2. UAS data collection timeline and sensor-wise flight specification.

Date	Flight Altitude (m)		Overlap (%)		Spatial Resolution (cm)	
	RGB	Multispectral	RGB	Multispectral	RGB	Multispectral
04/24/2017	20	30	85	75	0.51	0.93
05/05/2017	20	25	85	70	0.50	0.85
05/12/2017	20	25	85	70	0.51	0.81
05/20/2017	20	25	85	70	0.52	0.82
05/30/2017	20	25	85	70	0.51	0.85
06/07/2017	20	25	85	70	0.51	0.83
06/19/2017	20	25	85	70	0.52	0.81
07/05/2017	20	25	85	70	0.51	0.81
07/10/2017	20	25	85	70	0.50	0.83
07/18/2017	20	25	85	70	0.51	0.82
07/23/2017	20	25	85	70	0.51	0.82
04/23/2018	35	47	80	70	0.73	1.61
05/07/2018	35	47	80	70	0.69	1.65
05/14/2018	35	47	80	70	0.71	1.61
05/23/2018	35	47	80	70	0.71	1.64
06/01/2018	37	47	80	70	0.73	1.62
06/06/2018	35	47	80	70	0.72	1.61
06/13/2018	35	47	80	70	0.71	1.63
07/03/2018	35	47	80	70	0.71	1.61
07/09/2018	35	47	80	70	0.72	1.63
07/19/2018	35	47	80	70	0.70	1.62

3.3 Methodology

MS sensor-based CC estimation is considered more accurate and reliable compared to CC estimation using RGB sensors (Fernandez-Gallego et al., 2018). However, MS sensors are relatively more complex, expensive, and have sensitive detectors. The objective of this study is

twofold: the first objective is to compare various RGB-based CC estimation methods with MS sensor-based CC estimation, and the second objective is to improve RGB-based CC estimation and investigate the best suited RGB-based VI for CC computation. The procedure to compute percentage CC is presented in section A.1. An orthomosaic image (RGB or MS) was converted into a binary image after separating canopy from non-canopy. Later, percentage CC per grid was computed using Equation A.2 of Appendix-A (Figure A.2). Following the procedure, three different types of CC estimation were performed, namely, CC estimation using MS sensor, CC estimation using a pixel-wise classification of RGB images, and CC estimation using RGB sensor-based VIs. Finally, a morphological closing operation was performed to improve RGB-based CC estimations, and the best suited RGB-based VI to estimate CC was reported based on the comparison results.

3.3.1 CC estimation using MS sensor

As mentioned in section 3.1, MS sensor-based CC estimation is considered the most reliable in the literature. It uses normalized difference vegetation index (NDVI) to separate canopy from non-canopy (computed using Equation A.4 of Appendix-A (Rouse Jr et al., 1974)). Radiometric calibration of MS data was performed to compare the crop conditions accurately across datasets collected in varying lighting conditions throughout the growing season. SlantView (SlantRange Inc., San Diego, USA), the software developed for the SlantRange 3p MS sensor, was used to convert the raw UAS image values (digital numbers) to reflectance values. A detailed visual inspection was performed to find a threshold NDVI value to separate canopy from non-canopy in the images throughout the growing season regardless of the growth stage.

3.3.2 CC estimation using a pixel-wise classification of RGB image

A pixel-wise classification method was implemented to investigate the accurate CC estimation using an RGB sensor. With an appropriate spatial resolution of the image, pixel classification methods are considered highly accurate in distinguishing canopy from non-canopy (Booth et al., 2006; Hulvey et al., 2018; Patrignani and Ochsner, 2015). A pixel-level classification

method based on K-means clustering was used in this study. Initially, K-means clustering was applied to the RGB orthomosaics, considering five potential classes representing soil, shadow, cotton bolls, green canopy, and brown canopy, respectively (presented in Figure 3.3). After manually assigning the class labels to the clustered map, it was validated with manually collected ground-truth pixels from RGB orthomosaics using visual inspection. Later, soil, shadow, and cotton bolls were merged and assigned as a non-canopy class, and green and brown canopy classes were merged and identified as a canopy class. Pixel-wise classification-based CC estimation is a manually intensive process, as it relies on ground truth sample collection. Hence, the implementation was solely intended to investigate the maximum achievable performance using RGB-based sensors and to provide a reference of comparison to vegetation indices based CC estimation using RGB sensor. Following this point, CC estimation using a pixel-wise classification of RGB image will be referred to as RGB reference CC estimation.

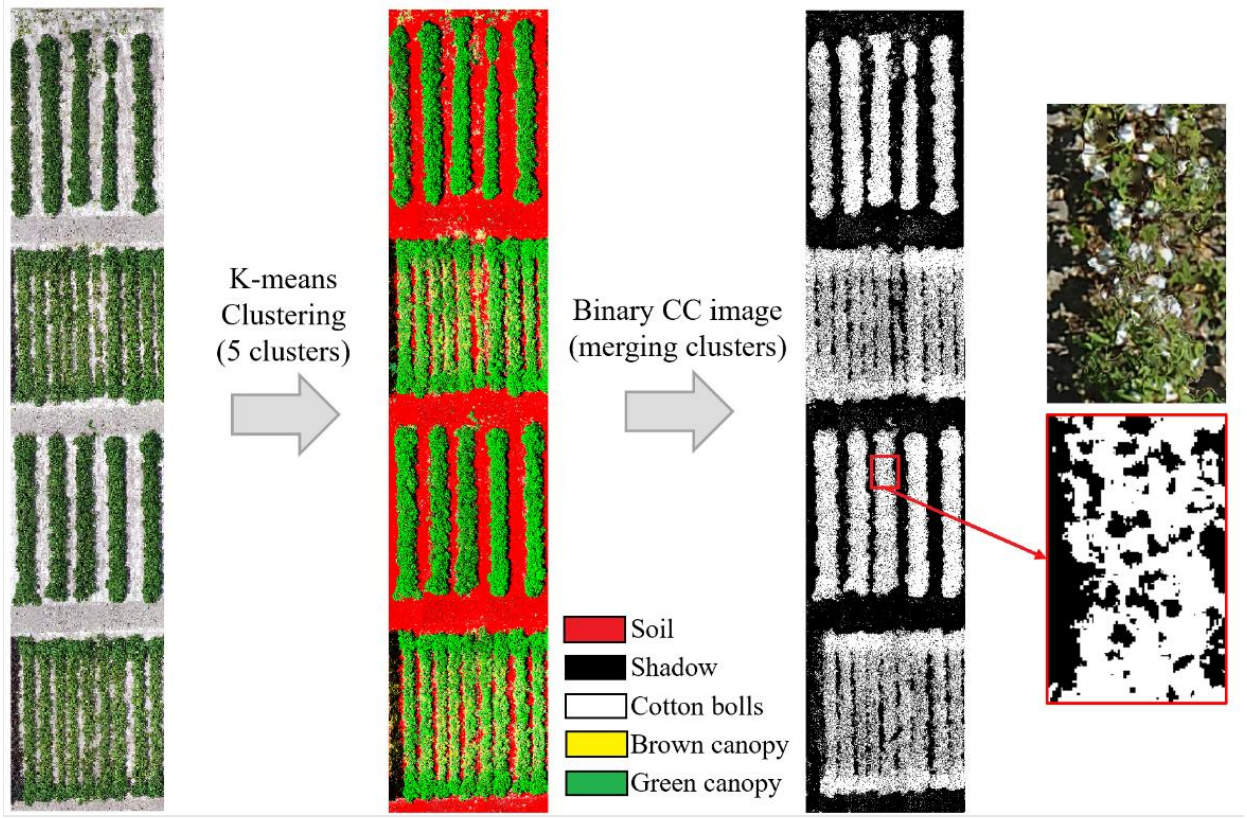

Figure 3.3. K-means clustering-based pixel classification method workflow where orthomosaic is classified into five classes, and later, classes are merged into two clusters: canopy and non-canopy. The RGB orthomosaic presented was captured on 6/19/2017.

3.3.3 CC estimation using RGB sensor-based vegetation indices

In this study, four different RGB-based CC estimation methods were considered, namely, Canopeo, excessive greenness index (ExG), modified green, red vegetation index (MGRVI), and red, green blue vegetation index (RGBVI) to generate the binary images (Table 3.3). The overall procedure to compute the CC binary map using RGB vegetation indices is presented inFigure 3.4. The Canopeo algorithm resulted in a binary map that separates canopy from non-canopy. However, applying vegetation indices over the RGB mosaics results in a grayscale image. Therefore, thresholding is required to transform the grayscale VI image into a binary image. Similar to NDVI, an empirical evaluation was performed to determine a threshold value for each VI that could separate canopy from non-canopy. The Otsu method was used for automatic thresholding in

previous studies (Marcial-Pablo et al., 2019). However, they were not applied over a multi-temporal dataset. The Otsu method resulted in accurate thresholding early in the season, as the image histogram mostly followed a bimodal histogram. Also, the variances of the spectral clusters were small compared to the mean difference. However, later in the season, thresholding by the Otsu method was questionable, as the variance in the spectral signature of the canopy increased over time, and the image no longer possessed a bimodal distribution (due to the emergence of new spectral classes such as open cotton bolls, and brown canopy).

Table 3.3. RGB image-based vegetation indices and their formula

Vegetation index	**Formula**	**Reference**
Canopeo	$canopy = (i_1 < \theta_2) \times (i_2 < \theta_1) \times (i_3 > \theta_3)$ $i_1 = \frac{red}{green}, i_2 = \frac{blue}{green}, \ i_3 = 2 \times green - blue - red$ $\theta_1 = 0.95, \ \theta_2 = 0.95, \theta_3 = 20$	(Patrignani and Ochsner, 2015)
ExG	$2G_{\mathrm{n}} - R_{\mathrm{n}} - B_{\mathrm{n}}$ $R_{\mathrm{n}} = \frac{R}{R+G+B}, G_{\mathrm{n}} = \frac{G}{R+G+B}, B_{\mathrm{n}} = \frac{B}{R+G+B}$	(Woebbecke et al., 1995)
MGRVI	$\frac{G^2 - R^2}{G^2 + R^2}$	(Bendig et al., 2015)
RGBVI	$\frac{G^2 - R \times B}{G^2 + R \times B}$	(Bendig et al., 2015)

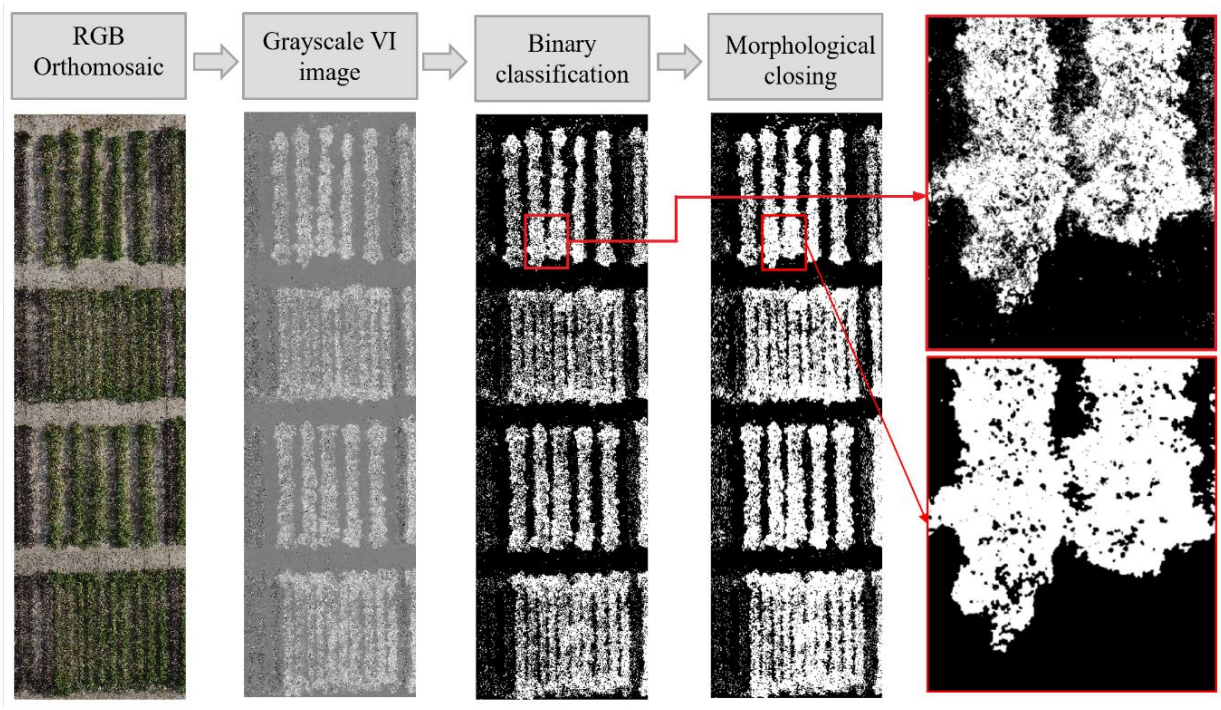

Figure 3.4. Procedure to generate binary map indicating canopy and non-canopy classes using RGB orthomosaic.

RGB-based VIs accurately identified healthy green canopy in the early growth stage. However, later in the season, their ability to identify the canopy deteriorated as the canopy started to change the color from green to brown (highlighted part of Figure 3.4), especially closer to senescence. Therefore, a morphological closing operation was performed to improve further the binary map generated using RGB-based vegetation indices. The morphological closing operation is a combination of dilation and erosion. It helps to remove small holes while keeping the separation boundary intact (Dougherty, 1992). For this experiment, a 3 x 3 kernel window over one iteration was used.

3.4 Results and discussion

The CC grid maps at each flight for 2017 and 2018 using MS sensors are presented in Figure 3.5 and, Figure 3.6 respectively. Visual inspection of the grid maps revealed that the average percentage canopy cover increased from ~10% on the first data collection date to ~90%

when it reached its plateau (June 19 and June 13 for 2017 and 2018, respectively). Later in the season, the average CC lowered down to ~60% between July 18 and July 23 for the 2017 dataset due to a common practice in the cotton fields known as defoliation which prepares the crop for harvesting. A similar effect was observed in the 2018 experiment between July 9 and July 19. Following the methodology presented in Figure 3.3 using RGB images, K-means clustering-based classification maps were generated considering five clusters which were later labeled to represent soil, cotton-boll, shadow, green canopy, and brown canopy. Subsequently, binary maps were generated by merging soil, cotton-boll, and shadow classes to indicate non-canopy and brown and green canopy to indicate canopy. The comparison for MS sensor-based CC and RGB reference-based CC is presented in Figure 3.7 and Figure 3.8 for the 2017 and 2018 experiments. MS sensor-based and RGB reference-based average CC values were highly correlated throughout the growing season (Figure 3.7 and Figure 3.8), with a high coefficient of determination (R^2 of 0.98 and 0.97 for 2017 and 2018, respectively). The results confirmed that it is possible to achieve the same level of performance using the RGB sensor as that of the MS sensors. However, the purpose of RGB reference CC estimation was to investigate whether it is possible to achieve the same level of performance as that of the MS-sensor CC estimation.

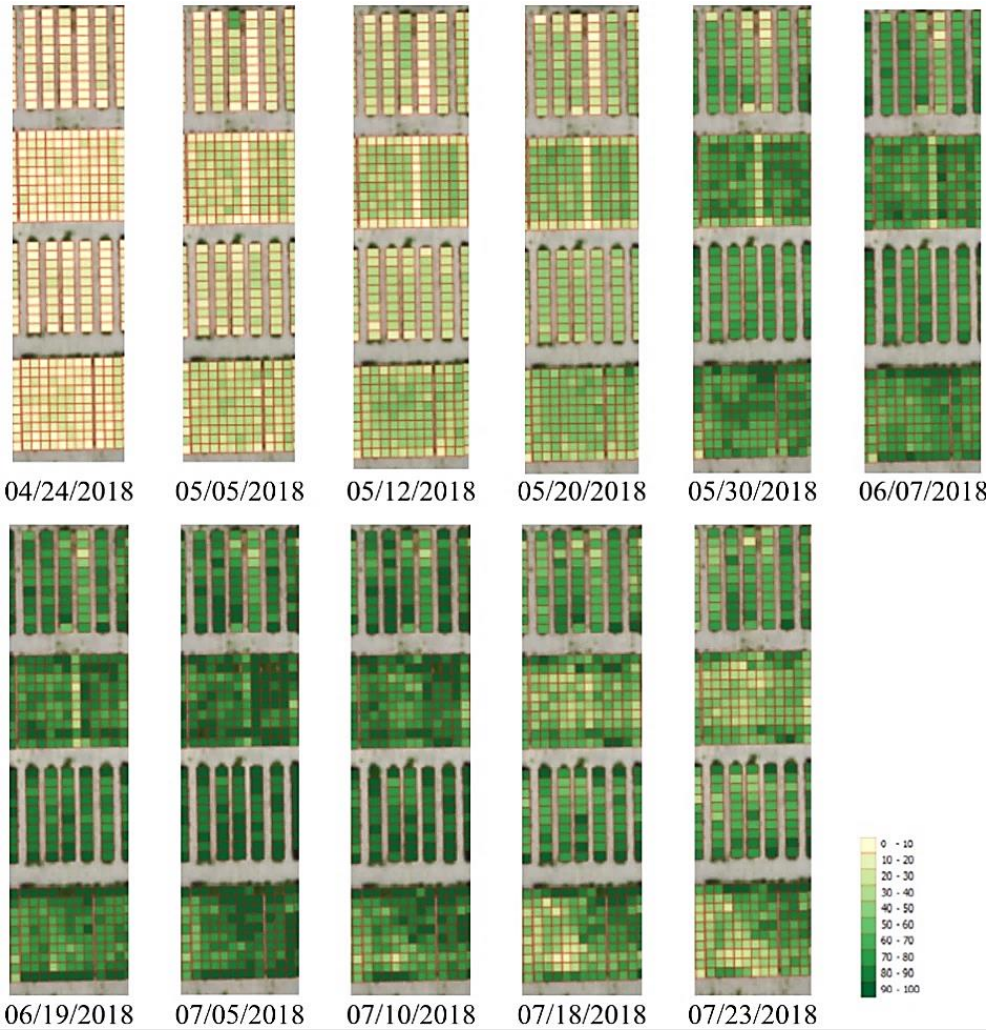

Figure 3.5. Canopy cover (CC) grid maps generated at each flight in the growing season using the multi-spectral sensor for the 2017 dataset.

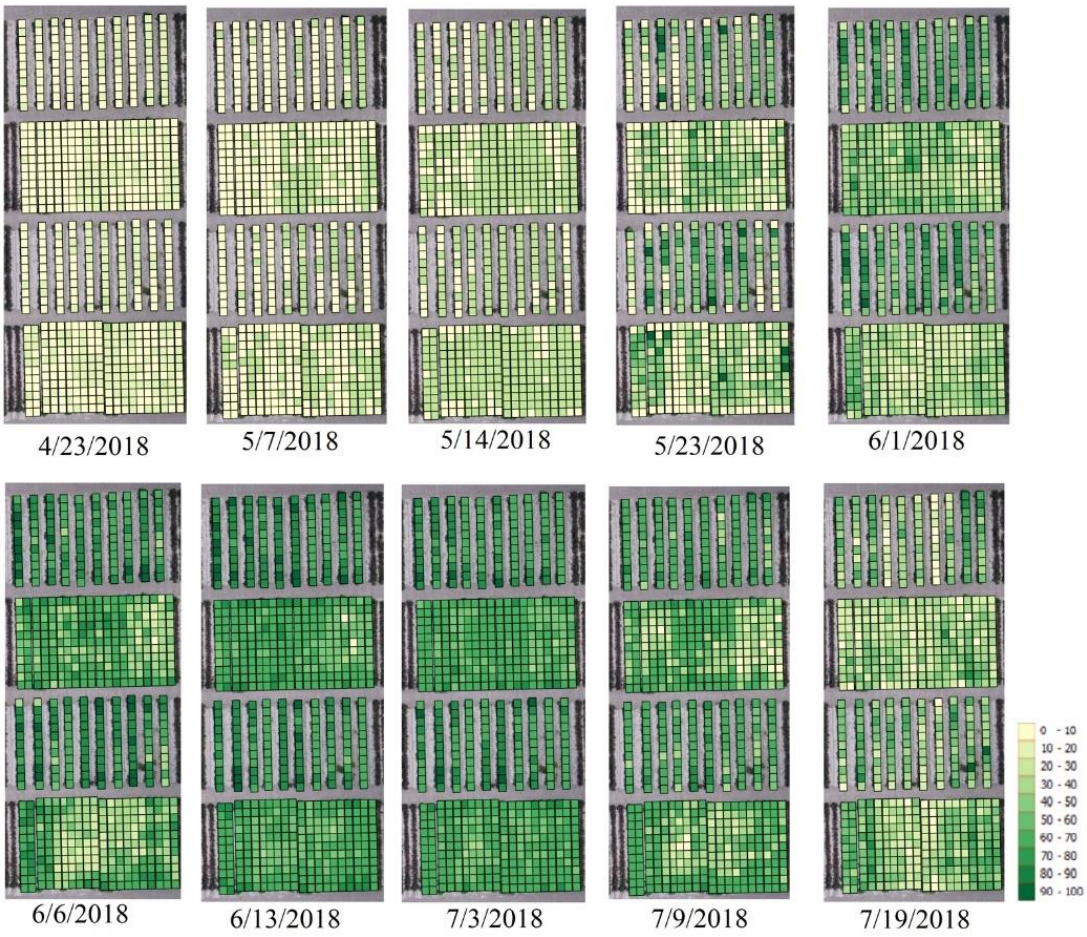

Figure 3.6. Canopy cover (CC) grid maps generated at each flight in the growing season using the multi-spectral sensor for the 2018 dataset.

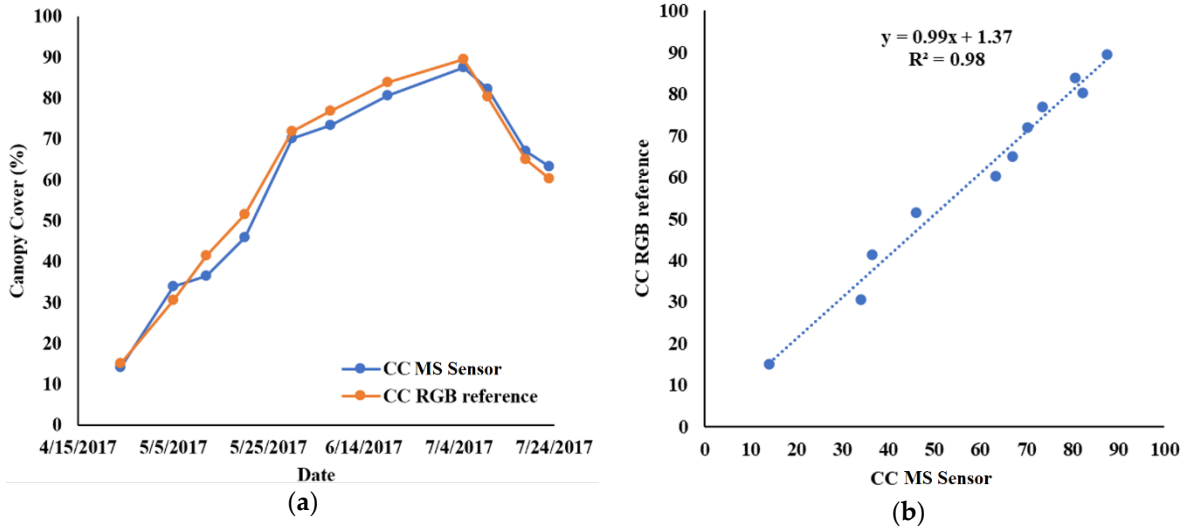

Figure 3.7. For the 2017 experiment, (**a**) Average multi-spectral (MS) sensor and RGB reference-based percentage canopy cover (CC) for each flight in the growing season and (**b**) Comparison of MS sensor and RGB reference-based percentage CC with R^2.

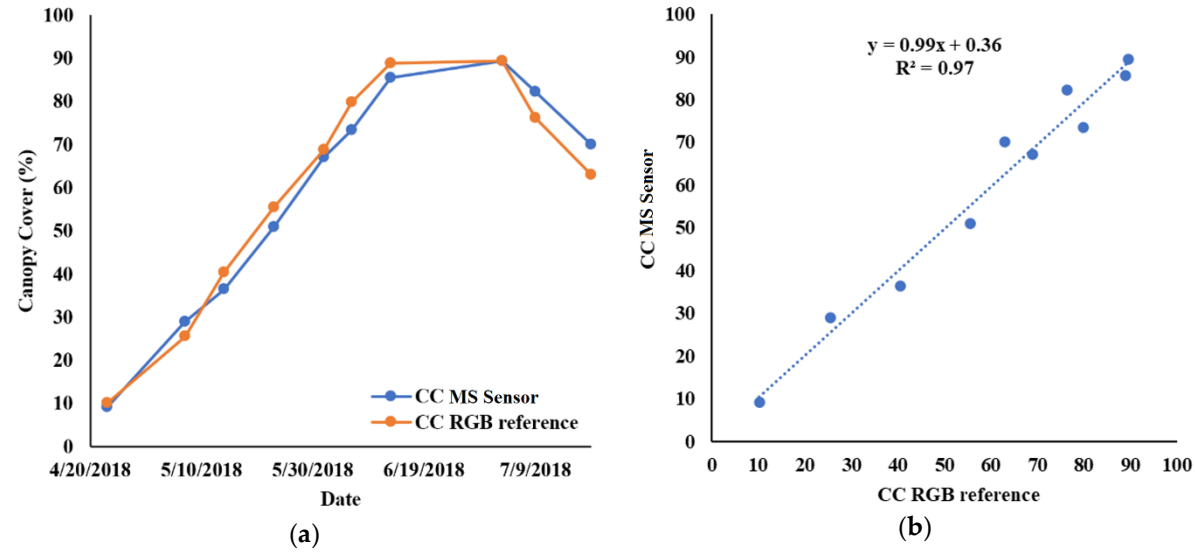

Figure 3.8. For the 2018 experiment, (**a**) Average multi-spectral (MS) sensor and RGB reference-based percentage canopy cover (CC) for each flight in the growing season and (**b**) Comparison of MS sensor and RGB reference-based percentage CC with R^2.

Four VIs were considered for computing CC using RGB images: Canopeo, ExG, MGRVI, and RGBVI. Along with the MS sensor-based average CC estimation per grid, average CC estimation per grid in the growing season for each RGB-based CC estimation method before and

after applying morphological closing (MC) is presented in Figure 3.9 and Figure 3.10 for 2017 and 2018 experiments, respectively. It can be observed from Figure 3.9 that early in the growing season, the average CC estimated by all the methods was in agreement with an average variation of less than 10% and followed a similar increasing trend with MS sensor-based estimation. However, CC estimation using Canopeo and ExG methods reached its peak on June 7, while MGRVI and RGBVI reached their peak on June 19. It was evident that ExG and Canopeo accurately identified a healthy green canopy. However, later in the season, because of the senescence, the canopy started to change color from green to yellow and eventually to brown; they failed to identify the matured canopy. Table 3.4 presents an average of RMSEs of thresholding-based CC estimation methods computed using all the datasets collected throughout the growing season in 2017 and 2018. The average RMSE of percentage CC turned out to be the highest for the Canopeo algorithm, even after applying morphological closing (13.3% for the 2017 dataset). RMSE for MGRVI was 3% lower compared to Canopeo, and it was able to identify mature canopy. However, it also reached its peak relatively early in comparison to MS sensor-based CC. RGBVI resulted in the most accurate method to estimate CC with an RMSE of 2.9%, especially later in the season; it outperformed other RGB-based methods. Morphological closing significantly improved the CC estimation with an improvement in RMSE ranging from 4% to 7%, and average RMSE with MS sensor-based CC estimation has substantially reduced (Table 3.4).

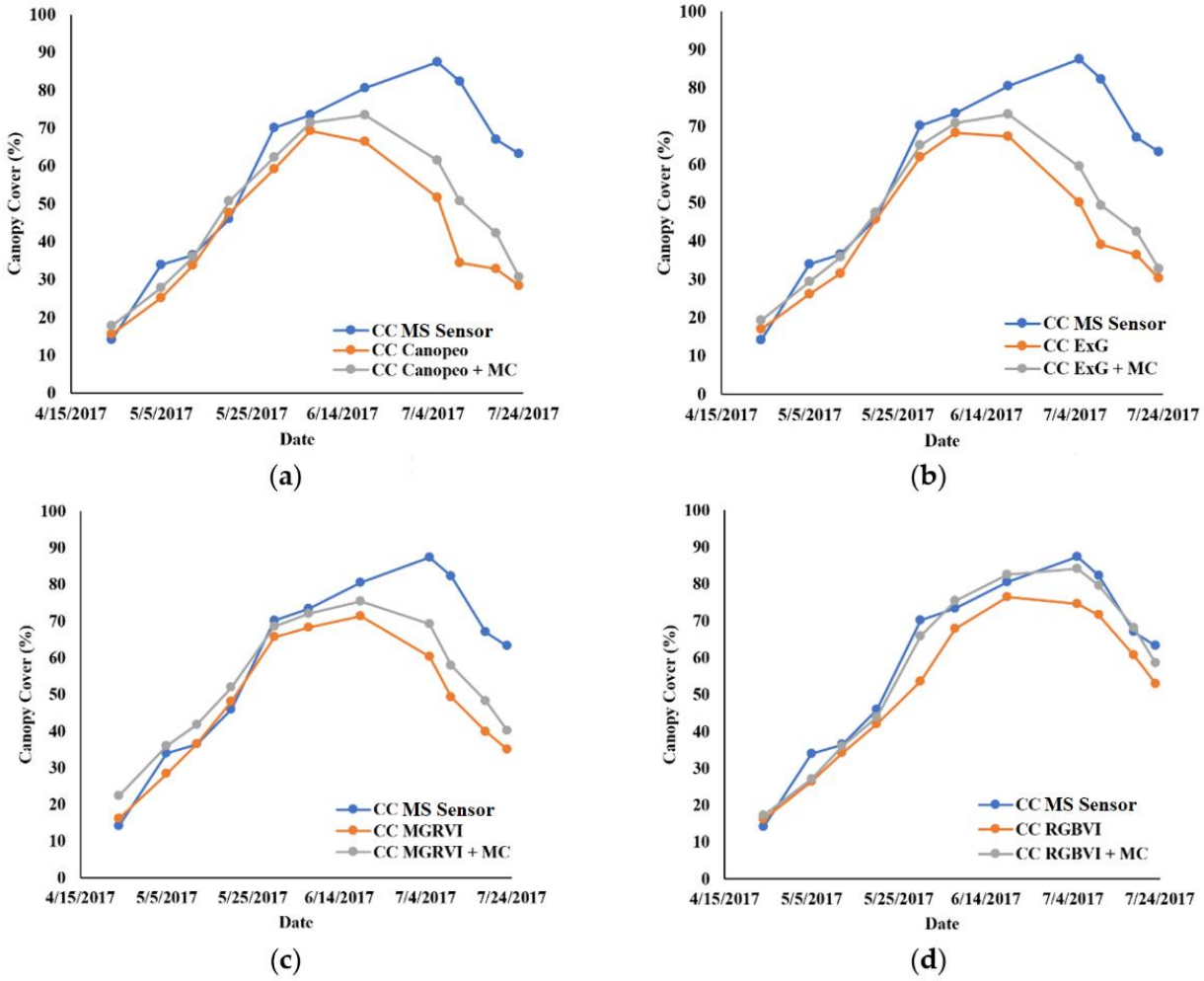

Figure 3.9. For the 2017 experiment, average canopy cover (CC) estimation per grid using multi-spectral (MS) sensor-based CC estimation throughout the growing season along with average CC estimation using (**a**) Canopeo, (**b**) Excess greenness index (ExG), (**c**) Modified green, red vegetation index (MGRVI), and (**d**) Red green blue vegetation index (RGBVI), before and after applying the morphological closing (MC) operation.

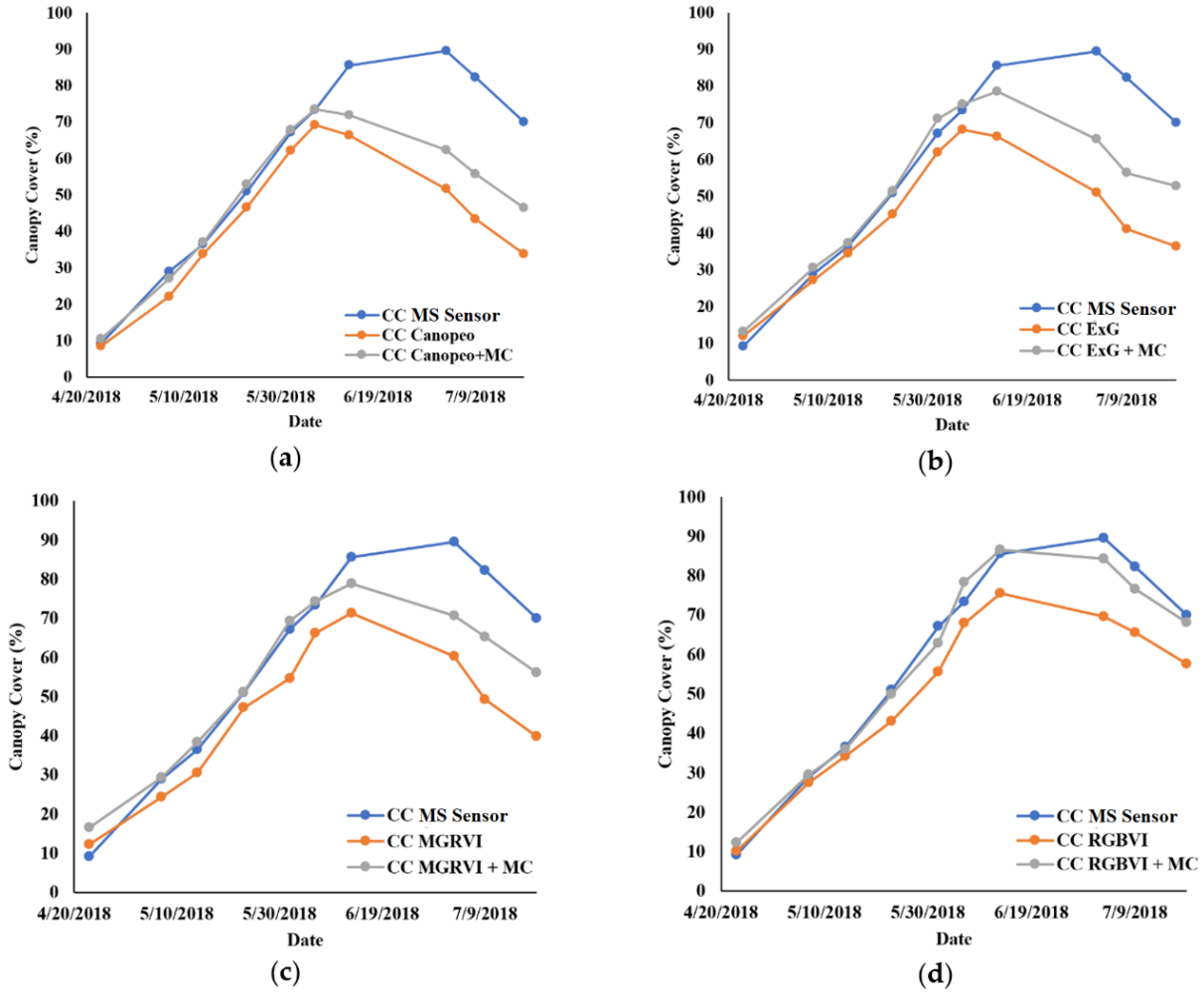

Figure 3.10. For the 2018 experiment, average CC estimation per grid using MS sensor-based CC estimation throughout the growing season along with average CC estimation using (**a**) Canopeo, (**b**) Excess greenness index (ExG), (**c**) Modified green, red vegetation index (MGRVI), and (**d**) Red green blue vegetation index (RGBVI), before and after applying the morphological closing (MC) operation.

Table 3.4. Average root mean square error (RMSE) of thresholding-based canopy cover (CC) estimation methods with respect to multi-spectral (MS) sensor-based CC estimation (%) throughout the growing season in 2017 and 2018.

RGB-based method	Average RMSE with respect to MS sensor-based CC estimation (%)			
	2017 experiment		2018 experiment	
	Before MC	After MC	Before MC	After MC
Canopeo	17.87	13.34	15.56	9.73
ExG	16.97	13.00	15.51	8.67
MGRVI	13.11	10.35	14.34	6.95
RGBVI	7.44	2.94	8.85	2.82

A similar trend was observed in the performance of thresholding-based CC estimation methods in the 2018 experiment (Figure 3.10). Canopeo and ExG methods had an RMSE of 9.7% and 8.7 %, respectively (Table 3.4) but 4% higher than the 2017 experiment. RGBVI resulted in the most accurate CC estimation method amongst all, with an RMSE of 2.8% after applying morphological closing operation. The morphological closing operation resulted in relatively lower RMSEs in the 2018 experiment compared to the 2017 experiment. In the 2018 experiments, the spatial resolution of RGB images was 0.2cm lower than in the 2017 experiments. A high resolution often leads to more details being observed, which could be undesirable when the information class under consideration is more general; consequently, a decrease of the GSD (Table 3.2) might have contributed to better classification and later filtering performance in 2017 compared to 2018.

Recent years have witnessed an upsurge in the UAS and sensor technology that made it possible to collect high temporal and spatial resolution data over the crops throughout the growing season. The main objective of this study was to provide a comparison framework between MS sensor-based CC estimation and RGB-based CC estimation, as scarce attention has been paid to exploring different VIs generated using UAS-based sensors to compute the canopy cover. MS sensor-based CC estimation is relatively accurate and stable compared to RGB-based CC estimation. However, the accuracy of NDVI is a function of the type and quality of the multispectral sensor used to collect the image. Temporal NDVI maps were generated from

multispectral data collected using a SlantRange 3p sensor that was radiometrically calibrated. While RGB-based CC estimation was comparable to MS sensor-based CC estimation in the early season, experiments in 2017 and 2018 confirmed that it performed inadequately when the plant color deviated from green in the late season.

Except for the Canopeo method, all other RGB VIs considered in this study required a manual threshold to separate canopy from non-canopy. As mentioned in section 3.3, the Otsu method could not be used for automatic thresholding in this study. Consequently, RGB and MS sensor-based VIs were visually inspected to select a threshold value for all the images in the growing season. Since this study was limited to cotton crops, the threshold value might differ for other crops, and there might be a different trend observed in response to the senescence in the growing season. In the future, an efficient thresholding method that can classify canopy regardless of growth stage would help automate the process.

As previous studies have affirmed that RGB-based CC estimation efficiently works early in the season (Fang et al., 2016; Marcial-Pablo et al., 2019), it was also observed that both MS and RGB-based CC estimation were in agreement early in the season. Moreover, in previous studies, MS sensor-based CC estimation was more accurate in the later season than RGB-based CC estimation (Marcial-Pablo et al., 2019). MS sensor-based CC estimation increased as the season progressed, but RGB-based CC estimation peaked early and started to drop with an average rate of 7% and 8% per week for the 2017 and 2018 experiments, respectively. The inadequacy of RGB-based CC estimation in the previous studies led to the question, “is it possible to achieve the same level of accuracy using RGB-based CC estimation as that of the NDVI-based CC estimation?”. To address this question, a K-means clustering-based CC estimation method was implemented, which was tested using the ground truth samples for canopy and non-canopy classes. K-means clustering-based approach resulted in CC estimation highly correlated with MS sensor-based CC estimation throughout the growing season (R^2 of 0.98 and 0.97 for 2017 and 2018, respectively). However, the clustering or classification-based approach is computationally extensive, especially in their parameter tuning. Additionally, supervised methods require ground truth collection, which is labor-intensive and time-consuming. Consequently, this study was focused on improving RGB-

based CC estimation using VIs. Towards the senescence, when the canopy started losing its green color, RGB-based VIs could not identify the canopy pixels, which resulted in CC maps with narrow isthmuses, and thin protrusions. The morphological closing operation proved to be a solution to this problem and helped fill tiny holes and keep the boundary of the canopy intact. It was noticed in both the experiments (2017 and 2018) that applying morphological closing operation reduced the average RMSE of the RGB-based CC estimation by 4% in 2017 and 5% in the 2018 dataset. An affordable alternative to the MS sensor can be provided to estimate the CC with the proposed study. To have higher accuracy of CC estimation, several studies in the past have relied on MS sensors, as it provides more spectral information. This study explored the potential of an alternate approach of enhancing CC estimation accuracy by improving the existing image processing technique, which requires only RGB information. In the future, the methodology will be investigated on other crops as there might be a different trend observed in response to the senescence in the growing season.

3.5 Conclusion

A comparative study was performed to evaluate CC estimation using an RGB sensor. With multi-year CC analysis, MS sensor-based CC estimation was used as a reference to provide a stable and accurate estimation. The correlation of RGB reference-based CC estimation with MS sensor-based CC estimation ensured the feasibility of using RGB sensor to match MS sensor-based CC estimation. Analysis of RGB-based methods suggested that RGBVI was more tolerant to the change in color of the canopy when the canopy started to senescence. Moreover, when morphological closing was applied, RGBVI-based CC estimation was similar to MS sensor-based CC estimation with an average RMSE of less than three percent. CC is a good predictor variable for plant growth parameters. As multispectral sensors have relatively sensitive detectors and are more complex and expensive, proposed RGB-based CC estimation could provide an affordable alternate to agriculture scientists and breeders.

4. MACHINE LEARNING BASED COTTON YIELD ESTIMATION FRAMEWORK USING MULTI-TEMPORAL UAS DATA

4.1 Background

One of the main objectives of cotton breeding research is to select genotypes suitable for specific environments. For example, in arid and semi-arid areas, the focus is to develop cotton genotypes resistant to water stress due to the dry climate and high irrigation costs. Traditionally, cotton breeding research has focused on manual field-based evaluation approaches that require the entire cotton field to be harvested, and later the best performing genotypes are selected based on ranking (Clement et al., 2014; Iqbal et al., 2008; Kazerani, 2012; Shaukat et al., 2013). As this process is cumbersome, the scale of the field experiment is constrained by the limited availability of resources. As a result, developing automated genotype selection techniques that do not require the entire field to be harvested can benefit cotton breeding research.

Remote sensing-based crop yield estimation methods have the potential to help develop tools to improve genotype selection efficiency. Recent developments in exploiting UAS data for cotton yield estimation have revealed that UAS-based remote sensing has the potential to accurately estimate crop yield (Weiss et al., 2020). Previous research done in this direction demonstrated a correlation of crop yield with selective spectral bands and vegetation indices derived from images collected using RGB and multi-spectral sensors onboard a UAS (Nebiker et al., 2016; Stroppiana et al., 2015; Zhou et al., 2017). Later, UAS based image-driven crop canopy attributes such as canopy height were also utilized to estimate crop yield (Feng et al., 2018; Stanton et al., 2017). Recent years have witnessed an increasing application of machine learning regression models such as artificial neural network (ANN), support vector regression (SVR), random forest regression (RFR), and Gaussian process regression to develop empirical relationships between crop yield and canopy attributes because they are capable of handling the nonlinear relationship

Content of this chapter is published as follows: Ashapure, A., Jung, J., Chang, A., Oh, S., Yeom, J., Maeda, M., ... & Smith, W. (2020). Developing a machine learning based cotton yield estimation framework using multi-temporal UAS data. *ISPRS Journal of Photogrammetry and Remote Sensing*, *169*, 180-194.

between input features and the output target (Gandhi et al., 2016; Gopal and Bhargavi, 2019; Yu et al., 2016). Therefore, this study aims to develop a novel machine learning framework to estimate the crop yield and determine the optimal input feature set for accurate yield estimation. Furthermore, the objective is to develop a model with the flexibility to accommodate multi-year and multi-location data for yield estimation.

4.1.1 Scope and contribution

Studies utilizing UAS derived canopy attributes for yield estimation in the literature are limited to exploiting a single or relatively few regression parameters. This study, therefore, explores the potential of UAS derived multi-temporal vegetation indices and canopy attributes to estimate the crop yield. Recently, deep learning models are gaining popularity for accurate crop yield prediction (Tri et al., 2017; Wang et al., 2018). Deep learning models such as deep Gaussian processes (You et al., 2017) and deep convolutional neural networks (CNN) (Khaki et al., 2019; Kim et al., 2019) have been utilized to develop crop yield prediction models. Moreover, hybrid deep learning models combining CNN with recurrent neural networks (RNN) are also being used to improve yield prediction accuracy (Khaki et al., 2020). However, deep models are primarily utilized for large-scale yield prediction utilizing multi-year weather data along with satellite data. The large size of the network architecture means more trainable parameters, and it is recommended that the number of training samples should be at least ten times the number of trainable parameters in any deep learning model (Miotto et al., 2018). Consequently, the success of deep learning-based yield estimation models is mainly dependent on the availability of training samples which makes them unsuitable for small-scale experiments having limited training samples.

The objective of this study was to present a novel framework that combines UAS derived multi-temporal vegetation indices and canopy attributes with qualitative information to predict the crop yield. The proposed machine learning framework is based on ANN architecture. Neural network models can implicitly detect complex nonlinear relationships between independent and dependent variables in a complex system without requiring explicit mathematical representations (Sargent, 2001). The main contributions of this study are:

- Proposing a framework to estimate crop yield utilizing UAS derived canopy attributes using three state-of-the-art machine learning regression models, namely, ANN, SVR, and RFR, and compare their efficacy.

- Redundant features removal from the input feature-set and computing relative significance of each feature using sensitivity analysis.

- Determining how early in the season the proposed model can accurately predict crop yield.

4.2 Study area, sensors, and platforms

Field experiments were conducted at the Texas A&M AgriLife Research and Extension Center (27°46'59" N, 97°34'13" W) in Corpus Christi, TX, USA. The total area of the experimental field was approximately 1.6 acres. Thirty cotton genotypes (Table 4.2) from Texas A&M University Cotton Breeding Program were planted on April 1, 2016, and machine harvested on August 20, 2016. Soil types in the study site are Victoria Clay series soils (Victoria-Lattas-Clareville). Provided the experimental field was in a coastal area, wind speed and rain were the potential factors to be considered before every flight. Most flights were conducted between 10:00 AM to 2:00 PM. Moreover, the temperature variation throughout the growing season varied between 79°F to 96°F with an average humidity of 76%. Average monthly rainfall in the region ranges between 50 mm and 90 mm during the growing season (NWS, 2016). Machine harvested data were employed as ground reference data in this study. A total of 805 plots were used, and the yield value ranged from 0.4 to 14.3lbs with an average of 6.65lbs per plot. Figure 4.1 (a) shows the location of the study area and the aerial image of the site in the inset image. The whole field was divided into 1m x 10m size plots to compute various vegetation indices and canopy attributes, which can be observed in the zoomed area of Figure 4.1 (b). The experiment field was divided into two sections based on irrigation conditions: dryland and irrigated (Figure 4.1 (a)).

Both RGB (Red, Green, and Blue) and MS (multispectral) sensors were used for this study. DJI Phantom 2 Vision + (SZ DJI Technology Co., Ltd., Shenzhen, China) was used for RGB data collection. The weight of this UAS is 1.0 kg with a flight endurance of up to 25 minutes in mild

weather conditions. It is equipped with a 3-axis gimbal-stabilized RGB sensor with 14 megapixels resolution, with an FOV of 85°. Multispectral data was captured using a multirotor platform, 3DR IRIS (3D Robotics, Berkeley, CA, USA). A multispectral sensor, Tetracam ADC snap (Tetracam Inc., Chatsworth, CA, USA), was mounted on a UAV. Tetracam ADC snap sensor has a resolution of 1280 × 1024, 8.43 mm focal length, and 28° FOV. The sensor captures three spectral bands, including green, red, and near-infrared bands (peak wavelengths are presented in Table 4.1). The UAS data was collected in the 2016 growing season, from April to August. Beginning April 7, 30 flights were conducted before the crop was harvested on August 20 (Table 4.3). Multispectral data collection occurred every seven to ten days compared to four to seven days for the RGB sensor. Table 4.3 presents flight specifications for both RGB and multispectral data. UAS considered in this study were equipped with a consumer-grade GPS which did not have satisfactory location accuracy for aerial mapping applications. To overcome this problem, fifteen well-distributed GCPs in 2018 experiments (Figure 4.2) with high reflectance were installed over the study area. GCPs were surveyed every time the UAS data was collected using a dual-frequency, post-processed kinematic (PPK) GPS, model 20Hz V-Map Air (Micro Aerial Project L.L.C., Gainesville, FL). After each flight, the collected raw UAS data was processed using Agisoft Photoscan Pro software (Agisoft LLC, St. Petersburg, Russia). The details of UAS data processing for this study are described in section 2.2, and canopy attributes and vegetation indices computation procedure is presented in Appendix A.1.

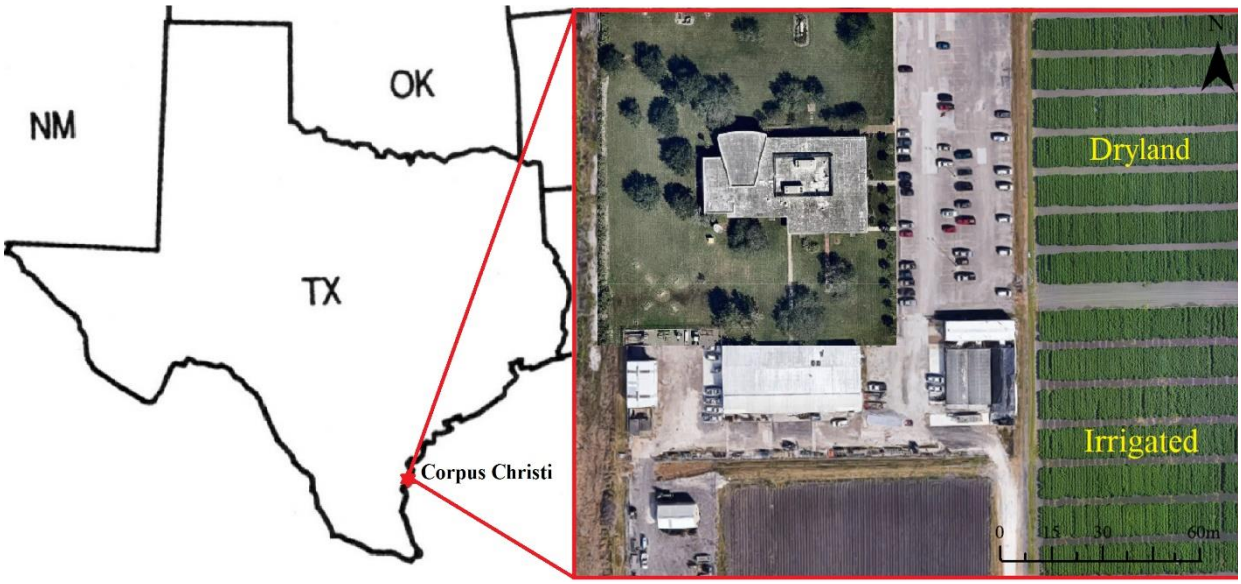

(a)

(b)

Figure 4.1. (a) Location of the study area with the aerial image of the site in the inset where half of the field was under dryland condition, and another half was under irrigation, (b) A segment of the field with overlaid line segments 1m x 10 m each.

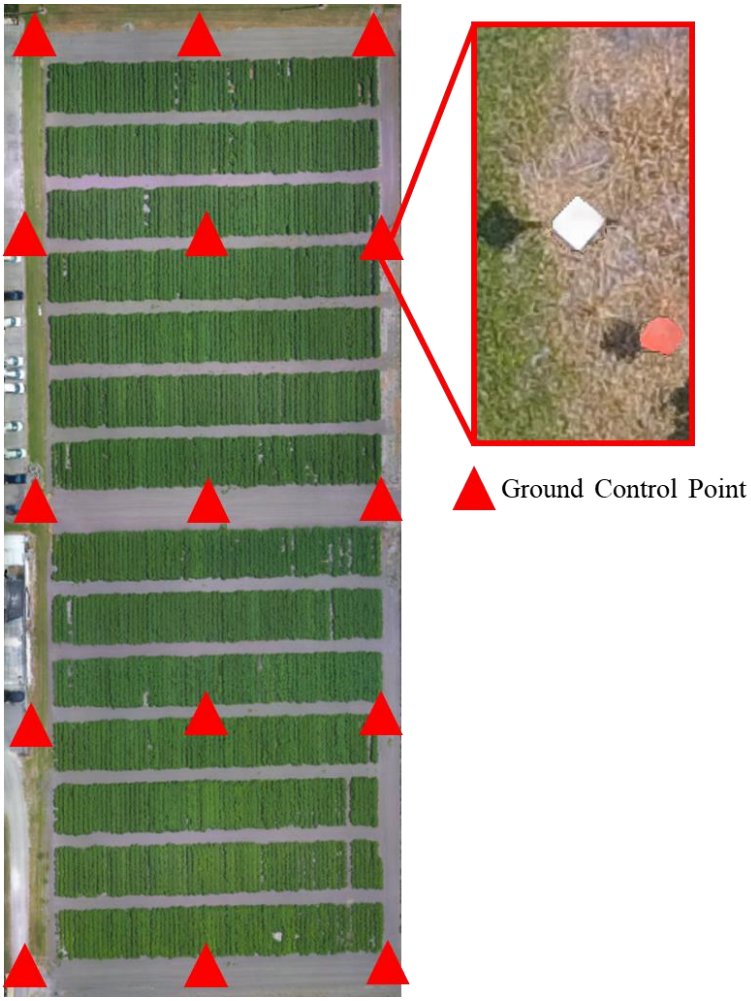

Figure 4.2. Distribution of permanent ground control points (GCPs) in the experimental field.

Table 4.1. Peak wavelength and full width at half maximum (FWHM) for bands of Tetracam ADC snap sensor.

Tetracam ADC snap sensor band	Peak wavelength (nm)	FWHM (nm)
Green	540	100
Red	650	320
Near-infrared	820	160

Table 4.2. List of cotton genotype varieties planted.

Genotype no	Genotype Name/Code
1	10 WE-11
2	12 BB 2139
3	13Q-18
4	13Q-51
5	TAM 11K-13 ELSU
6	10x-64
7	11 HF4IPSC-21-01
8	TAM WK-11 Lo
9	11-11-307BB
10	11-21-703S
11	13-2-501FQ
12	7-7-1303CT
13	7-7-519CT
14	CA 4001
15	CA 4002
16	CA 4003
17	CA 4004
18	DPL 491
19	PSC 355
20	TAMCOT 73
21	5235
22	5237
23	5241
24	5338
25	5435
26	5542
27	STV 6182
28	PHY333
29	DPL 1044
30	UA 103

Table 4.3. UAS data collection timeline and sensor-wise flight specification.

Date	Flight Altitude (m)		Overlap (%)		Spatial Resolution (cm)	
	RGB	Multi	RGB	Multi	RGB	Multi
04/07/2016	30	40	80	60	1.05	2.09
04/12/2016	30	40	90	60	1.08	2.16
04/15/2016	35	N/A	90	N/A	1.28	N/A
04/22/2016	35	40	90	60	1.32	2.14
04/27/2016	35	35	90	60	1.3	2.11
05/06/2016	35	40	90	60	1.34	2.14
05/16/2016	37	40	90	60	1.38	2.16
05/20/2016	35	40	90	60	1.34	2.18
05/23/2016	37	N/A	90	N/A	1.42	N/A
05/27/2016	40	N/A	90	N/A	1.42	N/A
05/31/2016	40	50	90	90	1.46	2.71
06/02/2016	35	N/A	90	N/A	1.34	N/A
06/07/2016	30	50	90	90	1.2	2.68
06/14/2016	25	50	90	90	0.898	2.7
06/17/2016	25	45	90	90	0.916	2.61
06/20/2016	20	45	90	90	0.753	2.55
06/23/2016	25	40	90	85	0.875	2.42
06/27/2016	20	45	90	90	0.797	2.52
06/30/2016	18	N/A	90	N/A	0.714	N/A
07/08/2016	25	N/A	90	N/A	0.975	N/A
07/13/2016	25	N/A	90	N/A	0.905	N/A
07/16/2016	22	45	90	90	0.836	2.6
07/19/2016	35	45	90	90	1.29	2.6
07/21/2016	22	45	90	90	0.839	2.6
07/25/2016	20	45	90	90	0.809	2.51
07/28/2016	20	N/A	90	N/A	0.767	N/A
08/02/2016	15	42	90	90	0.596	2.44
08/08/2016	15	45	90	90	0.599	2.6
08/12/2016	13	45	90	90	0.492	2.6
08/18/2016	13	45	90	90	0.596	2.62

4.3 Methodology

A flowchart outlining the overall methodology is presented in Figure 4.3. The first step included UAS data collection using RGB and multispectral sensors, along with the GPS survey of the ground control points (GCPs). In the second step, raw images and GCP coordinates were provided to the SfM photogrammetric processing software, and orthomosaics and DEMs were generated. Canopy attributes were generated from orthomosaics and DEMs in the third step. In the fourth step, canopy attributes were estimated for each day using the radial basis function (RBF) neural network. In the final step, ANN modeling was employed to estimate the yield using the optimal subset of input variables.

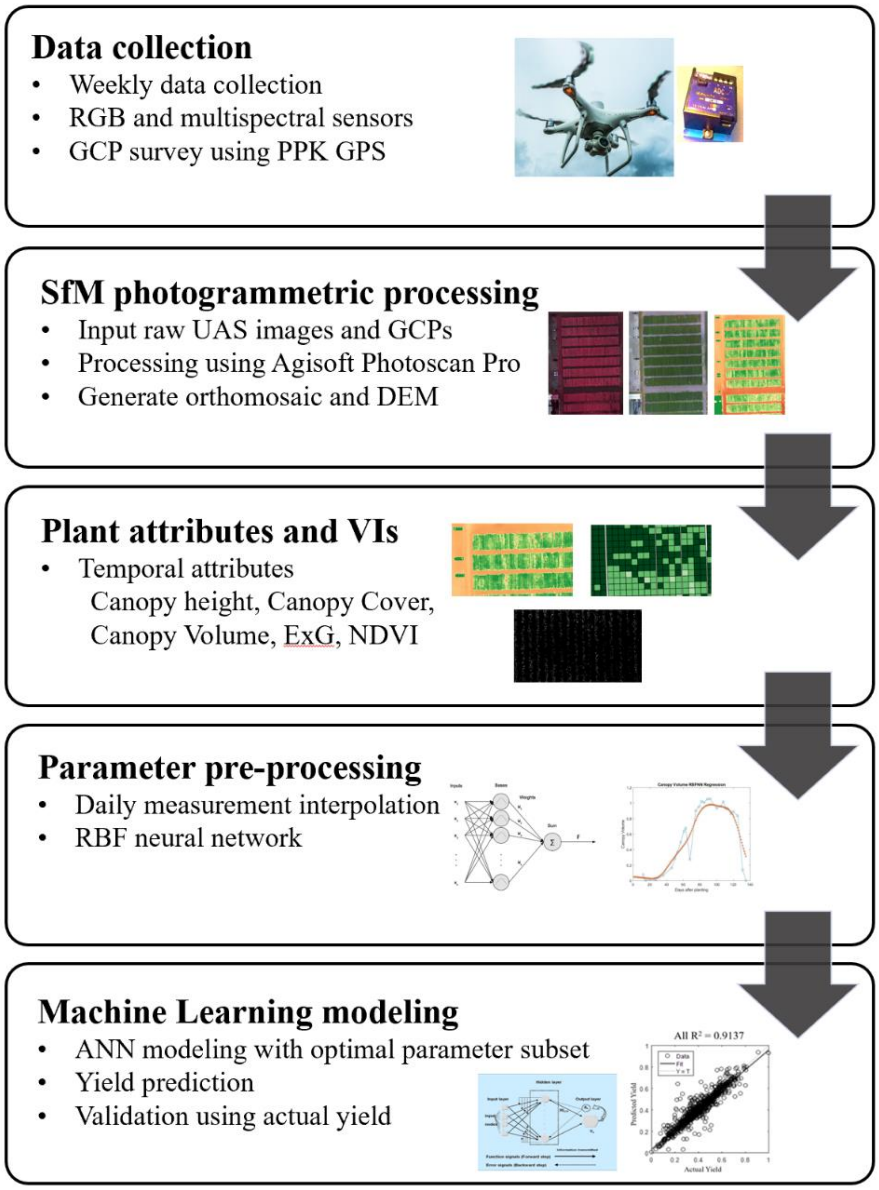

Figure 4.3. Overall process workflow of UAS based crop yield estimation.

UAS data collection is highly application-dependent. For yield estimation, it is very critical to account for the growth behavior of the crop under consideration. Especially for a unique crop like cotton, which is a tropical perennial plant grown and managed as an annual crop. Cotton has an indeterminate growth habit which means its vegetative and reproductive growth has an overlap, requiring growth regulators to maintain the crop. The developmental phases of cotton can be divided into five main growth stages, namely, germination and emergence, seedling establishment,

leaf area and canopy development, flowering and boll development, and maturation (Stewart et al., 2009). The growth curve of a cotton plant follows a typical sigmoid curve which has a slow growth rate in the initial phase, succeeded by an exponential growth rate for leaf area, canopy, flowering, and boll development, followed by a slow growth rate in the maturation phase. Under favorable moisture and temperature conditions, the growth of the cotton plant follows a well-defined and consistent pattern expressed in days. Cotton growth milestones are often given in terms of days after planting or between growth stages. Ritchie et al. (2007) provided a general growth pattern of the cotton plant as presented in Figure 4.4. As presented in Figure 4.4, the red markers represent the optimal number of data points to accurately capture the cotton growth curve. For effective yield estimation, collected UAS datapoints must represent the shape of the growth curve. Consequently, the data collection should adopt a systematic targeting of critically sensitive periods as suggested by knowledge of crop physiology.

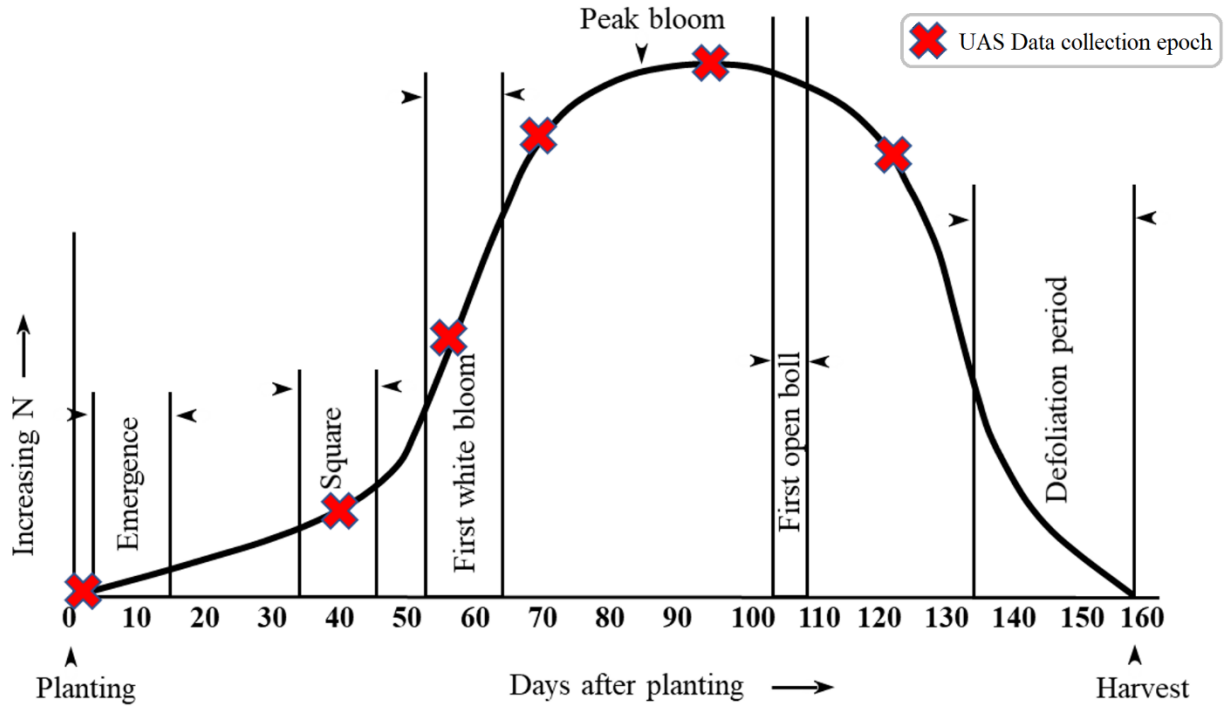

Figure 4.4. A typical growth curve of the cotton plant following a sigmoid curve, where the x-axis represents days after planting and the y-axis represent the nitrogen content in the plant. This figure is reproduced from Ritchie et al. (2007), where red markers are the optimal number of data points to accurately capture the cotton growth curve.

4.3.1 Parameter preprocessing

In addition to crop physiology, UAS data collection also depends on various factors such as the availability of the crew, availability of resources, weather conditions, and availability of the field. As a result, maintaining the same time of data collection across multiple years is practically not viable. Thus, an interpolation technique was used to determine daily estimates for crop canopy attributes. Later, measurements at any time interval of interest can be extracted from the daily measurements. In this study, a radial basis function neural network (RBFNN) based regression model was used for daily measurement estimation. RBFNNs are single-pass learning models with high accuracy interpolation capability that have been successfully utilized for interpolation problems (Dash et al., 2016). They can efficiently handle noise in the input data, which is particularly useful for remote sensing applications (Pandey et al., 2012; Xiao-Hua et al., 2009). Similar to 2-layer ANNs, RBFNNs include an input layer fully connected to a hidden layer with a Gaussian radial basis function as the activation function (Figure 4.5). Each input vector is supplied to each basis in the hidden layer. The output of the hidden layer is used to compute a weighted sum to get the output which is the daily interpolated value of the parameter.

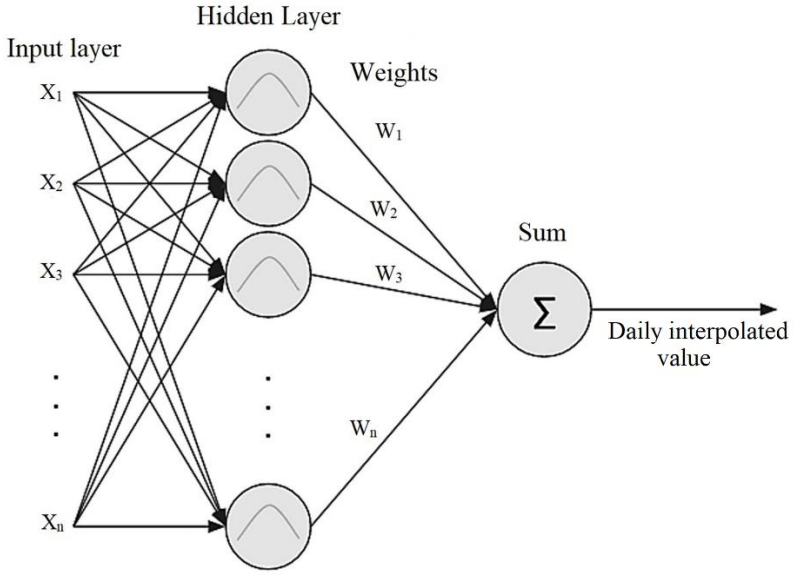

Figure 4.5. Architecture of the radial basis function neural network (RBFNN) based regression model.

RBFNN can learn to approximate the underlying trend using many Gaussian curves. Shapes of curves are adjustable by changing the weights or centers. This suggests that RBF can be used to approximate any unknown nonlinear function given observational data samples (Hien and Huan, 2015). This dissertation also aims to provide information on an optimal number of data points needed to accurately compute the daily measurements for canopy attributes. An experiment was conducted to compute daily measurement estimates, where a part of the available data was used for deriving the interpolation model, and the remaining data were used for the evaluation of the same. Two methods were considered in this study based on uniform interval and based on crop physiology. Following daily measurement estimation, correlation analysis was performed categorically to examine the degree of correlation between the canopy attributes, vegetation indices, and open cotton boll attributes. Correlated features were discarded to remove the redundancy from the input feature set.

4.3.2 Machine Learning model

Machine learning regression algorithms have been successfully applied to remote sensing applications since they can generate adaptive, robust relationships, and trained machine learning models are very fast to apply (Hultquist et al., 2014; Rodriguez-Galiano et al., 2015; Verrelst et al., 2012; Were et al., 2015). Three machine learning-based regression models were considered in this study, namely, ANN, SVR, and RFR. Numerous studies have demonstrated that these machine learning models are among the most powerful machine learning regression methods to handle the strong nonlinearity present in remote sensing datasets. Although ANNs are prone to over-fitting during training without careful parameter tuning, though it was still considered in this study because of their ability to efficiently identify the importance of different independent variables for more accurate crop yield estimation (Chlingaryan et al., 2018). Moreover, traditional linear regression models lack the ability to model data consisting of nonlinear features. ANN consists of a collection of simulated neurons placed in a multi-layer arrangement connected with other neurons via weighted links which help them deal with the non-linearity in the input data. ANNs are known to learn correlated patterns between inputs and the corresponding target (Chlingaryan

et al., 2018). An ANN regression model with three layers (one input layer, one hidden layer, and an output layer) was considered in this study. To prepare the input dataset using VIs, canopy attributes, and qualitative attributes, a feature vector was formed by concatenating weekly extracted values of all the temporal features followed by non-temporal and qualitative features (Figure 4.6) that constituted an input sample, with the machine harvested yield per plot used as a target feature. Further, the prepared input samples were divided into a training set and a test set with 80% and 20% proportions, respectively. The training samples were used to train the machine learning models using k-fold cross validation process (Fushiki, 2011). In the k-fold cross-validation process, the data is randomly partitioned into k equal size sub samples. Each of the k sub samples is considered as a validation set, and the remaining sub-samples are considered for training. The cross-validation process is then repeated k times. The average of k results provides the training and validation accuracies of the algorithm (Jung and Hu, 2015). In this study, 10-fold cross-validation was used.

To compare the efficacy of the ANN regression model, two machine learning regression methods were considered as references, namely, support vector regression (SVR) and random forest regression (RFR). Support vector machines are popular machine learning models applied efficiently in various remote sensing applications (Behmann et al., 2015; Pasolli et al., 2012). It transforms a nonlinear regression problem into a linear regression problem with the help of kernel functions by mapping the original feature space into a new feature space. In this study, the radial basis function (RBF) kernel was used and is regarded as a better kernel function compared to linear and polynomial kernels in handlining non-linearity in the input data (Chen and Hay, 2011). The model parameters ε (loss function) and error penalty factor (C) were estimated empirically. Ensemble methods such as random forest regression are also very efficiently utilized in remote sensing applications in the literature (Yang et al., 2017; Zhou et al., 2016). The random forest regression method utilizes the ensemble of many regression trees determined independently using a bootstrap data set sample. Later, the final prediction is made using majority voting (Hultquist et al., 2014). The parameters for RFR, which are the maximum number of trees and the number of samples chosen randomly at every split, were determined empirically.

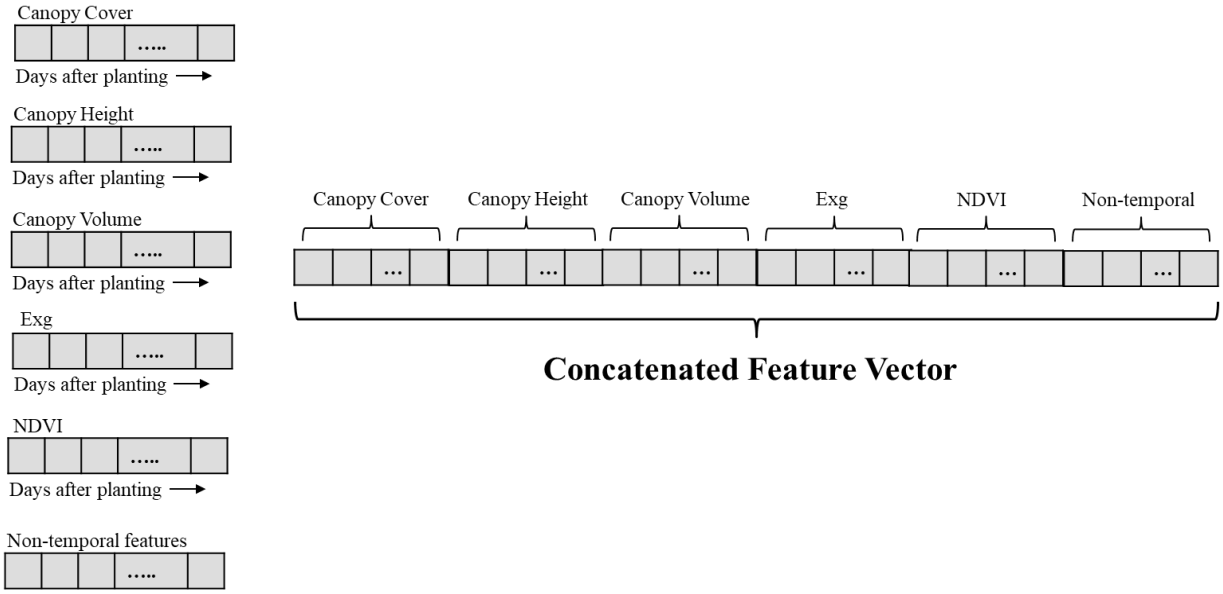

Figure 4.6. Forming a feature vector by concatenating all the attributes.

Figure 4.7 presents the network architecture consisting of three layers: an input layer, a single hidden layer, and an output layer. The temporal and non-temporal crop canopy and qualitative attributes were concatenated (Figure 4.6) and provided as input to the ANN. While training the ANN model, a concatenated input feature vector was provided to the model along with the machine harvested yield as a target feature. Initial weights were assigned randomly and later updated by employing the backpropagation algorithm using Levenberg-Marquardt optimization (Moré, 1978) to minimize the global error (mean square error). Two popular optimization functions were also tested, namely, stochastic gradient descent (SGD) (Ruder, 2016) and Adam (adaptive moment estimation) (Kingma and Ba, 2014). It was observed that the Levenberg Marquardt algorithm provided faster convergence. Levenberg Marquardt algorithm, also known as the damped least-squares method which uses gradient vector and Jacobian matrix instead of calculating the exact Hessian matrix. It combines the advantages of both Gradient-Descent and Gauss-Newton methods by decreasing the cost very efficiently for a change in its behavior, which helps achieve faster convergence for a convex function.

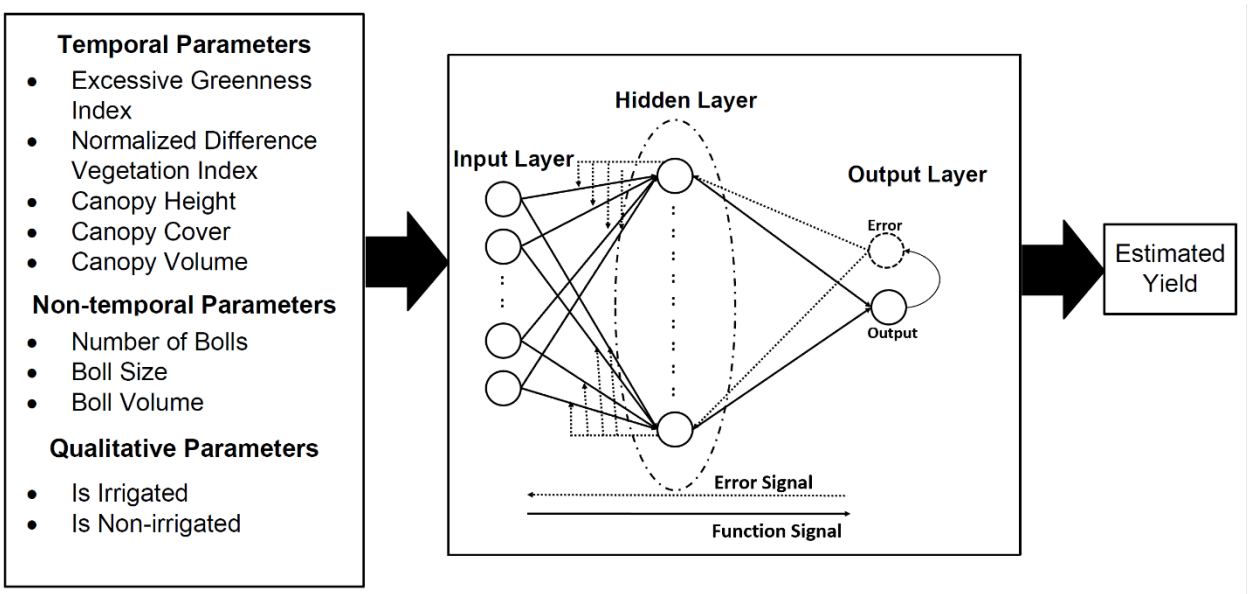

Figure 4.7. Artificial neural network (ANN) network architecture.

The training was stopped when a satisfactory level of performance, i.e., mean squared error (MSE) of the normalized yield was 10^{-3}, and the network with the current weights was used to predict the yield over the test samples. The MSE during the learning process was calculated by Equation 4.1.

$$MSE = \sum(Y_a - Y_p)^2/n \quad (4.1)$$

Where Y_a represents actual yield and Y_p represents predicted yield.

4.3.3 Sensitivity analysis

A stepwise sensitivity analysis (Gevrey et al., 2003) was performed over the input variables. This method consists of rejecting one input variable from the set and observing the effect on the prediction accuracy. When a variable has an insignificant effect on the output, the model, after removing this variable, will still show a high correlation and low MSE. After determining the optimal input variable subset, the weight method (Garson, 1991) was used to determine the percentage contribution of each variable. The weight method partitions the connecting weights of the network to determine the relative significance of the input variables. This method partitions

the hidden-output connection weights of each hidden neuron into components associated with each input neuron (Gevrey et al., 2003) as follows:

a. For *m*: 1 to *n*

For *i*: 1 to *k*

$$\theta_{im} = \frac{|w_{im}|}{\sum_{i=1}^{k}|w_{im}|}$$

end,

end.

b. For *i*: 1 to *k*

$$RS_i = \frac{\sum_{m=1}^{n}\theta_{im}}{\sum_{m=1}^{n}\sum_{i=1}^{k}\theta_{im}} \times 100$$

end.

Where *k* and *n* are the number of input and hidden neurons and RS_i is the relative significance of the i^{th} input variable.

4.4 Results and discussion

4.4.1 Canopy attribute preprocessing

Daily estimates of canopy attributes and vegetation indices were interpolated from UAS derived data using RBFNN. The estimated daily measurements address some of the variability found in UAS derived measurements (Figure 4.8), which are often caused by noise, flight, and weather conditions. Because UAS data may not have the same number of flights during the growing season and planting date might not be the same across multiple years, estimating daily measurement and converting the Julian date to day-after-planting also enables multi-year analysis.

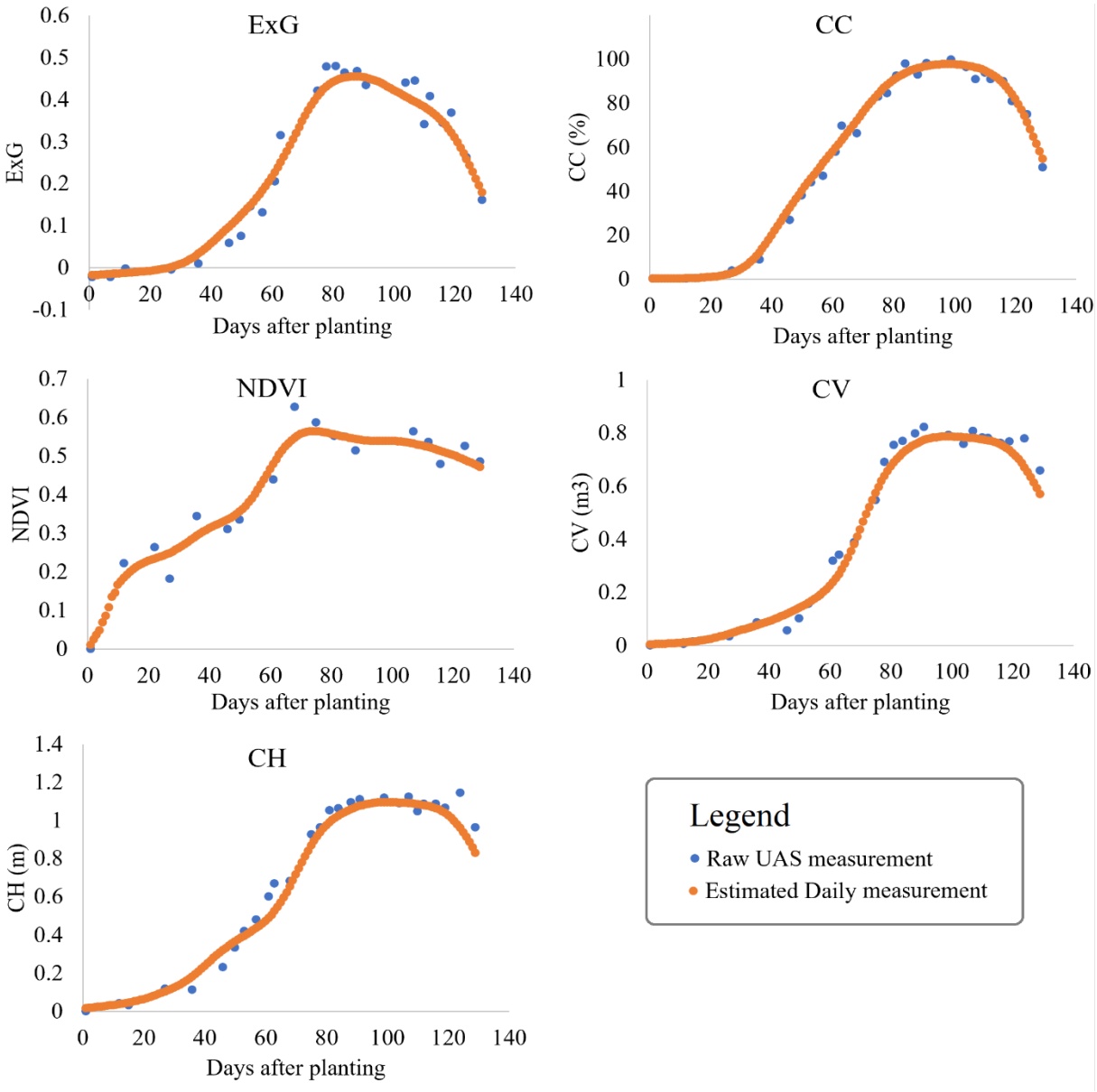

Figure 4.8. An example of daily interpolation of canopy attributes: canopy height (CH), canopy cover (CC), canopy volume (CV), excess greenness index (ExG), and normalized difference vegetation index (NDVI) from unmanned aircraft system (UAS) based measurements using radial basis function neural network (RBFNN) for one plot.

Table 4.3, a total of 25 flights were conducted throughout the growing season. However, in light of the practical constraints associated with a large number of UAS data collection, initial experiments were conducted to determine the optimum number of flights needed to determine daily measurements accurately. Daily measurement estimates were computed based on uniform intervals and based on crop physiology (Figure 4.9). A part of the available data was used for deriving the interpolation model, and the remaining data were used for the evaluation of the same. The uniform interval-based method involved experiments with UAS data considered roughly on a weekly basis, at two-week intervals, and at three-week intervals. The crop physiology-based method considered UAS datapoints that represent the shape of the crop growth curve. The lowest average RMSE was obtained with daily interpolation using measurements at the one-week interval (Table 4.4). However, the difference between the average RMSEs of one-week and three-week intervals was only 0.5 cm. Crop physiology-based time interval resulted in an average RMSE of 6.4 cm. Although the crop physiology-based method resulted in the highest RMSE amongst all cases, the difference between the lowest and the highest RMSEs was only 0.8 cm which is even less than one percent of the average height of a fully grown cotton plant. Similar results were observed for other canopy attributes also.

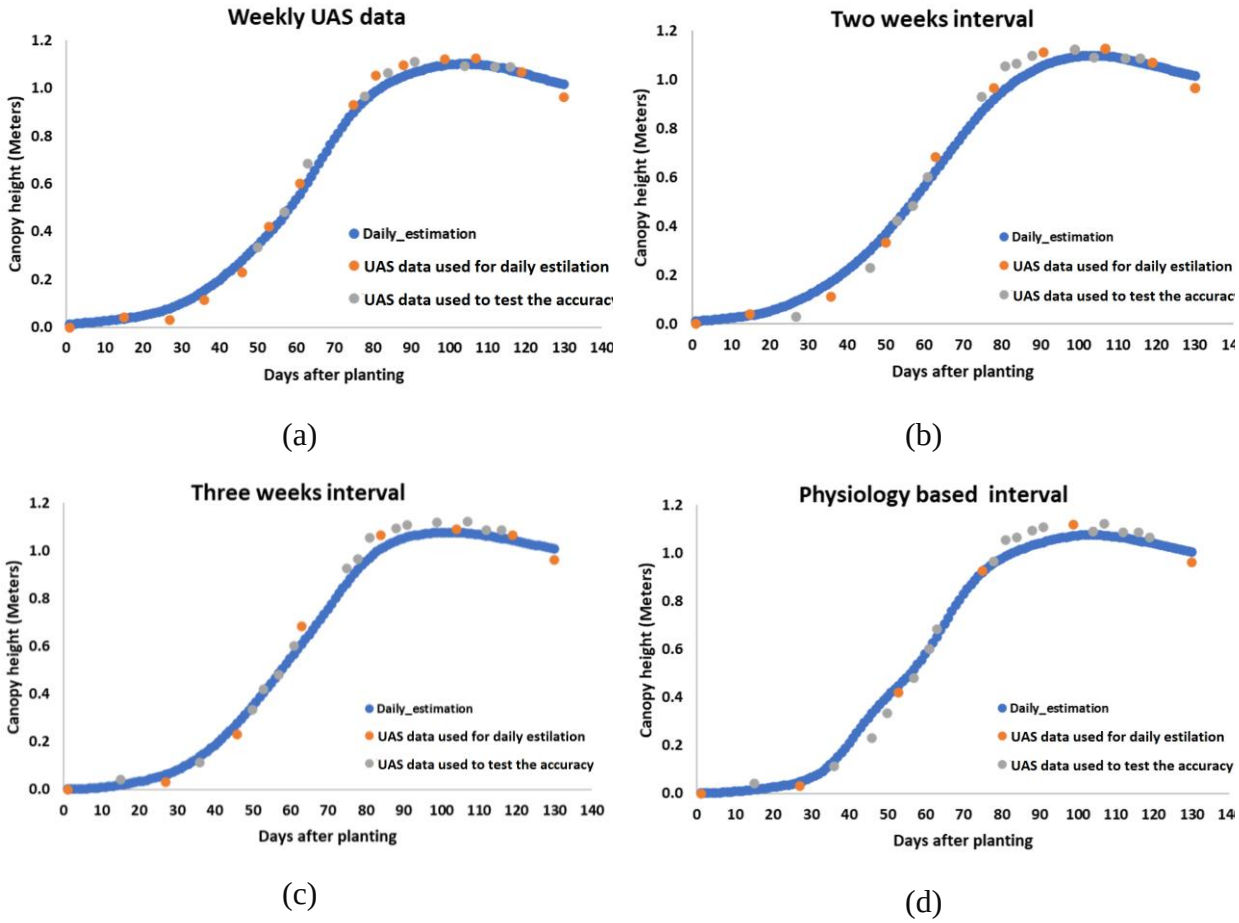

Figure 4.9. Daily measurement estimation of UAS based canopy height using a part of the available data for deriving the interpolation model and the remaining data for the evaluation. Two methods were considered for the experiments, based on (a) to (c) uniform intervals of one, two, and three weeks, respectively, and (d) crop physiology.

Table 4.4. Accuracy assessment of daily measurement estimation for UAS based canopy height based on uniform interval and crop physiology.

Method	Average RMSE over test data (cm)	No samples utilized for daily interpolation
Weekly	5.6	14
Two weeks interval	5.8	9
Three weeks interval	6.1	7
Physiology based interval	6.4	5

Weekly measurements were extracted from estimated daily measurements and concatenated to form a feature vector to be used as input to machine learning models. To reduce the input feature vector size, an analysis was performed categorically to examine the degree of correlation between the canopy attributes, vegetation indices, and open cotton boll attributes. For temporal variables, the average of all the correlation coefficients of individual temporal instances was considered. A strong correlation was found between the vegetation indices NDVI and ExG with a correlation coefficient of 0.97 (Table 4.5). In this case, ExG was chosen to be included in the reduced input feature set since it potentially eliminates the need for multispectral sensor data.

Table 4.5. Correlation coefficient matrix for vegetation indices.

Attribute	NDVI	ExG
NDVI	-	0.97
ExG	0.97	-

Table 4.6. Correlation coefficient matrix for canopy attributes.

Attribute	CH	CC	CV
CH	-	0.97	0.99
CC	0.97	-	0.98
CV	0.99	0.98	-

Table 4.7. Correlation coefficient matrix for open cotton boll attributes.

Attribute	BC	BS	BV
BC	-	0.77	0.81
BS	0.77	-	0.97
BV	0.81	0.97	-

The correlation coefficient matrix for canopy attributes (Table 4.6) indicated a strong correlation between CH, CC, CV, implying that only one canopy attribute may be sufficient as part of the reduced input feature set. CV was selected for the model among the canopy attributes since it inherently incorporates CH and CC (Equation A.3). The results for the open cotton boll attributes suggested a high degree of correlation between BS and BV (Table 4.7), so BV was chosen to be included in the reduced input feature set. The reduced input feature set included CV, ExG, BC, BV, and Irrigation status (IR). In some cases, plots contained patches of non-target plants, such as weeds (Figure 4.10), which may erroneously lead to over estimation of the crop yield because of comparable values of canopy attribute and vegetation indices contained in these patches. Therefore, plots containing excessive non-target plants were manually removed from the analysis after a careful visual inspection of RGB images. However, there were only less than one percent of samples removed based on weed infestation.

Figure 4.10. Example of excessive non-target plants in the plots indicated by the red boundaries.

4.4.2 Regression model implementation

The training was performed over 644 samples (80%) using the k-fold cross-validation method. An empirical evaluation to determine ANN hyperparameters was performed using the grid search method. The network performance was evaluated over the k-fold training and validation sets, and a test set using the coefficient of determination and RMSE. Selected hyperparameters are presented in Table 4.8. A stratified sampling method was used to select the samples for training and testing to ensure that the ANN was trained and tested over a wide range of yield values. Training error decreased over successive training epochs, reaching convergence after the 4th epoch (Figure 4.11).

Table 4.8. Parameter selection of artificial neural network (ANN) model.

Parameter	**Value**
Number of hidden layers	1
Hidden layer neurons	10
Training Method	Levenberg-Marquardt
Activation function	Hyperbolic tangent sigmoid
Training and Test ratio	80:20

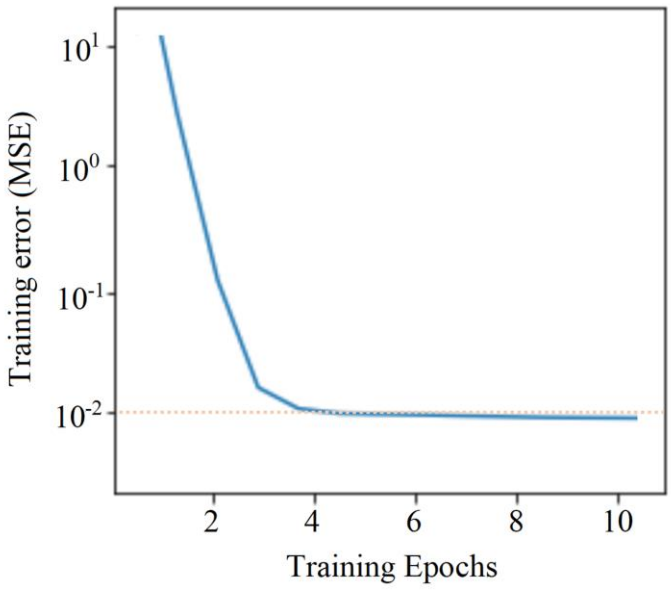

Figure 4.11. Performance of the network for training for one of the instances of k-fold where the x-axis represents iterations, and the y-axis represents training mean square error (MSE).

The error histogram over the test set is presented in Figure 4.12, which indicated that residuals were centered around zero. Additionally, the Shapiro-Wilk normality test (Yap and Sim, 2011) indicated that the residuals follow a normal distribution with zero mean and a standard deviation of 0.06. Since the errors were normally distributed with zero means, the probability of the model having significantly large errors was very less. The observed and estimated values revealed a high correlation between actual and predicted yield values (Table 4.9), except for a few outliers.

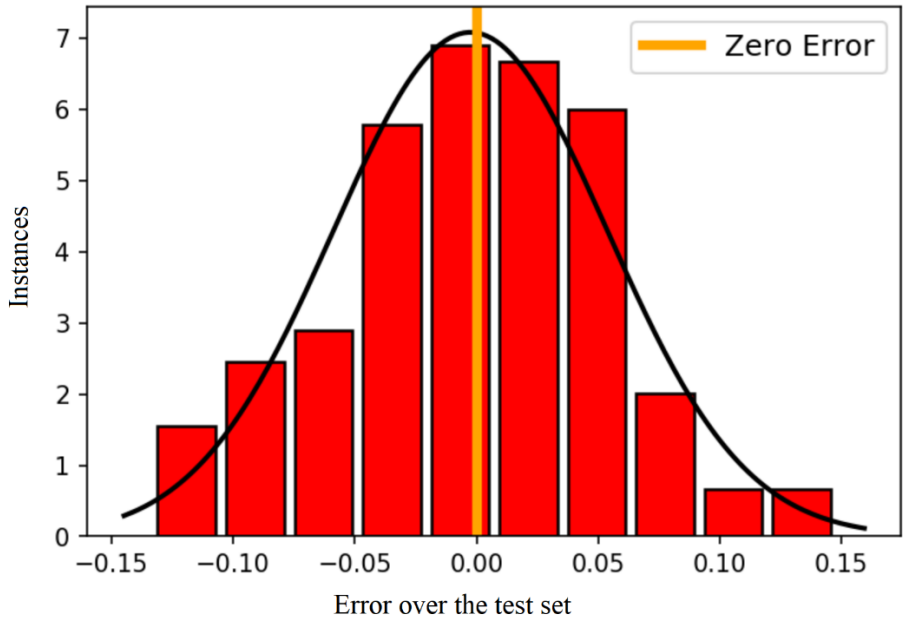

Figure 4.12. Error histogram of the residual between predicted and actual yield (normalized).

Performance assessment of the model included the average coefficient of determination and RMSE for 10-folds (Table 4.9). The observed and estimated values are depicted in Figure 4.13 for one of the 10-fold results, which revealed a one-to-one correspondence among the actual and predicted yield values confirming the high performance of the ANN model. The average of 10-folds results indicated a high test-time performance of ANN with a coefficient of determination of 0.86 and RMSE of 0.64 lb for an average of 10-folds.

Table 4.9. Model performance assessment. The best-case scenario and an average of ten runs are shown.

Estimators	Average of 10-folds
R^2 value for training	0.92
R^2 value for validation	0.85
R^2 value for testing	0.86
RMSE for training (lb)	0.30
RMSE for validation (lb)	0.71
RMSE for testing (lb)	0.64

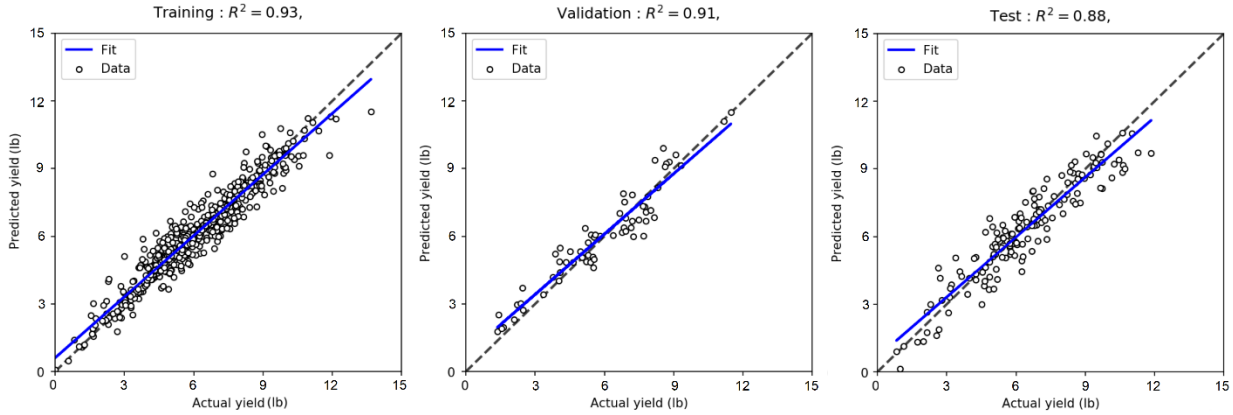

Figure 4.13. Correlation between actual and target yield for training (left), validation (middle), and testing (right) of an artificial neural network (ANN).

4.4.3 ANN model comparison with SVR and RFR

Empirically determined parameter values of SVR and RFR are presented in Table 4.10. The performance of the ANN model was compared with two widely used machine learning regression models, namely, SVR and RFR. The performance analysis based on the coefficient of determination and RMSE revealed that all three methods successfully captured the complex relationships between UAS derived canopy attributes and the yield (Table 4.11). Particularly, the performance of RFR and SVR exhibited considerable similarity, and ANN outperformed RFR and SVM marginally. However, it cannot be inferred from this study that ANN is superior to SVM and RFR for yield estimation since this research included only a single case study. The objective of

this research was not to identify the best performing machine learning model for yield estimation but to determine the useful features which can serve as inputs to the yield prediction model.

Table 4.10. Parameter setting for support vector regression (SVR) and random forest regression (RFR).

Regression method	Parameters	Values
SVR	ε, C	0.005, 10
RFR	n_$estimator$, max_$depth$	50, 7

Table 4.11. Model performances comparison between artificial neural network (ANN), support vector regression (SVR), and random forest regression (RFR) regression methods using a coefficient of determination and RMSE over the training and test cases in best-case and average of 10-fold cross-validation.

Method	Average of 10-fold Training		Validation		Testing	
	$R^2 \pm \sigma$	RMSE ± σ (lb)	$R^2 \pm \sigma$	RMSE ± σ (lb)	$R^2 \pm \sigma$	RMSE ± σ (lb)
ANN	0.93 ± 0.01	0.26 ± 0.08	0.85 ± 0.02	0.71 ± 0.16	0.87 ± 0.03	0.63 ± 0.14
SVR	0.89 ± 0.02	0.31 ± 0.11	0.84 ± 0.02	0.98 ± 0.35	0.84 ± 0.01	1.01 ± 0.38
RFR	0.91 ± 0.02	0.28 ± 0.09	0.84 ± 0.02	0.95 ± 0.31	0.84 ± 0.02	0.92 ± 0.27

When it comes to machine learning models, their suitability is context-dependent. The effective utilization of a regression model, coupled with a feature extraction methodology to devise a machine learning framework has been intensively discussed in the previous literature. SVR and RFR have demonstrated their capability to handle challenging cases pertaining to remote sensing data for classification and regression problems, such as the high-dimensionality of the input data, the scarcity of training examples, and data heterogeneity (Hengl et al., 2018; Sheykhmousa et al., 2020). However, SVR does not perform well when the number of the training sample is large (Awad and Khanna, 2015). RFR works well with a mixture of numerical and categorical features. However, a large number of decision trees required to be generated can make the algorithm too slow and ineffective for real-time predictions (İskenderoğlu et al., 2020). A typical ANN can be

defined as a parallel computing system comprising of a large number of simple interconnected processors (Raczko and Zagajewski, 2017). ANNs are inherently capable of deciphering complex nonlinear relationships between independent and dependent variables. The hidden layers of ANN enable it to determine the interactions or interrelationships between the input variables (Tu, 1996).

It is common knowledge that yield is the function of a range of temporal, non-temporal, and categorical variables, as discussed in section 4.4.1. There are deep neural network architectures that explicitly take care of temporal dependencies; however, they require a large number of training samples (Le and Zuidema, 2016; Sun et al., 2019). Consequently, an ANN with a single hidden layer was chosen for this study. For the problems where there is a lack of adequate understanding pertaining to the optimum combination of various inputs, a reasonable strategy is to assume that every variable can affect the final output. Subsequently, the use of sensitivity analysis facilitates the estimation of the proportional contribution of each input variable. Additionally, mixing different types of variables together in an input vector runs the risk of losing the meaning of variables. For example, when two instances of the same temporal variable are mixed together, the information that they are of the same variable is lost. So, mixing static and temporal variables together creates additional ambiguity. Unlike the normalization for each vector dimension separately where the temporal dependencies are lost, the group normalization used in this research preserved crucial information like temporal order. Additionally, the intention of including one categorical variable was to classify the input features into two categories irrigated and non-irrigated.

4.4.4 Sensitivity analysis

In the stepwise sensitivity analysis, variables were eliminated one at a time. The ANN model was run ten times, and average values for the correlation coefficient and RMSE were computed (Table 4.12). A one-tailed test hypothesis was designed to examine whether removing any variable reduced the average R^2 significantly over the test set. The hypothesis used the Z statistic with a 95% confidence interval being significant when $Z > 1.645$.

Table 4.12. Stepwise sensitivity analysis report results for ten runs for optimal input variables subset. One variable was removed at a time, and average R^2, average mean square error (MSE), and Z statistics are shown.

Eliminated Variable	Test R^2 (Average of 10-fold)	Test RMSE (lb) (Average of 10-fold)	Z (95%)
CV	0.83	1.12	**2.44**
ExG	0.83	1.08	**1.92**
BC	0.84	1.00	**2.15**
BV	0.85	0.94	**1.64**
Irrigation status	0.84	1.04	**1.88**

The stepwise sensitivity analysis suggested that removing any variable from the optimum input variable set significantly reduced R^2 for the test set. With the optimal input variable set, the model input vector size was reduced from 75 to 32. Further, the weights method was applied to investigate the contribution of each input variable using the optimal input variable subset, and it was compared with the impurity-based method using RFR (Figure 4.14).

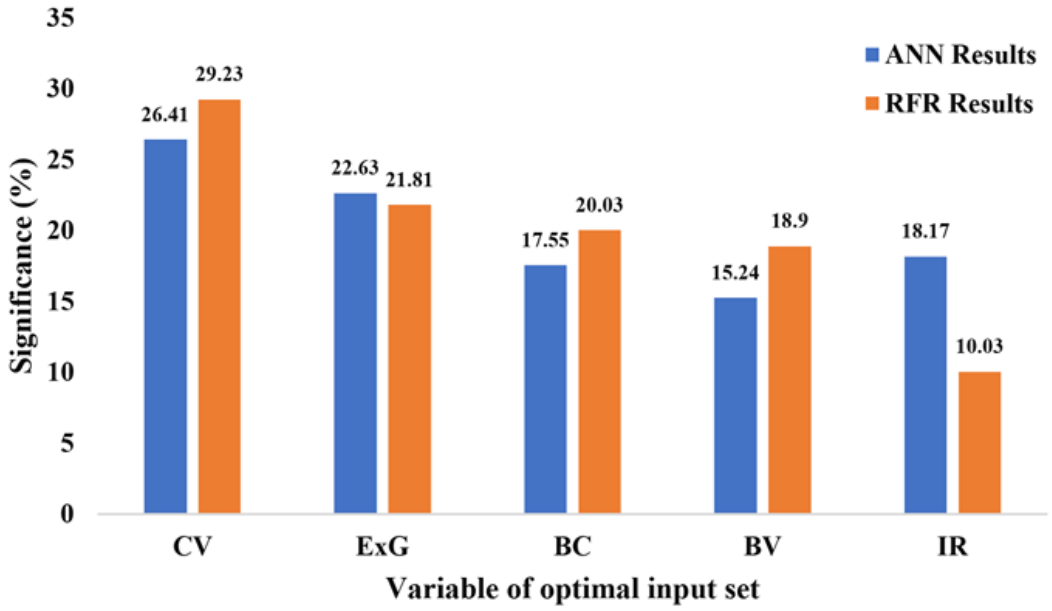

Figure 4.14 Relative contributions (%) of each variable in the optimal input variable subset using weight method for artificial neural network (ANN) and impurity-based method for random forest regression (RFR).

The weights method classified the variables according to their contribution to the model output. Canopy volume had the highest contribution (26.41%) followed by ExG (22.63%), IR (18.17%), BC (17.55%) and BV (152.4%). Combined CV and ExG contributed close to 50% to the yield estimation. Naturally, these canopy attributes are essential components of the mass and energy balance of the crop, and understanding the balance between photosynthesis and water use is key to understanding crop growth and yield (Weiss et al., 2004). Similar to the weight method, the impurity-based method also indicated the major contribution of CV. However, the relative difference between the highest and lowest contributors was higher (19.2%) in RFR as compared to the weight method (11.17%) in ANN, indicating that RFR was more biased to the highest contributor (CV). Additionally, the least importance was granted to the qualitative attributes (IR) in RFR based yield prediction.

4.4.5 Early-stage yield prediction

An analysis was performed to investigate how early in the growing season the model could predict yield with $R^2 > 0.7$ using the test set. Beginning from 100 days after planting (DAP), the model was trained and tested with a decreasing number of DAP using a step size of five days (presented in Table 4.13). Since BC and BV are end-of-the-season measurements, they were excluded from the analysis. The input variables considered were CV, ExG, and the Irrigation status.

Table 4.13. Average R^2 and mean square error (MSE) for training and test sets, including canopy volume(CV), Excess Greenness Index (ExG), and Irrigation Status (IR), over ten runs with decreasing days after planting with a step size of 5 days.

Days after planting	Training R^2 (Average of 10-fold)	Training RMSE (lb) (Average of 10-fold)	Validation R^2 (Average of 10-fold)	Validation RMSE (lb) (Average of 10-fold)	Test R^2 (Average of 10-fold)	Test RMSE (lb) (Average of 10-fold)
100	0.90	0.53	0.83	1.09	0.84	1.07
95	0.90	0.61	0.84	1.11	0.83	1.16
90	0.90	0.69	0.83	1.13	0.83	1.14
85	0.87	0.96	0.78	1.23	0.79	1.21
80	0.84	0.99	0.75	1.28	0.76	1.21
75	0.83	1.01	0.75	1.26	0.75	1.24
70	0.82	1.13	0.72	1.28	0.73	1.25
65	0.79	1.35	0.70	1.56	0.69	1.53
60	0.75	1.53	0.66	2.33	0.66	2.30
55	0.69	1.70	0.61	2.41	0.59	2.48

The growth curve of a cotton plant follows a typical sigmoid curve which has a slow growth rate in the initial phase, succeeded by an exponential growth rate for leaf area, canopy, flowering, and boll development, followed by a slow growth rate in the maturation phase. It was observed that the reduction in the accuracy with decreasing DAP commensurate well with the growth curve (Figure 4.4) suggested by crop physiology. As the plant still remains in the maturation state, there was no significant reduction in the model's performance from 100 to 90 DAP, but a high rate of reduction in the R^2 values was observed after 85 DAP, representing the tail end of the exponential growth phase of the crop. At 70 DAP, the model predicted the yield with a test R^2 greater than 0.7, indicating the potential use of this methodology as early as 70 DAP to estimate crop yield. The test accuracy declined significantly below 70 DAP as the plants grew exponentially at this period, and any small change in DAP will significantly impact test accuracy.

This study explored the feasibility of incorporating UAS derived features to predict yield using an artificial neural network model. The study demonstrates how multi-temporal, non-temporal, and qualitative features can be incorporated into a single feature vector as an input to the ANN model to estimate cotton yield. The initial implementation included all the features and showed accurate yield prediction results with a low RMSE. Performance comparison revealed that,

although the ANN model achieved a higher R^2 for the test set compared to SVR and RFR, all the three models were able to predict the yield with acceptable accuracy (R^2 higher than 0.82 on average of 10 runs and higher than 0.85 for best case scenario). If there are some inherent learnable patterns in the training set, any machine learning model that can handle non-linearity in the data can perform reasonably with appropriate parameter tuning. Thus, preparing the training set that comprises the appropriate input features having learnable patterns pertaining to the target is more critical compared to the choice of a regression model (Halevy et al., 2009; Sun et al., 2017). However, the ANN performed better in a multi-modality scenario where the input variable set comprised three different types of features: multi-temporal, non-temporal, and qualitative features. Sensitivity analysis using a stepwise elimination of the input variables suggested some redundancy in the initial input variable set, except for boll count and irrigation status. Except for these two variables, removing any other variables from the set did not significantly change the accuracy of the prediction. A correlation analysis was used to eliminate the redundant variables resulting in a reduced subset of the input variables. For this research, plant canopy attributes and vegetation indices computed using RGB sensor data were adequate for accurate cotton yield prediction. This may be used in the future to reduce overall experimental costs and data collection time. Moreover, RGB sensors are robust and less expensive when compared to multispectral sensors (Andújar et al., 2016; Nock et al., 2013; Paulus et al., 2014).

An additional stepwise elimination analysis suggested that the reduced input variable set was the optimal subset as removing any of these inputs affected the prediction accuracy of the network. With the optimal subset of input variables, the network training time was reduced by more than 50%, as the original input vector size was 75, and reduction resulted in a vector size of 32. Quantifying the significance of individual input variables in the ANN model is very important to open the ‘‘black box” model and provide information about the role of each variable in the model. In agriculture, finding the variables contributing to crop yield is important as it helps farmers and agriculture scientists reduce environmental impact while increasing agricultural sustainability (Khoshroo et al., 2018). A sensitivity analysis was carried out using the weights method to determine the input variables with the most impact on yield. Results indicated that

canopy volume had the most significant impact on cotton yield, followed by the excessive greenness index. The difference between the relative contribution of the most important and the least important variable was 12%.

This study also explored how early in the growing season yield can be reasonably predicted. The input variable set excluded boll count and boll volume as the open cotton bolls are only visible at harvest. Canopy volume, ExG, and the irrigation status were used to predict the yield and tested by gradually reducing DAP. The prediction accuracy decreased as the DAP decreased. An inspection of the rate of decay in the prediction accuracy revealed that it was commensurate with the growth pattern of the canopy attributes used as input variables (Figure 4.8 CV and ExG). For the DAP greater than 70, canopy attributes were close to attaining a plateau, and there was no significant change in the attribute values with an increase in DAP. However, between 50 to 70 DAP, the crop growth pattern resembles a steep slope (i.e., linear phase of plant growth as presented in Figure 4.8). The ANN model predicted cotton yield with an R^2 greater than 0.7 as early as 70 DAP. Although many factors, such as biotic and abiotic stresses, may affect the crop growth between the end of remote-sensing measurements and harvest, an early-stage yield prediction can help farmers and agriculture scientists make crop management and marketing decisions based on the predicted yield potential. Breeding trials generally contain thousands of plots, and breeders could benefit from a high prediction accuracy model that would assist them in selecting suitable genotypes without the need to harvest each plot to determine yield, reducing overall program costs. Increased screening efficiency will allow them to explore a larger number of genotypes.

The results demonstrate that UAS technology can be used as high precision and cost-effective system to extract canopy attributes throughout the growing season for yield prediction. Collecting high-quality UAS data is critical for the computation of crop canopy attributes and VIs, which can be significantly affected by UAS's flying altitude, forward and side overlaps, spatial resolution, and the entirety of the DTM obtained using the SfM pipeline. Additionally, weather conditions play an important role in UAS data collection and should be considered since they affect the quality of data products (e.g., orthomosaics and DEMs), which in turn affects the quality of the

extracted plant canopy attributes. Additionally, the quality of sensors also determines the quality of the vegetation indices computed. A Tetracam ADC snap sensor without a sunlight sensor was used in this study for multispectral data collection, which questions the reliability of the data. However, NDVI maps were mostly consistent as the data were collected during the same time of the day throughout the growing season. Additionally, the sensor used for multispectral data was the same throughout the data collection. Moreover, the reliability of the multispectral data was not a primary concern of the present study, as it was demonstrated that the optimal feature subset for the yield prediction model did not utilize any feature derived from multispectral data.

4.5 Conclusion and future work

The ability to combine temporal, non-temporal, and qualitative features to predict crop yield is very powerful. In this study, an Artificial Neural Network (ANN) machine learning model was developed to predict cotton yield by leveraging high-resolution UAS imagery to derive biologically relevant plant canopy attributes. The proposed model predicted cotton yield with an R^2 value of 0.89 in the best-case scenario and an R^2 of 0.85 in an average of ten runs. Redundant input variables were eliminated by sensitivity analysis, and an optimal subset of input variables was obtained. Plant canopy attributes were derived from RGB data, reducing the overhead of collecting multispectral data. Moreover, the ANN training time was reduced by more than 50%, with no significant reduction in the prediction accuracy. Findings from this study can serve as a valuable tool for cotton breeding research programs. If breeders can incorporate the technology, there is potential to increase genotype selection efficiency. With this technology, agricultural scientists and crop managers, crop consultants, and farmers can have access to a level of information about the crop that was not previously available, helping in the decision-making process. Finally, with an accurate early-stage yield prediction, appropriate crop management decisions can be taken to improve the efficiency and sustainability of farming operations.

This study's crop yield estimation was limited to the upper and lower limit of the available yield values with no extrapolation beyond the data limits. Moreover, the geographical location was also a constraint, as the experiments were limited to a single study site for a single year. In the

future, the inclusion of other geographic locations and multi-year data would allow transfer learning of the methodology to test the feasibility of the current model across geographic locations and time. Additionally, multi-location experiments may demand additional analysis to include more input features such as soil type, weather information. This study focused on cotton crop yield estimation. Transferability of this methodology was successfully demonstrated for other crops, such as corn and tomato (Ashapure et al., 2019c) after replacing attributes specific to the cotton crop such as boll count, boll size, and boll volume with the crop attributes specific to tomatoes and corn. In the future, similar experiments can be performed to test the efficacy of the methodology for other crops. Moreover, sensitivity analysis would result in a different subset of input features suggesting the significance of each feature for the crop yield. Generally, recurrent neural networks (RNNs) are found to be suitable for temporal data (Lipton et al., 2015; Ndikumana et al., 2018). However, RNNs alone are not capable of handling the multi-modality nature of the input data involved in this research, which includes multi- and non-temporal data along with qualitative data. Moreover, RNNs suffer from the vanishing gradient issue when handling a large sequence of data (Le and Zuidema, 2016). Usually, RNNs are combined with CNN and other deep networks, and the hybrid model is used for prediction (Khaki et al., 2020). However, it requires enormous training data, making them unsuitable for applications involving limited training samples. In the future, the availability of multi-year data would provide scope for validating the methodology along with multi-year predictions, and the availability of more data would also allow for experiments involving more sophisticated machine learning models, including deep learning models.

Overall, this study successfully demonstrated a yield prediction methodology by proposing a machine learning framework that exploits UAS derived crop canopy attributes. An accurate prediction of cotton yield and replacing human labor with automated high throughput phenotyping will help agricultural research. It will also help towards informed crop management decisions based on yield prediction, especially when the breeding trials contain thousands of plots.

5. LEVERAGING DEEP LEARNING TO IMPROVE SATELLITE DATA BASED CROP YIELD ESTIMATION USING UAS DATA AS SIDE INFORMATION

5.1 Background

A recent upsurge in the development of UAS largely contributed to the implementation of HTP for precision agriculture applications (Singh and Frazier, 2018). With high temporal and spatial resolution data, UAS is being utilized successfully to detect crop biomass and yield (Swain et al., 2010) and monitor crop growth (Ashapure et al., 2019b) with a great degree of precision. These applications have resulted in the reliable and efficient estimation of crop canopy phenotypes and vegetation indices (Calders et al., 2015; Chianucci et al., 2016; Harwin and Lucieer, 2012; Pádua et al., 2017). Later, these attributes are also utilized for yield estimation (Gandhi et al., 2016; Gopal and Bhargavi, 2019). One of the main advantages of UAS derived phenotypic data is that they are reliable and can provide more precise phenotypic measurements than manual observations in the field. Further, it covers the whole area seamlessly so that a huge number of training data can be generated from the UAS data. These large number of training samples can be utilized to develop state-of-the-art deep learning models for accurate yield prediction (Khaki et al., 2020; Tri et al., 2017). Although UAS is capable of providing high spatial and temporal resolution data, large aerial coverage is not feasible due to limitations, such as payload, flight time, and large size of the data.

Besides UAS based HTP, satellite data is also extensively utilized for precision agriculture applications (Rudd et al., 2017; Yang, 2018; Yang et al., 2012). They cover a larger area but provide coarser spatial resolution data compared to UAS imagery. Additionally, weather conditions are often a huge concern for passive sensors. UAS is relatively less affected by weather conditions; furthermore, UAS provides more spatial and temporal resolution flexibility compared to satellite data (Xiang and Tian, 2011). The present study aims to develop an effective crop yield prediction model by taking advantage of the UAS's ability to provide precise fine spatial resolution data with the vast spatial coverage provided by satellite data.

5.1.1 Scope and contribution

In chapter 4, it was well established that multi-temporal UAS data can be successfully employed for crop yield estimation. However, the scale of the experiment was limited by the aerial coverage of the UAS. On the contrary, satellite remote sensing data are widely utilized for crop yield estimation over a large area (Ferencz et al., 2004; Hunt et al., 2019; Meng et al., 2019; Novelli et al., 2019; Sayago and Bocco, 2018; Singh et al., 2002), although coarser spatial resolution is still a concern for many precision agriculture applications. Current state-of-the-art crop yield prediction using multi-temporal satellite data is valuable for extensive aerial coverage; however, their coarser spatial resolution limits the level of detail UAS could provide. There is a knowledge gap in the literature regarding combining UAS and satellite data together for crop yield estimation. It is vital to address this research gap since an accurate crop yield prediction in a larger area before harvest is essential to prevent famine, improve food security, and sustainable development of agriculture. To fill this aforementioned knowledge gap, this chapter explores ways in which UAS derived information can be provided as side information to improve satellite data-based crop yield prediction models. Previous studies (Gupta et al., 2014; Wang et al., 2015) indicate that fusion of multi-modal data significantly enhances the performance of deep learning-based detection models. However, no access to UAS data at test time is a barrier to the straightforward adoption of the traditional fusion-based approaches. To overcome this challenge, this study explores various strategies in which UAS data can be used as side information to improve the performance of satellite data-based crop yield prediction models. Two different techniques are proposed based on cross-task knowledge transfer and modality hallucination, eliminating the need for UAS data at test time. The proposed technique efficiently handles selective availability of UAS data leading to enhanced crop yield estimation accuracy.

5.2 Study area, sensors, and platforms

Field experiments were conducted in Driscoll, TX, USA (27°46’59” N, 97°34’13” W). The total area of the commercial cotton field under consideration was approximately 100 acres. A single variety of cotton was planted on March 2, 2020, and machine harvested on August 9, 2020.

Soil types in the study site are Victoria Clay series soils (Victoria-Lattas-Clareville). The temperature variation throughout the growing season varied between 79°F to 96°F with an average humidity of 76%. Average monthly rainfall in the region ranges between 50 mm and 90 mm during the growing season (NWS, 2016). Figure 5.1 shows the RGB orthomosaic of the study area captured on July 2nd, 2020. For the computation of various canopy attributes corresponding to Sentinel-2A pixel level, the entire field was divided into 10m x 10m size grids equivalent to the Sentinel pixel size.

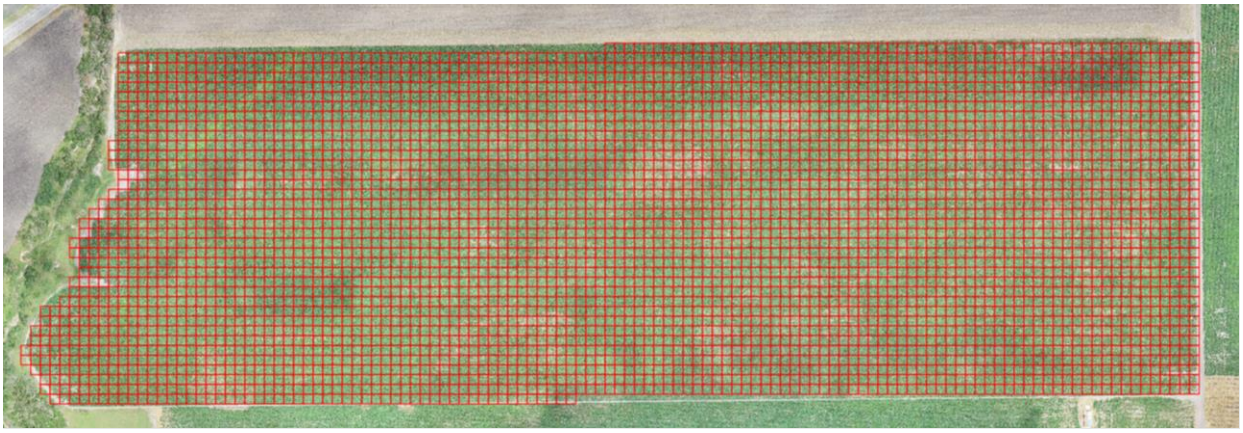

Figure 5.1. RGB orthomosaic of the study area captured on 07/02/2020 with 10m x 10m size grids overlaid on top (represented in red color).

Two types of sensors were considered in this study, namely, UAS based RGB sensor and satellite-based multispectral sensor. UAS data were collected using DJI Phantom-4 RTK (SZ DJI Technology Co., Ltd., Shenzhen, China). The weight of this UAS is 1.4 kg with a flight endurance of up to 30 minutes in mild weather conditions. Phantom-4 RTK is equipped with a 3-axis gimbal and an RGB sensor with a resolution of 20 megapixels, with an FOV of 60°. Phantom 4 RTK was accompanied by a DJI base station having a GNSS receiver and radio transmitter to send positional corrections to the UAS when the data was being collected. A permanent GCP was installed on the northeast side of the experimental field. The GCP was surveyed for more than two hours to get the precise coordinates using a dual-frequency, post-processed kinematic (PPK) GPS, model 20Hz V-Map Air (Micro Aerial Project L.L.C., Gainesville, FL). This permanent GCP with known precise coordinates was used to place the DJI base station, and radio communication was set up between

this base and the UAS. The radio communication was established and maintained throughout the data collection during each flight, which allowed real-time positioning of the UAS relative to the known base location, which in turn enabled each image to be associated with an RTK corrected three-dimensional position. After each flight, the collected raw UAS data was processed using Agisoft Photoscan Pro software (Agisoft LLC, St. Petersburg, Russia) to generate DSM and orthomosaic. Satellite data considered were Sentinel-2A which has 13 spectral bands (443–2190 nm) and a swath width of 290 km. During the growing period, five instances were found where there was a considerable match between UAS data collection and cloud-free Sentinel-2A data availability (presented in Figure 5.2 (a)). Absolute georeferencing accuracy of the UAS generated DSM and orthomosaics was not computed. However, the relative accuracy of multi-temporal UAS data was observed to be centimeter-level on visual inspection, i.e., 2 cm in planimetry and 3 cm in altimetry. Additionally, the visual inspection also confirmed that UAS data aligned adequately with satellite data.

As described in section 4.3, the ideal acquisition frequency for remote sensing data is application-dependent. It is very critical to account for the growth behavior of the crop under consideration for yield estimation. Under favorable moisture and temperature conditions, the growth of the cotton plant follows a well-defined and consistent pattern expressed in days. Ritchie et al. (2007) provided a general growth pattern of the cotton plant as presented in Figure 5.2, where the red markers represented epochs when the satellite data was available. For effective yield estimation, sample data points must be close enough to accurately represent the shape of the growth curve. Therefore, the data collection strategy should adopt a systematic targeting of critically sensitive periods as suggested by knowledge of crop physiology.

Table 5.1 presents the UAS data collection timeline and flight specifications. It is evident from Figure 5.2 that the satellite data used in this study compare favorably with the trend of the cotton growth curve.

The yield data were also available for an independent field (~400 acres) close to the main experiment field at Driscoll, Texas. Figure 5.3 (b) presents the Sentinel-2A time series data over an independent test field considered in this study where UAS data were not available. As shown

in Figure 5.3 (b), the Sentinel-2A imagery acquired on 7/10/2020 has a partial cloud coverage over the northern half of the field (~100 acres), which was not used in this experiment.

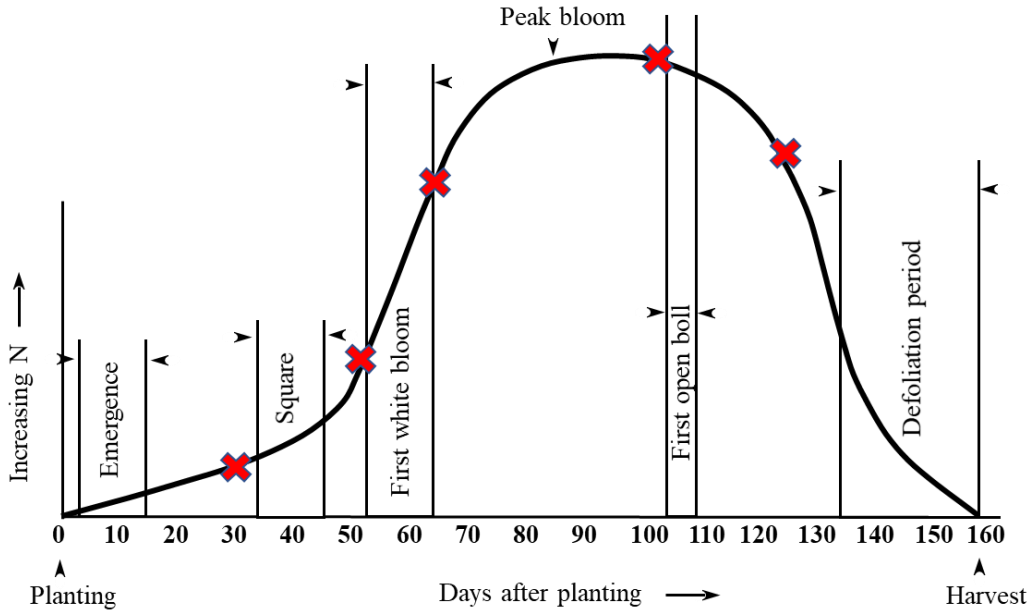

Figure 5.2. A typical growth curve of the cotton plant following a sigmoid curve, where the x-axis represents days after planting, and y-axis represent the nitrogen content in the plant (Ritchie et al., 2007). Red markers represent the days after planting when the satellite data was available.

Table 5.1. UAS data collection timeline and flight specifications.

Date	Flight Altitude (RGB)	Overlap (RGB)	Spatial Resolution, RGB (cm)
4/1/2020	90m	70%	2.47
4/26/2020	90m	70%	2.47
4/30/2020	90m	70%	2.47
6/11/2020	90m	70%	2.46
7/2/2020	90m	70%	2.47

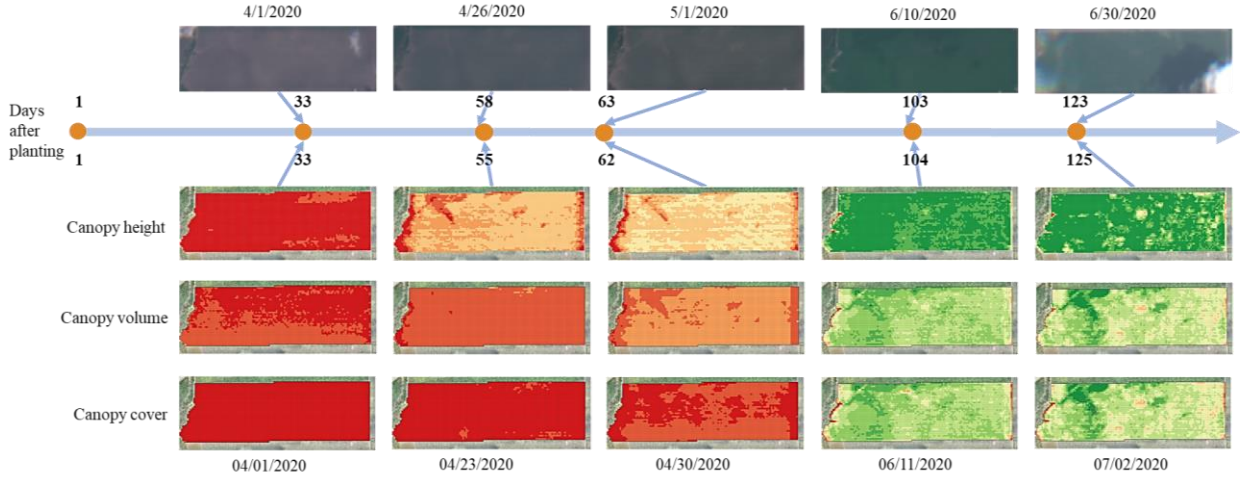

(a)

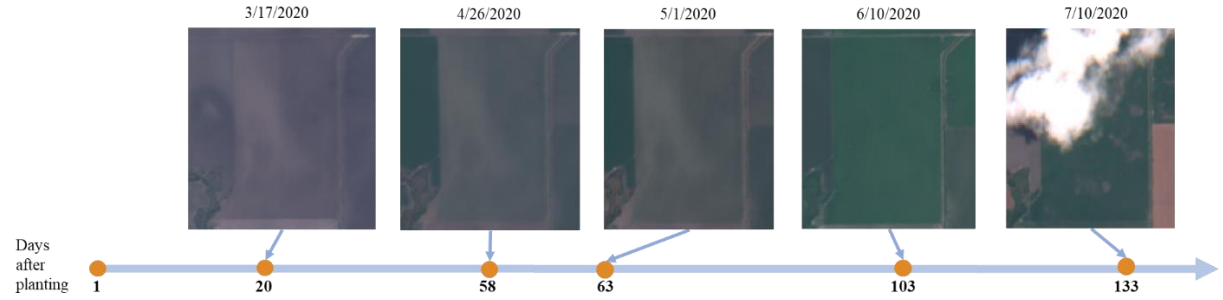

(b)

Figure 5.3 (a) Sentinel-2A time-series data (on the top) along with the corresponding matching data collected using UAS, using which canopy attribute (canopy height, canopy volume, and canopy cover) were computed grid-wise, (b) Sentinel-2A time series data over an independent test field. The orange circles on the horizontal axis depict the unevenly distributed satellite data acquisition dates over the growing season.

Table 5.2 Sentinel-2A and UAS data collection matching dates.

UAS data collection date	**Sentinel date**	**Difference (no. of days)**
4/1/2020	4/1/2020	0
4/26/2020	4/23/2020	3
4/30/2020	5/1/2020	2
6/11/2020	6/10/2020	1
7/2/2020	6/30/2020	2

5.3 Methodology

As this research aims to predict the yield over a larger area even at the locations where UAS data were not collected, UAS derived canopy attributes can only be utilized as side information at the time of training the multi-temporal satellite data-based yield prediction model. The proposed methodology demonstrated two different ways to include UAS derived canopy attributes as side information to the satellite-based crop yield prediction model: the first approach was based on cross-task knowledge transfer where UAS derived information was used as one of the outputs along with the yield, and the other approach was based on modality hallucination where the UAS derived information is used as one of the inputs to a yield estimation model along with the satellite data (block diagram of the methodology is presented in Figure 5.4).

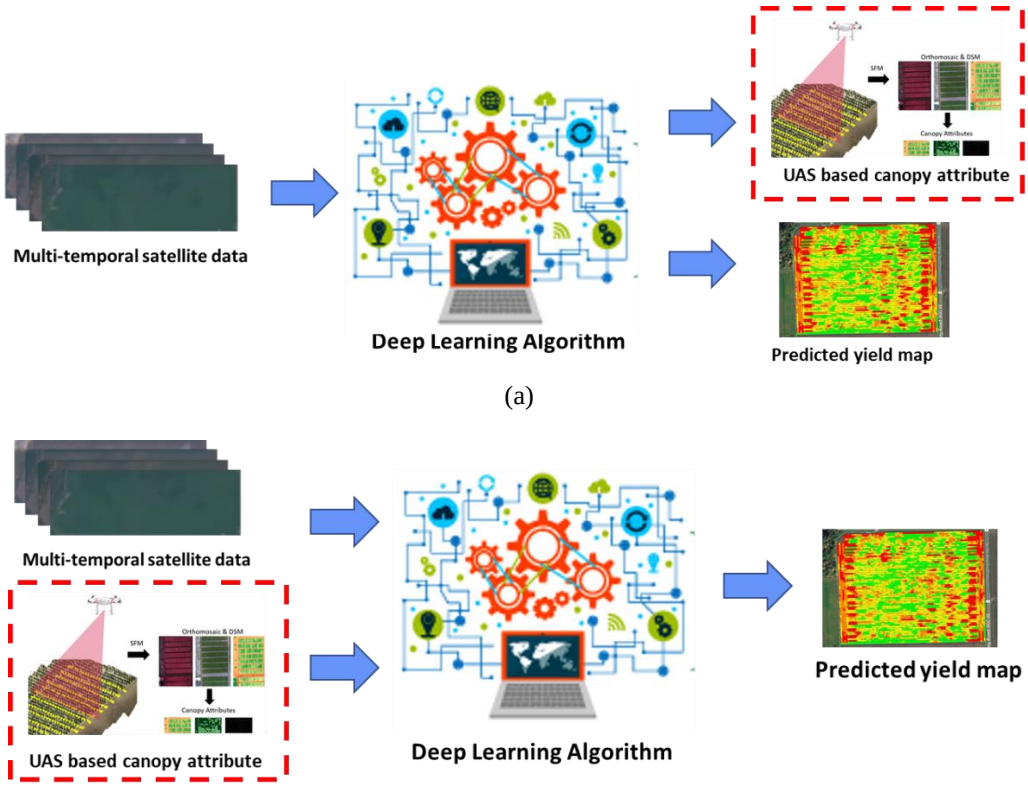

Figure 5.4. Process flow of the deep learning methodology, where UAS derived canopy attributes are used as a side information (a) as one of the outputs along with the predicted yield, or (b) as one of the inputs along with satellite data.

The overall methodology consists of two stages, including data preprocessing and machine learning modeling.

5.3.1 Data preprocessing

In this phase, UAS derived canopy attributes utilized as input to the yield prediction model were identified as canopy cover, canopy height, and canopy volume. As mentioned in section 5.2, the entire field was divided into 10m x 10m size grids, and canopy attributes were computed (canopy attribute computation is presented in section A.1 of Appendix A) and aggregated grid-wise. Yield data in the field was collected using a yield monitor equipped with a differential global positioning system (DGPS) receiver. It simultaneously records crop yield and position data, which is used to produce yield maps. The blue dots on the leftmost image in Figure 5.5 represent the locations provided by the yield monitor where the yield was measured. As these points were not uniformly distributed across the field, a spatial distribution technique was used to determine grid-wise yield from the measured harvested yield provided by the yield monitor.

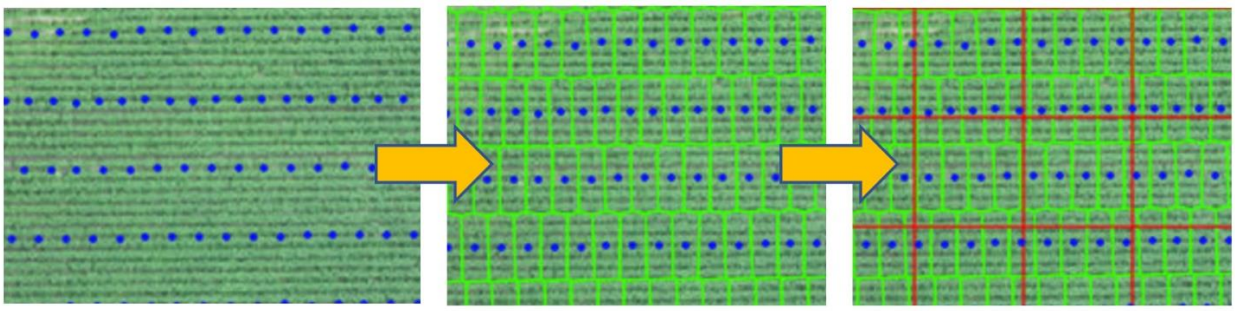

Figure 5.5. Procedure to compute grid-wise yield values using yield monitor. The left image contains the yield values provided by the yield monitor (blue dots). The Center image consists of Voronoi partitioning of the yield points (green polygons). The right image presents the overlaid grids (red polygons) over the Voronoi partitions.

A grid-wise yield computation procedure is shown in Figure 5.5. A Voronoi partition (Burrough et al., 2015) is performed using the yield measurements (the blue dots on the leftmost image in Figure 5.5) to determine the optimal spatial coverage of each yield point, which is presented as green polygons in the center image of Figure 5.5. Finally, the intersection of grids

(represented by red color polygons) and Voronoi polygons was performed to determine yield per grid by computing the areal sum of all the intersected parts of Voronoi polygons falling within a grid. Figure 5.6 shows the yield monitor data over the main experimental field and an independent test field along with the corresponding grid-wise aggregated yield data generated following the methodology presented in Figure 5.5.

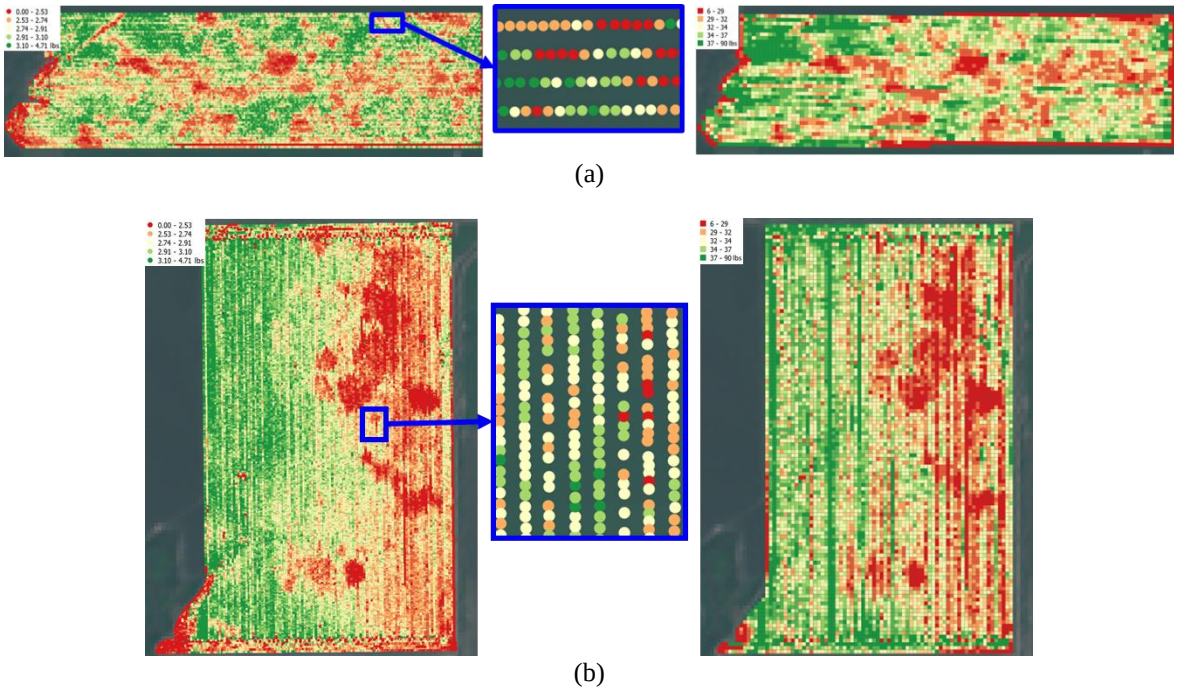

Figure 5.6. Yield data for the main experiment field (a), and independent test field (b), in Driscoll, Texas. Yield monitor data on the left, where the zoomed-in subset highlights the point measurements captured by the yield monitor. The right shows the corresponding grid-wise aggregated yield data generated following the methodology presented in Figure 5.4.

Due to a calibration issue with the weighing machine of the yield monitor, the total cotton weight reported at the ginning facility was not equal to the sum of the cotton weight recorded by the yield monitor. This difference in the total cotton weight was proportionally distributed throughout the field, assuming that the calibration issue was systematic throughout the field. Once the gird-wise information was extracted from three different sources, namely, Sentinel-2A pixel values, aggregated UAS derived canopy attributes, and aggregated yield per grid, they were

arranged in tensor forms as follows. A temporal tensor denoted Sentinel-2A pixel values of a given 10m x 10m grid in Equation 5.1:

$$X_i = \left[x_i^{(1)},\ x_i^{(2)}, \dots, x_i^{(T)}\right] \tag{5.1}$$

Where, X_i is the input feature vector corresponding to i^{th} grid on the study area. T is the total number of temporal observations throughout the growing season, and each $x_i^{(t)}\Big|_{t=1}^{T}$ corresponding to i^{th} grid represents a vector of size fourteen, thirteen of which represent band values of Sentinel-2A, and the fourteenth value represents normalized day after planting with respect to planting and harvest date. As the available satellite data is unevenly distributed in time over the period of interest, there is a necessity to have a data acquisition time indicator associated with the feature vector comprising of band values. The data acquisition time indicator ensures the training of the deep learning model with a precise sense of data acquisition timing of each temporal feature vector to provide the flexibility to accommodate the data with a different date of acquisition at the time of training and testing. UAS derived aggregated canopy attributes over a given 10m x 10m grid were denoted by a temporal tensor as follows:

$$U_i = \left[u_i^{(1)},\ u_i^{(2)}, \dots, u_i^{(T)}\right] \tag{5.2}$$

Where T is the number of temporal observations within the period of interest matching with Sentinel-2A observations, and each $u_i^{(t)}\Big|_{t=1}^{T}$ represents a vector of size three representing aggregated canopy height, total canopy volume, and percentage canopy cover corresponding to i^{th} grid. Aggregated yield corresponding to i^{th} grid is represented by a single value Y_i.

5.3.2 Machine learning modeling

The primary model used in this study to encapsulate the temporal properties of satellite data across the period of interest consists of long short-term memory (LSTM) cells, which is a special type of recurrent neural network (RNN). LSTMs are capable of modeling longer sequences as compared to simple RNN, as its cell structure provides a better gradient flow during backpropagation and prevents the model from the vanishing gradient problem (Hochreiter and

Schmidhuber, 1997). The internal memory mechanism of LSTM makes it more efficient to handle long-term dependencies. Until recently, the popularity of LSTM models was limited to natural language processing applications. However, recent years have witnessed their application in many scientific areas, including remote sensing and precision agriculture, thanks to their ability to automatically discover relevant temporal features from raw data (Masjedi, 2020; Wang et al., 2018; You et al., 2017; Zaremba et al., 2014). As mentioned earlier, LSTMs have successfully demonstrated their ability to capture relevant abstract features for biomass prediction (Masjedi et al., 2019) and large area yield estimation in conjunction with CNN (Sun et al., 2019). However, using LSTMs for high-resolution satellite-based pixel-level yield estimation is unprecedented in the literature. Moreover, utilizing multi-modality data fusion to enhance high-resolution satellite-based crop yield estimation is also not discussed.

A baseline model was developed in this research utilizing only multi-temporal satellite data as input before introducing UAS derived information as side information. As shown in Figure 5.7, the input to the network is Sentinel-2A pixel values of a given 10m x 10m grid denoted by a temporal tensor in equation 5.1.

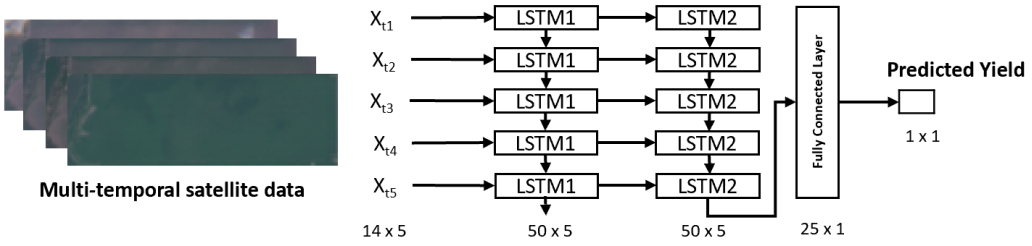

Figure 5.7. Baseline long short term memory (LSTM) based yield estimation model using multi-temporal satellite data.

An LSTM model is utilized to encapsulate the temporal properties of the input feature in the period of interest. The number of layers for the network was determined empirically with the help of systematic experiments. The input feature is first parsed through two LSTM layers which determine the temporal relationship during the crop growing season. Each LSTM layer consists of 50 nodes that use the sigmoid function as an activation function. As observed in Figure 5.7, LSTM

layers are followed by a fully connected layer of size 25. The empirical analysis determined that after two LSTM layers, a single fully connected layer was sufficient to predict crop yield. Hyperparameters considered for the baseline network are presented in Table 5.3. The objective of the baseline model implementation was to assess the potential of multi-temporal satellite data to predict the yield and provide a comparison basis for the deep architectures using UAS derived canopy attributes as side information to improve the multi-temporal satellite-based yield estimation model.

Table 5.3. Hyperparameters selection for the baseline network implementation.

Hyperparameters	**Values**
Activation function	Sigmoid
Loss function	MSE
Optimization method	Adam
Total no of samples	4130
Train and test ratio	70:30
Batch size	10
No. of epochs	100

Deep cross-task knowledge transfer architecture

This section demonstrates one of the ways how UAS derived information can be utilized as side information to improve multi-temporal satellite-based crop yield prediction. In chapter 4, it was demonstrated that UAS derived crop canopy attributes could be successfully utilized to predict the crop yield. Additionally, Sentinel-2A data has been successfully utilized to predict canopy attributes generated from UAS data (Ashapure et al., 2020b). This research aims to take advantage of the intermediate features from the deep network while using satellite data as input to predict UAS derived canopy attributes. The idea is to use those intermediate features to train the yield prediction model. This methodology stems from the main ideas of transfer learning and domain adaptation which learns to share information from one task to another.

The perception behind this methodology is that deep networks are usually capable of learning abstract representations from task 1, and part of the knowledge learned during task 1 can

be utilized further for a new task (Bengio et al., 2013). In Particular, the main principle of transfer learning is to extract certain transferable abstract representations from the source domain and transfer those abstract representations to help improve the performance on a different task in the target domain. In the literature, the transfer learning approach has been successfully utilized for crop yield prediction to utilize the pre-trained deep learning architecture from one field and use it to fine-tune over other locations (Wang et al., 2018). However, using a pre-trained network across different modalities for different target tasks is unprecedented. As shown in Figure 5.8, the cross-task knowledge transfer architecture consists of three main components: common feature transform network, UAS data network, and yield prediction network.

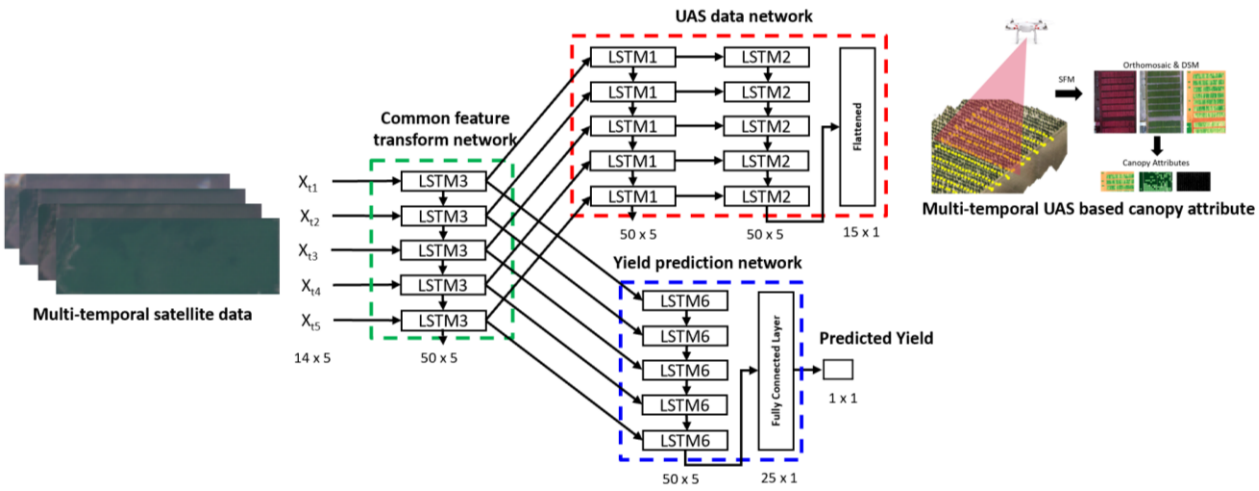

Figure 5.8. Deep cross-task knowledge transfer architecture using multi-temporal satellite data as input to predict UAS derived canopy attributes and crop yield.

The input to the network is multi-temporal Sentinel-2A pixel values, as explained in the baseline yield estimation model in Figure 5.7. Input data is provided to a common feature transform network which consists of an LSTM layer with 50 output nodes. The output of the common feature transform network is provided to both the UAS data network and yield prediction network, respectively. UAS prediction network consists of two LSTM layers with 50 and 3 output nodes, followed by a flattened layer comprising 15 nodes (three canopy attributes, namely canopy height, canopy volume, and canopy cover in five instances). The yield prediction network consists

of an LSTM layer with 50 nodes followed by a fully connected layer of size 25 and an output layer of size one in the end. The overall network is trained in a twofold training fashion. Initial training was performed combining common feature transform network and UAS data network for UAS derived canopy attribute prediction using hyper parameters present in Table 5.3. Later, the common feature transform network is combined with yield prediction network to predict the yield with an assumption that the common feature transform network is pre-trained in the initial training and will utilize that additional knowledge while training for yield prediction model in conjunction with common feature transform model. The overall design of this network provides the flexibility to selectively utilize UAS data at the time of training and transfer the knowledge to the yield prediction module. At the time of testing the yield prediction model, UAS data is not required.

Deep hallucination architecture

In recent times, heterogeneous data fusion has gained significant attention from the scientific community (Wang et al., 2015; Zhao et al., 2020). It is observed to enhance the performance of deep learning-based models significantly. However, it is sometimes difficult and expensive to access multi-modal data at the test time, which is a prerequisite for any fusion-based detection algorithm. Modality hallucination proposed by Hoffman et al. (2016) provides a viable solution to this problem by concocting scarcely available modality features from a complementary modality, the data for which are easily obtainable. This research attempts to test the feasibility of the concept in crop yield estimation using remotely sensed data. The idea was to utilize UAS derived canopy attributes as side information while training a multi-temporal satellite-based crop yield estimation model. Figure 5.10 demonstrates the training architecture for the proposed modality hallucination architecture. The model consists of mainly two channels that get input from satellite data and UAS data. These channels consist of multi-layer LSTMs to encapsulate the temporal properties of the input features. However, the goal is to combine the information coming from the two modalities and to use the training time privileged UAS data modality to update the final satellite only yield estimation. To accomplish this, a separate channel was introduced and labeled as the hallucination network (middle network in Figure 5.10 (a)). The hallucination

network takes satellite data as input and generates mid-level features similar to mid-level features of the UAS modality. An additional regression loss was introduced between the aforementioned mid-level hallucination features and corresponding UAS derived mid-level features (target). The objective of this loss function is to cause the UAS modality to share information with the satellite data modality through this hallucination network. Effectively, this loss leads the hallucination network to extract features from the satellite data which mimic the features extracted from the corresponding UAS data.

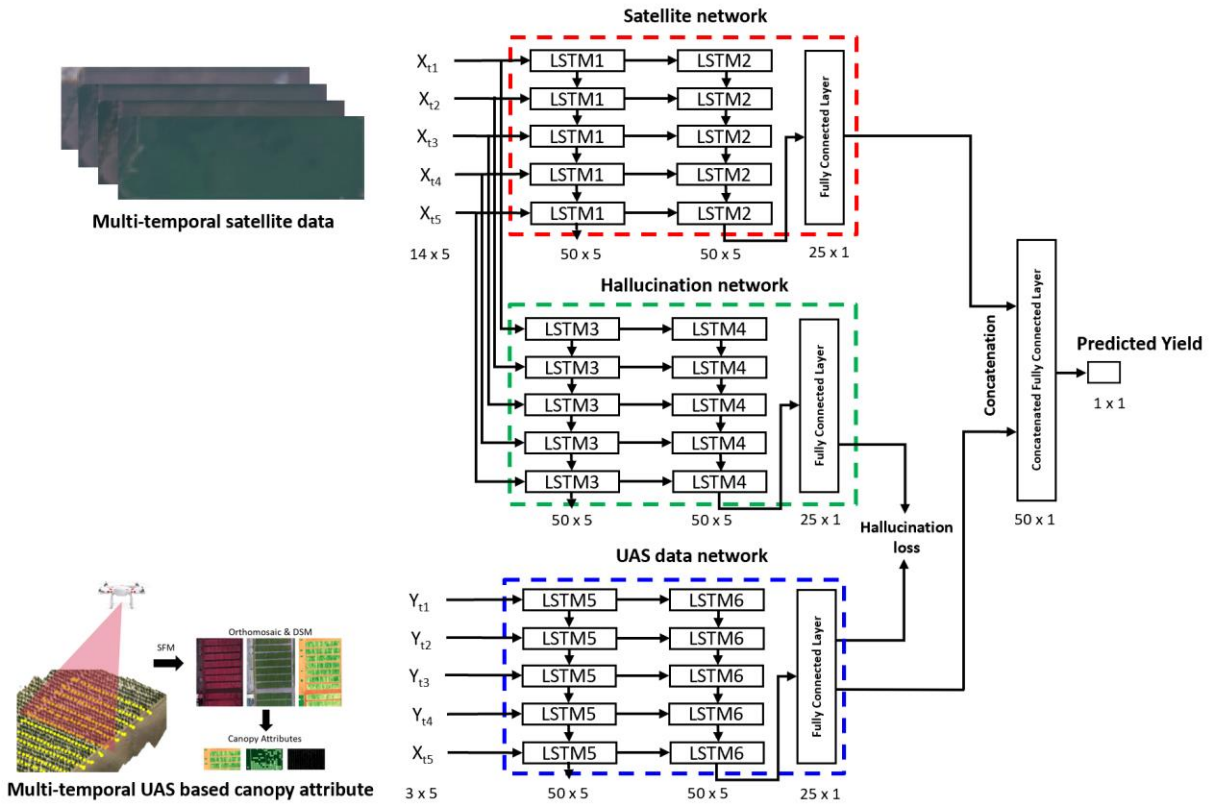

(a)

Figure 5.9. (a) Training the modality hallucination architecture. The hallucination branch is trained to take satellite data input and mimic the UAS derived canopy attribute mid-level activations, (b) Test time modality hallucination architecture.

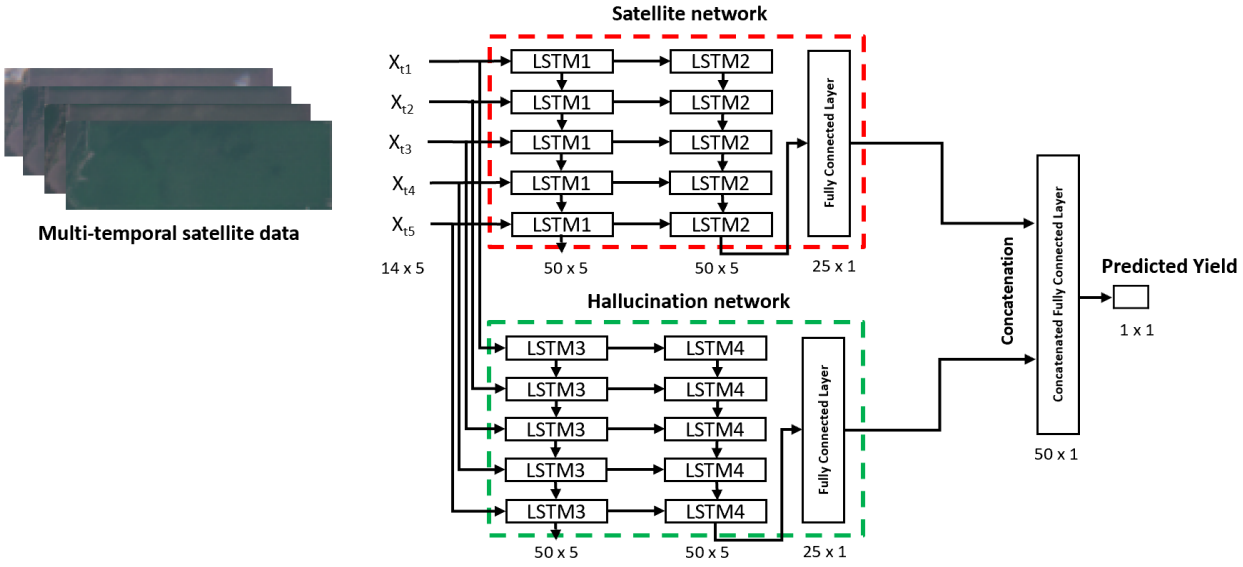

(b)

Figure 5.10. continued (a) Training the modality hallucination architecture. The hallucination branch is trained to take satellite data input and mimic the UAS derived canopy attribute mid-level activations, (b) Test time modality hallucination architecture.

The training module takes multi-temporal Sentinel-2A pixel values as explained in the baseline yield estimation model in Figure 5.7 as input through the satellite data network and corresponding UAS derived canopy attributes through the UAS data network. UAS derived aggregated canopy attributes over a given 10m x 10m grid were denoted by a temporal tensor in equation 5.2, where each $u^{(t)}$ represents a vector of size three representing aggregated canopy height, total canopy volume, and percentage canopy cover per grid. After satellite and UAS data were parsed through LSTM (output size 50) and fully connected (output size 25) layers in their respective networks, the fully connected layers from both networks were concatenated and predicted the corresponding yield with mean square error considered as loss function. Additional hyperparameters considered in the network were considered as presented in Table 5.3. The overall training of the network is twofold. As mentioned above, initial training is performed to predict the yield using both satellite data networks and the UAS data network. In the next step, the hallucination network is trained to mimic the UAS data network with the objective that activations after the fully connected layers should be similar between the hallucination and UAS data networks.

In particular, a loss function is added to minimize the difference between the UAS data activations after the fully connected layer A_l^{UNet} and the hallucination activations after fully connected layer A_l^{HNet} so that the hallucination loss $L_{Hallucination}(l)$ for the given layer is defined by Equation 5.3 as:

$$L_{Hallucination}(l) = \left|\sigma(A_l^{UNet}) - \sigma(A_l^{HNet})\right| \tag{5.3}$$

Where $\sigma(x) = 1/(1 + e^{-x})$ is sigmoidal function. The objective of the hallucination network activations is to match the corresponding UAS data mid-level activations; hence the parameters of the hallucination network must be independent of satellite as well as UAS data networks. Features extracted by the hallucination network should not be identical to mid-level features extracted by the UAS data network, as the inputs are satellite data for the hallucination network and UAS derived canopy attributes for the UAS data network. Hallucination loss can be theoretically applied at any mid-level; however, the objective is to learn an asymmetric transfer of information (to train the hallucination network using pre-learned UAS data network features). Consequently, weights and biases of the pre-learned network must be preserved to prevent any further training while training for hallucination loss. Therefore, the learning rates of all the previous layers with respect to the hallucination loss in the UAS data network were set to zero. This essentially freezes the UAS data network up to the fully connected layer in Figure 5.10 (a) so that the target UAS data activations are not altered during the hallucination loss backpropagation. At test time, only the satellite data passes through both the satellite data network and the hallucination network to produce two sets of intermediate features, which are concatenated after fully connected layers, which finally provides predicted yield after the activation.

5.4 Results and discussion

5.4.1 Implementation details

All the architectures presented in this chapter were implemented in python using Keras (Chollet, 2015) and Tensorflow (Abadi et al., 2016) deep learning libraries. All models were developed on a machine with a single GPU (NVIDIA® GeForce® GTX 1080 Ti) along with a dual-

core Intel i7-6600U 2.60GHz processor. In this study, hyperparameters of each architecture were determined using the Keras Tuner tool (O'Malley et al., 2019) and are presented in Table 5.3. Keras tuner tool consists of distributable hyperparameter optimization framework for hyperparameter search utilizing Bayesian Optimization, Hyperband, and Random Search algorithms. Adam optimizer (Kingma and Ba, 2014) with a learning rate of 10^{-3} was used to minimize the loss function (mean squared error between target and predicted yield). The number of training epochs chosen for the models considered in this study was 100, which was found to be sufficient for all the models to achieve convergence. The satellite time series data were normalized band-wise and for each epoch individually. Similarly, UAS derived canopy attributes were also normalized attribute-wise for each epoch individually.

5.4.2 Performance analysis of deep models

The deep models considered in this study were the baseline model, which utilized only the satellite data, along with cross-task knowledge transfer, and hallucination models, which utilized UAS data as side information along with satellite data. The prediction accuracy of deep learning models was evaluated using MSE and coefficient of determination (R^2). Figure 5.11 shows the linear fitting of the actual yield and model predicted yield for training, test, and independent test set using baseline, cross-task knowledge transfer, and hallucination models, respectively. Figure 5.12 shows the probability distributions of the estimated error between the predicted and actual yield for training, test, and independent test set using baseline, cross-task knowledge transfer, and hallucination models.

The linear fitting of the actual yield and model predicted yield presented in Figure 5.11 (a) indicates that multi-temporal satellite data can be successfully utilized to determine the yield, and a test R^2 of 0.71 confirmed that the baseline model could identify relevant features from multi-temporal satellite data (Sentinel-2A) for effective yield estimation. However, the test result over the independent test site was not encouraging (R^2 of 0.56). Coarser spatial resolution certainly limits the generalization capability of the satellite-based model. Additionally, partial cloud coverage, cloud shadow, and haze contribute to the degradation in the model performance.

However, despite showing a promising relationship between multi-temporal satellite data and the yield, there is a scope for improvement. Chapter 4 of this dissertation has shown that UAS data could provide more reliable crop canopy features for effective crop yield estimation. They can provide higher spatial resolution and have no issues with cloud coverage or haze. Consequently, models where UAS derived data were provided as side information performed better compared to the baseline model, as the UAS data provided complementary information countering the problems of the satellite data. A higher correlation was observed between actual yield values and model predicted yield values for both cross-task knowledge transfer and hallucination models presented in Figure 5.11 (b) and Figure 5.11 (c), respectively. Additionally, their generalization capability over the independent test site was found to be better compared to the baseline model.

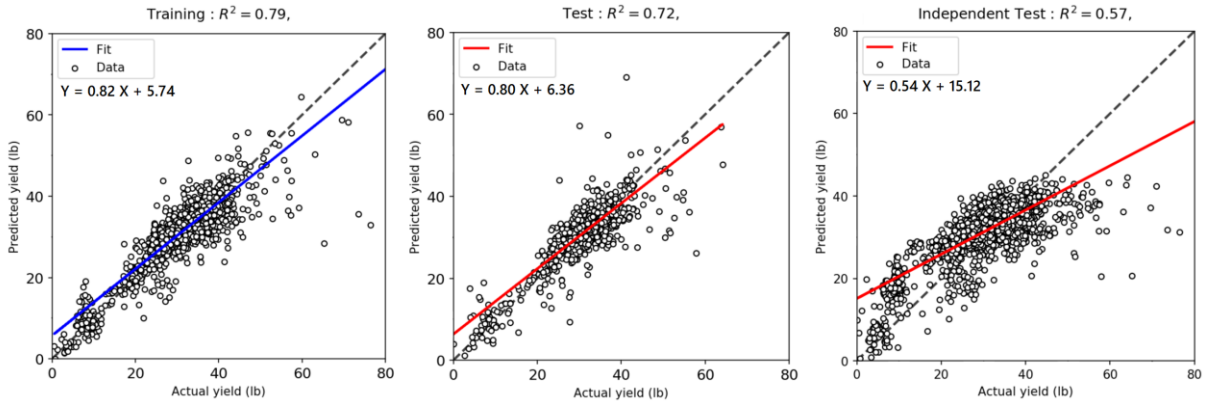

(a)

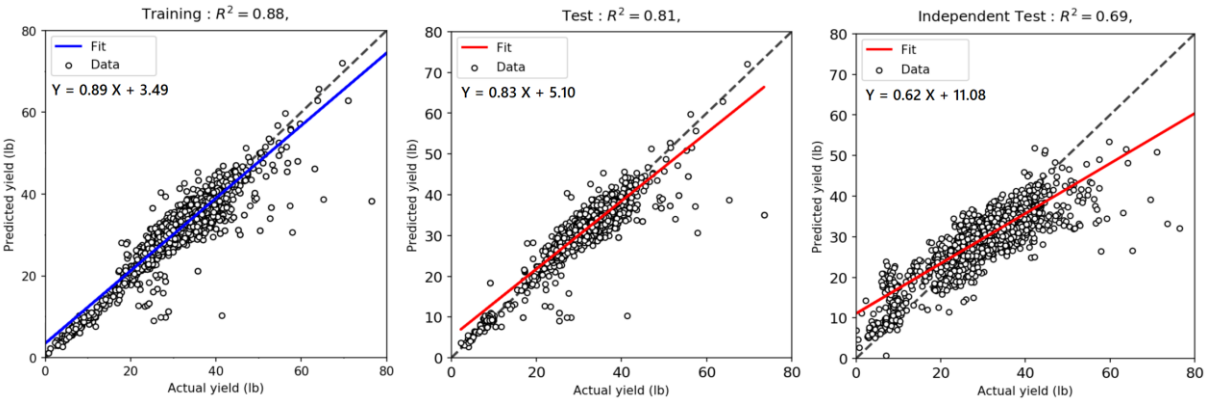

(b)

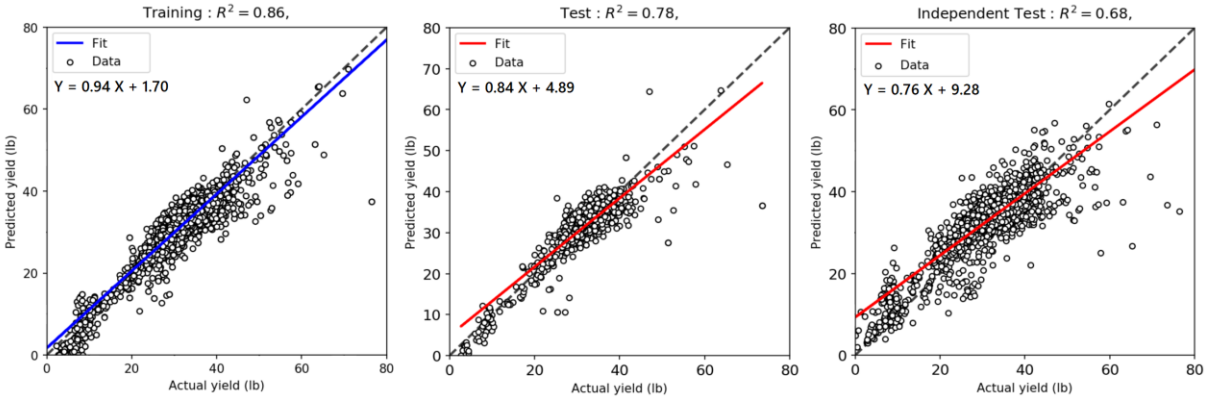

(c)

Figure 5.11. Linear fitting of the actual yield and model predicted yield for the training set (left) and test set (middle) and the independent test set (right) using (a) Baseline model, (b) Cross-task knowledge transfer model, and (c) Hallucination model.

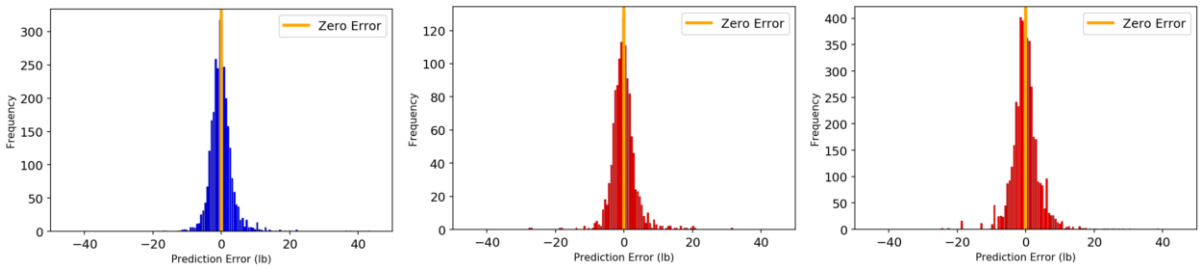

(a)

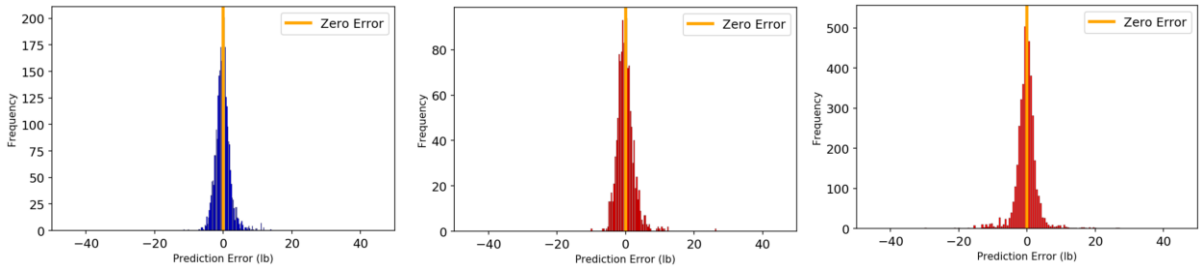

(b)

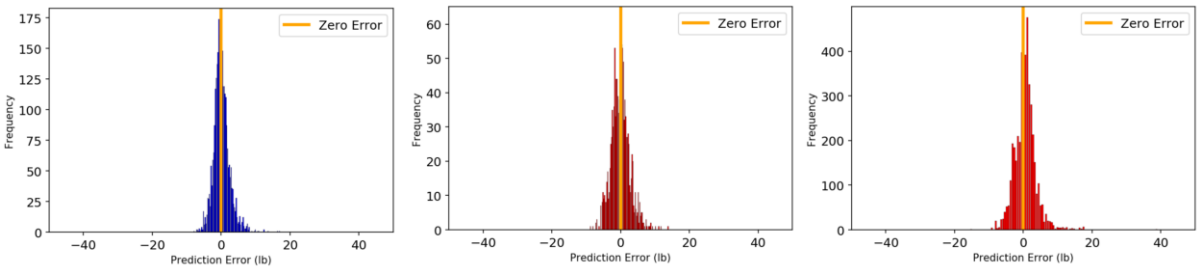

(c)

Figure 5.12. Error histogram of the actual yield and model predicted yield for the training set (left) and test set (middle) and the independent test set (right) using (a) Baseline model, (b) Cross-task knowledge transfer model, and (c) Hallucination model.

The error histogram over training, test, and independent test set presented in Figure 5.12 indicated that errors were centered around zero. A normality test of the error distributions suggested that errors were statistically random. Table 5.4 summarizes the accuracy assessment of deep models using R^2, MSE, and error in pounds per acre over training, test, and independent test sets, where the best value for each assessment criteria is highlighted in bold. MSE was reported per sample, which represented yield over 10m x 10m area in the field. Crop yield was also reported per acre for the main experimental field and independent test set (1528lbs/acre). Reported error per acre represented the absolute difference between pounds per acre computed using model

predicted yield and actual reported pounds per acre for both main experimental field and independent test site.

Relatively lower MSE and error per acre and higher R^2 for models using both cross-task knowledge transfer and hallucination model over baseline model suggest that adding UAS data as side information significantly improves model performance for not only training and test sets, but for the additional independent test set also. Highlighted values of R^2 indicate the higher performance of the cross-task knowledge transfer model over the hallucination model. However, there was no significant difference in the MSE, especially for the independent test site. Therefore, a Student's t-test was performed to check whether there was a significant difference in the performance of cross-task knowledge transfer and modality hallucination architecture (Table 5.5). A lower P value (0.001) for the training set indicated that the models were significantly different, suggesting a better training performance of cross-task knowledge transfer architecture over the modality hallucination. However, P values for the test set and independent test set suggested no significant difference in generalization capability between the architectures.

Table 5.4. Accuracy assessment of deep models over training, test, and independent test cases using a coefficient of determination (R^2), mean squared error (MSE) per grid, and error per acre.

Method	Training			Test			Independent Test		
	R^2	MSE/grid (lb^2)	Error/acre (lb^2)	R^2	MSE/grid (lb^2)	Error/acre (lb^2)	R^2	MSE/grid (lb^2)	Error/acre (lb^2)
Baseline Model	0.79	3.4	39.2	0.72	3.8	48.3	0.57	4.6	101.0
Cross-task transfer Model	**0.88**	**2.1**	**21.5**	**0.80**	**2.8**	**34.0**	**0.69**	**3.2**	**45.4**
Hallucination model	0.86	2.3	22.2	0.78	2.9	34.8	0.68	**3.2**	45.9

Table 5.5. T-test analysis for cross-task knowledge transfer and modality hallucination architecture.

Method	T value	P-value
Training	3.45	0.001
Test	-0.08	**0.933**
Independent Test	1.68	**0.091**

Error per acre was also lowest amongst all for the cross-task knowledge transfer model. The cross-task knowledge transfer model resulted in yield estimates with the discrepancy of 34lb/acre for the test set and 45.5lb/acre for the independent test set, which was 2.2% and ~3.0% of the reported 1528lb/acre yield for both fields. In comparison, the hallucination model resulted in yield estimates with a discrepancy of 34.8lb/acre for the test set and 45.9lb/acre for the independent test set, which was 2.3% and 3.0% of the reported yield per acre, which is very similar to cross-task knowledge transfer model performance. No benchmark dataset currently exists for multi-temporal satellite-based pixel-wise crop yield estimation supplemented by UAS derived information. This dataset is the first step towards more reproducible and comparable methodological work in this field.

5.5 Conclusion and future work

UAS technology efficiently works over small-size research fields or breeding trial fields; nevertheless, large aerial coverage using UAS is not feasible. Alternatively, satellite images have the advantage of covering vast areas, but they provide coarser spatial resolution data. To overcome the limitation of UAS and satellite sensors, a deep learning-based hybrid regression model was proposed for yield prediction. This study explored deep learning-based methodologies to incorporate additional information in the form of UAS derived canopy attributes to improve the multi-temporal satellite-only yield estimation model. This was accomplished through cross-task knowledge transfer architecture and modality hallucination architecture which combines a multi-temporal satellite-based representation with an additional and complementary UAS based representation to improve crop yield estimation. Hence, the model was capable of predicting the crop yield without utilizing UAS based representation at the test time. The present study provides a baseline deep learning model utilizing multi-temporal satellite data for effective crop yield estimation with a test R^2 of 0.71. Cross-task knowledge transfer architecture and modality hallucination architecture outperformed the baseline model with a higher coefficient of determination and lower MSE. However, the performance of cross-task knowledge transfer

architecture and modality hallucination architecture were not significantly different with respect to their generalization capability.

Future work may be extended in the following directions:

Deep network design: Current deep architectures presented in this study utilized LSTM to handle the temporal dimension of the input data as they were found to be better in handling the gradient over the time series compared to traditional RNNs. In the future, more network elements capable of handling temporal dimensions could be tried, such as deep attention networks (Sorokin et al., 2015), transformers networks (Wang et al., 2019) which outperform LSTM networks, especially in natural language processing applications.

Fusion methodologies: The scope of this study was to explore deep learning-based information fusion architecture to incorporate different modalities for effective crop yield estimation. In addition to transfer learning methodologies considered in this study, adversarial domain adaptation can also be tested (Tzeng et al., 2017), as adversarial learning mechanism is capable of generating domain invariant features to train robust deep networks across diverse domains. Future efforts should also include an ensemble approach, as it is well known that ensemble methods tend to outperform the single model approach.

Investigate more data sources: Current methodology incorporated freely available Sentinel-2 data. Initially, Planet data was also considered; however, relatively lower spectral resolution and poor radiometric calibration hindered the prediction accuracy. As future work, more efforts are required to explore various commercial high-resolution satellite datasets.

Application to diverse datasets: Future efforts may also focus on extending the proposed methodology for multi-year analysis as more data will be available to incorporate. Additionally, more data across different locations could also be incorporated to improve the model generalization capability. It is not always possible to have the same number of temporal epochs in the period of interest across geographical locations with multi-year and multi-location data. Future efforts will also focus on handling a different number of epochs for training and test sets.

Adaptation for other crops: Proposed methodology focused on the cotton crop; future efforts may also test the efficacy of the current methodology for other crops with a focus on crop canopy attribute selection for specific crops and inclusion of additional features such as weather, treatment, soil property, and irrigation information.

SUMMARY AND CONCLUSION

This dissertation focused on developing high throughput phenotyping framework using multi-temporal, high spatial resolution UAS based images. The overall objective of this dissertation was to investigate the suitability of various UAS derived canopy attributes for crop yield estimation and to exploit this limited available information to improve satellite-based large area yield estimation. Several studies were undertaken with the aim of developing a yield estimation framework using machine learning. Initially, to test the reliability of the UAS derived plant parameters, a comparative study was designed for comparison of two management practices in cotton, conventional tillage (CT) and no-tillage (NT), which revealed that there was a significant difference between cotton growth under CT and NT. Unlike manual measurements, which relied on limited samples, UAS technology provided the capability to exploit the entire population. This makes UAS derived data more robust and reliable. Additionally, an inter-comparison study was designed to compare canopy cover derived from RGB and multispectral sensors over multiple flights during the growing season of the cotton crop. An RGB-based canopy cover model was proposed, which provided an affordable alternative to the multispectral sensors, which are considered relatively more stable but have more sensitive detectors and are relatively more complex and expensive.

After assessing the reliability of UAS derived canopy parameters, a novel machine learning framework was developed for crop yield estimation of cotton crops using multi-temporal UAS data. This study revealed that UAS derived multi-temporal data along with non-temporal and qualitative data can be combined within a machine learning framework to provide a reliable estimation of crop yield and provide an effective understanding for crop management. The proposed methodology is promising and efficiently works over relatively smaller research fields or breeding trial fields; nevertheless, large aerial coverage using UAS is not practically viable. Alternatively, satellite images have the advantage of covering a vast area, but they provide coarser spatial resolution data. To overcome the limitation of UAS and satellite sensors, a deep learning-based modality fusion is explored for effective yield prediction. The inherent challenge lies in the

fact that with the fact that UAS data is only available over a limited area. Consequently, the proposed model can utilize this complementary information only at the time of training, and while estimating crop yield over the test samples, the model relies only on satellite data. To incorporate the aforementioned constrained, the proposed deep architectures based on cross task knowledge transfer and modality hallucination efficiently handle the selective availability of the UAS data by utilizing it at the time of training the crop yield prediction model, while the testing model only requires the satellite data. The generalization capability of the models was tested over an independent test site. The main contribution of this study was to provide a proof of principle for learning through side information for effective crop yield estimation utilizing multi-modality remote sensing data. To the best of the authors' knowledge, this is the first study that tackles the limited availability of UAS and uses it as complementary information to improve satellite-based yield estimation. Propose deep learning methodology may be adapted to incorporate diverse datasets (multi-year and multi-location) to test the efficacy of the proposed methodology further. Additionally, this research is limited to cotton yield estimation, and it could be extended to develop yield estimation models for other crops, which is scope for future work.

APPENDIX A. CANOPY PARAMETER ETIMATION

For canopy height computation, a UAS baseline flight was conducted before planting to generate a digital terrain model (DTM). Further, absolute canopy height or canopy height model (CHM) was obtained by subtracting DTM from each DSM generated using later UAS data collection in the growing season (Fig. A.1). After computing CHM maps, the average canopy height per plot was computed.

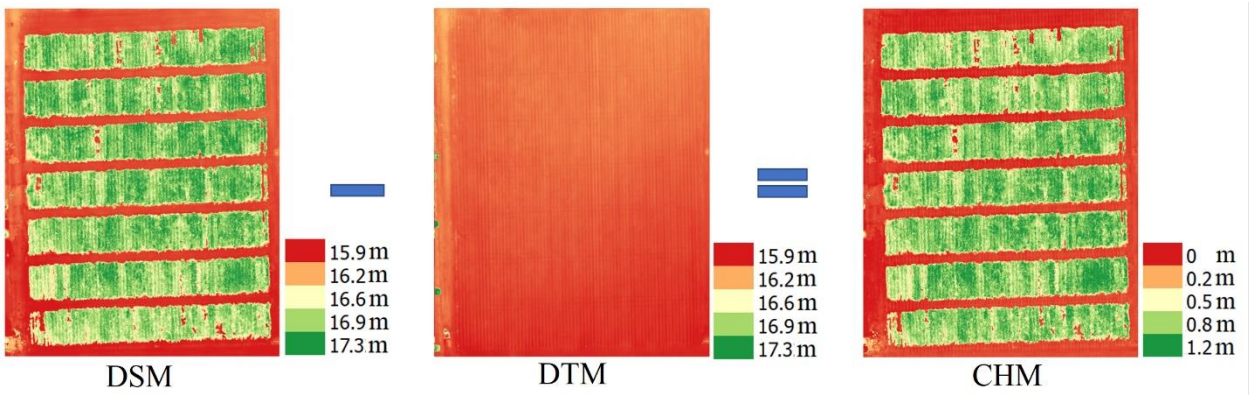

Figure A.1. Procedure to extract canopy height from UAS collected imagery. The digital terrain model (DTM) represents the soil elevation and is subtracted from the digital surface model (DSM) (soil + canopy elevation) to create the canopy height model (CHM)

To compute percentage canopy cover per plot, RGB Orthomosaic was classified into a binary map using the Canopeo algorithm (Patrignani and Ochsner, 2015)(Equation A.1), where white pixels represent canopy and black pixels represent non-canopy. Later, a ratio of canopy pixels over the total number of pixels within a plot was computed using Equation A.2 to compute the percentage canopy cover per plot (Fig. A.2).

$$canopy = \left(\frac{blue}{green} < \theta_2\right) \text{AND } \left(\frac{red}{green} < \theta_1\right) \text{ AND } (2\ green - blue - red > \theta_3) \quad \text{(A.1)}$$

Where, red, blue, and green represent values of the pixel in the corresponding band and $\theta_1 = 0.95,\ \theta_2 = 0.95,\ \theta_3 = 20.$

$$CC = \frac{(\sum(GSD^2)\ if\ Canopy\ )}{\sum(GSD^2)} * 100 \quad \text{(A.2)}$$

Where, GSD is the ground sample distance which is the distance between two consecutive pixel centers measured on the ground.

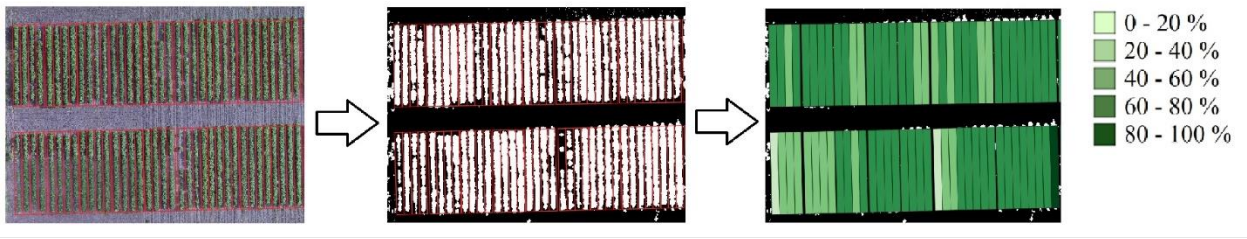

Figure A.2. Canopy cover estimation from the orthomosaic images (Red polygons: individual crop plots and each plot was ~1m x 10m): shows a natural color orthomosaic image acquired from UAS platform, followed by binary classification results of the orthomosaic image (white: canopy class, black: non-canopy class) and finally the estimated grid wise CC.

Canopy volume per plot was computed as the summation of the products of the height of the pixels and the pixel size within the plot (Equation A.3).

$$CV = \sum(H_i \times GSD^2) \tag{A.3}$$

Where, H_i is the height of the ith pixel.

NDVI images were computed as the ratio of the difference between near-infrared (NIR) and red bands to the sum of NIR and red bands (Rouse et al., 1974) (Equation A.4). To compute average NDVI values per plot, the average of all pixel values within each plot was computed.

$$\text{NDVI} = \frac{(NIR - Red)}{(NIR + Red)} \tag{A.4}$$

Excessive Greenness Index images were generated using Equation A.5 (Woebbecke et al., 1995). Later, the average ExG per plot was computed by averaging all the pixels of ExG images within each plot.

$$ExG = 2G - R - B \tag{A.5}$$

Where, $R = red/\max(red)$, $G = green/\max(green)$ and $R = blue/\max(blue)$

Non-temporal features considered in this research were cotton boll count, boll size, and boll volume, which were computed as suggested by Jung et al. (2018). Initially, an RGB

orthomosaic in which the cotton bolls were clearly visible was considered. To differentiate open cotton bolls from the background objects, binary classification of the orthomosaic image was performed after visual inspection of the boundaries between cotton bolls and background objects. Later, a connected component labeling algorithm with a 4-connectivity rule was applied to the classified image to identify the individual cotton boll clusters. Further, patch size analysis was performed to calculate spatial characteristics of open cotton bolls, including area and equivalent diameter. Finally, the spatial characteristics of the individual cotton bolls were summarized for each plot, such as boll count, boll size, and boll volume.

REFERENCES

Abadi, M., Barham, P., Chen, J., Chen, Z., Davis, A., Dean, J., Devin, M., Ghemawat, S., Irving, G., Isard, M., 2016. Tensorflow: A system for large-scale machine learning. DOI: https://www.usenix.org/conference/osdi16/technical-sessions/presentation/abadi

Andújar, D., Ribeiro, A., Fernández-Quintanilla, C., Dorado, J., 2016. Using depth cameras to extract structural parameters to assess the growth state and yield of cauliflower crops. Computers and Electronics in Agriculture 122, 67-73.DOI: https://doi.org/10.1016/j.compag.2016.01.018

Ashapure, A., Jung, J., Chang, A., Oh, S., Maeda, M., Landivar, J., 2019a. A Comparative Study of RGB and Multispectral Sensor-Based Cotton Canopy Cover Modelling Using Multi-Temporal UAS Data. Remote Sensing 11, 2757.DOI: https://doi.org/10.3390/rs11232757

Ashapure, A., Jung, J., Chang, A., Oh, S., Yeom, J., Maeda, M., Maeda, A., Dube, N., Landivar, J., Hague, S., 2020a. Developing a machine learning based cotton yield estimation framework using multi-temporal UAS data. ISPRS Journal of Photogrammetry and Remote Sensing 169, 180-194.DOI: https://doi.org/10.1016/j.isprsjprs.2020.09.015

Ashapure, A., Jung, J., Oh, S., Chang, A., Dube, N., Landivar, J., 2020b. Combining UAS and Sentinel-2 Data to Estimate Canopy Parameters of a Cotton Crop Using Machine Learning, IGARSS 2020-2020 IEEE International Geoscience and Remote Sensing Symposium. IEEE, pp. 5199-5202. DOI: 10.1109/IGARSS39084.2020.9324342

Ashapure, A., Jung, J., Yeom, J., Chang, A., Maeda, M., Maeda, A., Landivar, J., 2019b. A novel framework to detect conventional tillage and no-tillage cropping system effect on cotton growth and development using multi-temporal UAS data. ISPRS journal of photogrammetry and remote sensing 152, 49-64.DOI: https://doi.org/10.1016/j.isprsjprs.2019.04.003

Ashapure, A., Oh, S., Marconi, T.G., Chang, A., Jung, J., Landivar, J., Enciso, J., 2019c. Unmanned aerial system based tomato yield estimation using machine learning, Autonomous Air and Ground Sensing Systems for Agricultural Optimization and Phenotyping IV. International Society for Optics and Photonics, p. 110080O. DOI: https://doi.org/10.1117/12.2519129

Awad, M., Khanna, R., 2015. Support vector regression, Efficient learning machines. Springer, pp. 67-80. DOI: https://doi.org/10.1007/978-1-4302-5990-9_4

Behmann, J., Mahlein, A.-K., Rumpf, T., Römer, C., Plümer, L., 2015. A review of advanced machine learning methods for the detection of biotic stress in precision crop protection. Precision Agriculture 16, 239-260.DOI: https://doi.org/10.1007/s11119-014-9372-7

Bendig, J., Yu, K., Aasen, H., Bolten, A., Bennertz, S., Broscheit, J., Gnyp, M.L., Bareth, G., 2015. Combining UAV-based plant height from crop surface models, visible, and near infrared vegetation indices for biomass monitoring in barley. International Journal of Applied Earth Observation and Geoinformation 39, 79-87.DOI: https://doi.org/10.1016/j.jag.2015.02.012

Bengio, Y., Courville, A., Vincent, P., 2013. Representation learning: A review and new perspectives. IEEE transactions on pattern analysis and machine intelligence 35, 1798-1828.DOI: 10.1109/TPAMI.2013.50

Booth, D.T., Cox, S.E., Berryman, R.D., 2006. Point sampling digital imagery with 'SamplePoint'. Environmental Monitoring and Assessment 123, 97-108.DOI: https://doi.org/10.1007/s10661-005-9164-7

Brox, T., Weickert, J., 2006. Level set segmentation with multiple regions. IEEE Transactions on Image Processing 15, 3213-3218.DOI: 10.1109/TIP.2006.877481

Burrough, P.A., McDonnell, R., McDonnell, R.A., Lloyd, C.D., 2015. Principles of geographical information systems. Oxford university press.

Calders, K., Newnham, G., Burt, A., Murphy, S., Raumonen, P., Herold, M., Culvenor, D., Avitabile, V., Disney, M., Armston, J., 2015. Nondestructive estimates of above-ground biomass using terrestrial laser scanning. Methods in Ecology and Evolution 6, 198-208.DOI: https://doi.org/10.1111/2041-210X.12301

Chen, G., Hay, G.J., 2011. A support vector regression approach to estimate forest biophysical parameters at the object level using airborne lidar transects and quickbird data. Photogrammetric Engineering & Remote Sensing 77, 733-741.DOI: https://doi.org/10.14358/PERS.77.7.733

Chianucci, F., Disperati, L., Guzzi, D., Bianchini, D., Nardino, V., Lastri, C., Rindinella, A., Corona, P., 2016. Estimation of canopy attributes in beech forests using true colour digital images from a small fixed-wing UAV. International journal of applied earth observation and geoinformation 47, 60-68.DOI: https://doi.org/10.1016/j.jag.2015.12.005

Chlingaryan, A., Sukkarieh, S., Whelan, B., 2018. Machine learning approaches for crop yield prediction and nitrogen status estimation in precision agriculture: A review. Computers and electronics in agriculture 151, 61-69.DOI: https://doi.org/10.1016/j.compag.2018.05.012

Chollet, F.a.o., 2015. Keras. GitHub. DOI: https://github.com/fchollet/keras

Chu, T., Chen, R., Landivar, J.A., Maeda, M.M., Yang, C., Starek, M.J., 2016. Cotton growth modeling and assessment using unmanned aircraft system visual-band imagery. Journal of Applied Remote Sensing 10, 036018.DOI: https://doi.org/10.1117/1.JRS.10.036018

Chuai-Aree, S., Lursinsap, C., Sophasathit, P., Siripant, S., 2001. Fuzzy c-mean: A statistical feature classification of text and image segmentation method. International Journal of Uncertainty, Fuzziness and Knowledge-Based Systems 9, 661-671. DOI: https://doi.org/10.1142/S0218488501001137

Clement, J., Constable, G., Liu, S., 2014. Increasing cotton seed fibre density as a breeding strategy to improve fibre fineness. Field Crops Research 160, 81-89.DOI: https://doi.org/10.1016/j.fcr.2014.01.005

Clevers, J., Kooistra, L., Van Den Brande, M., 2017. Using Sentinel-2 data for retrieving LAI and leaf and canopy chlorophyll content of a potato crop. Remote Sensing 9, 405.DOI: https://doi.org/10.3390/rs9050405

Dash, C.S.K., Behera, A.K., Dehuri, S., Cho, S.-B., 2016. Radial basis function neural networks: a topical state-of-the-art survey. Open Computer Science 6.DOI: https://doi.org/10.1515/comp-2016-0005

Davi, H., Soudani, K., Deckx, T., Dufrene, E., Le Dantec, V., Francois, C., 2006. Estimation of forest leaf area index from SPOT imagery using NDVI distribution over forest stands. International Journal of Remote Sensing 27, 885-902.DOI: https://doi.org/10.1080/01431160500227896

Derpsch, R., Franzluebbers, A., Duiker, S., Reicosky, D., Koeller, K., Friedrich, T., Sturny, W., Sá, J., Weiss, K., 2014. Why do we need to standardize no-tillage research? Soil and Tillage Research 137, 16-22.DOI: http://dx.doi.org/10.1016/j.still.2013.10.002

Dougherty, E.R., 1992. An introduction to morphological image processing. SPIE, 1992

Fang, S., Tang, W., Peng, Y., Gong, Y., Dai, C., Chai, R., Liu, K., 2016. Remote estimation of vegetation fraction and flower fraction in oilseed rape with unmanned aerial vehicle data. Remote Sensing 8, 416.DOI: https://doi.org/10.3390/rs8050416

Feng, A., Sudduth, K., Vories, E., Zhang, M., Zhou, J., 2018. Cotton Yield Estimation based on Plant Height From UAV-based Imagery Data, 2018 ASABE Annual International Meeting. American Society of Agricultural and Biological Engineers, p. 1. DOI: 10.13031/aim.201800483

Ferencz, C., Bognar, P., Lichtenberger, J., Hamar, D., Tarcsai, G., Timár, G., Molnár, G., Pásztor, S., Steinbach, P., Székely, B., 2004. Crop yield estimation by satellite remote sensing. International Journal of Remote Sensing 25, 4113-4149.DOI: https://doi.org/10.1080/01431160410001698870

Fernandez-Gallego, J.A., Kefauver, S.C., Kerfal, S., Araus, J.L., 2018. Comparative canopy cover estimation using RGB images from UAV and ground, Remote Sensing for Agriculture, Ecosystems, and Hydrology XX. International Society for Optics and Photonics, p. 107830J. DOI: https://doi.org/10.1117/12.2501531

Freeland Jr, T.B., Pettigrew, B., Thaxton, P., Andrews, G.L., 2006. Agrometeorology and cotton production. World Meteorological Organization.DOI: http://www.wamis.org/agm/gamp/GAMP_Chap10.pdf

Fuentes-Peailillo, F., Ortega-Farias, S., Rivera, M., Bardeen, M., Moreno, M., 2018. Comparison of vegetation indices acquired from RGB and Multispectral sensors placed on UAV, 2018 IEEE International Conference on Automation/XXIII Congress of the Chilean Association of Automatic Control (ICA-ACCA). IEEE, pp. 1-6. DOI: 10.1109/ICA-ACCA.2018.8609861

Fushiki, T., 2011. Estimation of prediction error by using K-fold cross-validation. Statistics and Computing 21, 137-146.DOI: 10.1007/s11222-009-9153-8

Gandhi, N., Petkar, O., Armstrong, L.J., 2016. Rice crop yield prediction using artificial neural networks, 2016 IEEE Technological Innovations in ICT for Agriculture and Rural Development (TIAR). IEEE, pp. 105-110. DOI: 10.1109/TIAR.2016.7801222

Garson, D.G., 1991. Interpreting neural network connection weights.

Gevrey, M., Dimopoulos, I., Lek, S., 2003. Review and comparison of methods to study the contribution of variables in artificial neural network models. Ecological modelling 160, 249-264.DOI: https://doi.org/10.1016/S0304-3800(02)00257-0

Ghazal, M., Al Khalil, Y., Hajjdiab, H., 2015. UAV-based remote sensing for vegetation cover estimation using NDVI imagery and level sets method, Signal Processing and Information Technology (ISSPIT), 2015 IEEE International Symposium on. IEEE, pp. 332-337. DOI: 10.1109/ISSPIT.2015.7394354

Giller, K.E., Andersson, J.A., Corbeels, M., Kirkegaard, J., Mortensen, D., Erenstein, O., Vanlauwe, B., 2015. Beyond conservation agriculture. Frontiers in plant science 6.DOI: https://doi.org/10.3389/fpls.2015.00870

Gopal, P.M., Bhargavi, R., 2019. A novel approach for efficient crop yield prediction. Computers and Electronics in Agriculture 165, 104968.DOI: https://doi.org/10.1016/j.compag.2019.104968

Gracia-Romero, A., Kefauver, S.C., Vergara-Díaz, O., Zaman-Allah, M.A., Prasanna, B.M., Cairns, J.E., Araus, J.L., 2017. Comparative performance of ground vs. aerially assessed RGB and multispectral indices for early-growth evaluation of maize performance under phosphorus fertilization. Frontiers in Plant Science 8, 2004.DOI: https://doi.org/10.3389/fpls.2017.02004

Grybas, H., Congalton, R.G., 2021. A Comparison of Multi-Temporal RGB and Multispectral UAS Imagery for Tree Species Classification in Heterogeneous New Hampshire Forests. Remote Sensing 13, 2631.DOI: https://doi.org/10.3390/rs13132631

Guo, L.-J., Lin, S., Liu, T.-Q., Cao, C.-G., Li, C.-F., 2016. Effects of conservation tillage on topsoil microbial metabolic characteristics and organic carbon within aggregates under a rice (Oryza sativa L.)–wheat (Triticum aestivum L.) cropping system in central China. PloS one 11, e0146145.DOI: https://doi.org/10.1371/journal.pone.0146145

Gupta, S., Girshick, R., Arbeláez, P., Malik, J., 2014. Learning rich features from RGB-D images for object detection and segmentation, European conference on computer vision. Springer, pp. 345-360. DOI: 10.1007/978-3-319-10584-0_23

Halevy, A., Norvig, P., Pereira, F., 2009. The unreasonable effectiveness of data. IEEE Intelligent Systems 24, 8-12.DOI: 10.1109/MIS.2009.36

Harwin, S., Lucieer, A., 2012. Assessing the accuracy of georeferenced point clouds produced via multi-view stereopsis from unmanned aerial vehicle (UAV) imagery. Remote Sensing 4, 1573-1599.DOI: https://doi.org/10.3390/rs4061573

Hassan, M.A., Yang, M., Rasheed, A., Jin, X., Xia, X., Xiao, Y., He, Z., 2018. Time-Series Multispectral Indices from Unmanned Aerial Vehicle Imagery Reveal Senescence Rate in Bread Wheat. Remote Sensing 10, 809.DOI: https://doi.org/10.3390/rs10060809

Heidarian Dehkordi, R., Burgeon, V., Fouche, J., Placencia Gomez, E., Cornelis, J.-T., Nguyen, F., Denis, A., Meersmans, J., 2020. Using UAV collected RGB and multispectral images to evaluate winter wheat performance across a site characterized by century-old biochar patches in Belgium. Remote Sensing 12, 2504.DOI: https://doi.org/10.3390/rs12152504

Hengl, T., Nussbaum, M., Wright, M.N., Heuvelink, G.B., Gräler, B., 2018. Random forest as a generic framework for predictive modeling of spatial and spatio-temporal variables. PeerJ 6, e5518.DOI: https://doi.org/10.7717/peerj.5518

Herzig, P., Borrmann, P., Knauer, U., Klück, H.-C., Kilias, D., Seiffert, U., Pillen, K., Maurer, A., 2021. Evaluation of RGB and Multispectral Unmanned Aerial Vehicle (UAV) Imagery for High-Throughput Phenotyping and Yield Prediction in Barley Breeding. Remote Sensing 13, 2670.DOI: https://doi.org/10.3390/rs13142670

Hien, D.T.T., Huan, H.X., 2015. An effective solution to regression problem by RBF neuron network. International Journal of Operations Research and Information Systems (IJORIS) 6, 57-74.DOI: 10.4018/IJORIS.2015100104

Hochreiter, S., Schmidhuber, J., 1997. Long short-term memory. Neural computation 9, 1735-1780.DOI: 10.1162/neco.1997.9.8.1735

Hoffman, J., Gupta, S., Darrell, T., 2016. Learning with side information through modality hallucination, Proceedings of the IEEE Conference on Computer Vision and Pattern Recognition, pp. 826-834. DOI: 10.1109/CVPR.2016.96

Holman, F., Riche, A., Michalski, A., Castle, M., Wooster, M., Hawkesford, M., 2016. High throughput field phenotyping of wheat plant height and growth rate in field plot trials using UAV based remote sensing. Remote Sensing 8, 1031.DOI: https://doi.org/10.3390/rs8121031

Hu, J., Su, Y., Tan, B., Huang, D., Yang, W., Schull, M., Bull, M.A., Martonchik, J.V., Diner, D.J., Knyazikhin, Y., 2007. Analysis of the MISR LAI/FPAR product for spatial and temporal coverage, accuracy and consistency. Remote Sensing of Environment 107, 334-347.DOI: https://doi.org/10.1016/j.rse.2006.06.020

Hultquist, C., Chen, G., Zhao, K., 2014. A comparison of Gaussian process regression, random forests and support vector regression for burn severity assessment in diseased forests. Remote sensing letters 5, 723-732.DOI: https://doi.org/10.1080/2150704X.2014.963733

Hulvey, K.B., Thomas, K., Thacker, E., 2018. A Comparison of Two Herbaceous Cover Sampling Methods to Assess Ecosystem Services in High-Shrub Rangelands: Photography-Based Grid Point Intercept (GPI) Versus Quadrat Sampling. Rangelands 40, 152-159.DOI: https://doi.org/10.1016/j.rala.2018.08.004

Hunt, M.L., Blackburn, G.A., Carrasco, L., Redhead, J.W., Rowland, C.S., 2019. High resolution wheat yield mapping using Sentinel-2. Remote Sensing of Environment 233, 111410.DOI: https://doi.org/10.1016/j.rse.2019.111410

Iqbal, M., Hayat, K., Atiq, M., Khan, N., 2008. Evaluation and prospects of F2 genotypes of cotton (Gossypium hirsutum L) for yield and yield components. Int. J. Agric. Biol 10, 442-446

İskenderoğlu, F.C., Baltacioğlu, M.K., Demir, M.H., Baldinelli, A., Barelli, L., Bidini, G., 2020. Comparison of support vector regression and random forest algorithms for estimating the SOFC output voltage by considering hydrogen flow rates. International Journal of Hydrogen Energy 45, 35023-35038.DOI: https://doi.org/10.1016/j.ijhydene.2020.07.265

Jung, J., Maeda, M., Chang, A., Landivar, J., Yeom, J., McGinty, J., 2018. Unmanned aerial system assisted framework for the selection of high yielding cotton genotypes. Computers and Electronics in Agriculture 152, 74-81.DOI: https://doi.org/10.1016/j.compag.2018.06.051

Jung, Y., Hu, J., 2015. A K-fold averaging cross-validation procedure. Journal of nonparametric statistics 27, 167-179.DOI: https://doi.org/10.1080/10485252.2015.1010532

Kazerani, B., 2012. Determination of the best cotton cultivars and selection criteria to improve yield in Gorgan climatic region. African Journal of Agricultural Research 7, 2004-2011.DOI: https://doi.org/10.5897/AJAR11.1602

Kennedy, C.W., Hutchinson, R.L., 2001. Cotton growth and development under different tillage systems. Crop Science 41, 1162-1168.DOI: https://doi.org/10.2135/cropsci2001.4141162x

Khaki, S., Khalilzadeh, Z., Wang, L., 2019. Classification of Crop Tolerance to Heat and Drought—A Deep Convolutional Neural Networks Approach. Agronomy 9, 833.DOI: https://doi.org/10.3390/agronomy9120833

Khaki, S., Wang, L., Archontoulis, S.V., 2020. A CNN-RNN Framework for Crop Yield Prediction. Frontiers in Plant Science 10, 1750.DOI: https://doi.org/10.3389/fpls.2019.01750

Khoshroo, A., Emrouznejad, A., Ghaffarizadeh, A., Kasraei, M., Omid, M., 2018. Sensitivity analysis of energy inputs in crop production using artificial neural networks. Journal of cleaner production 197, 992-998.DOI: https://doi.org/10.1016/j.jclepro.2018.05.249

Kim, N., Ha, K.-J., Park, N.-W., Cho, J., Hong, S., Lee, Y.-W., 2019. A comparison between major artificial intelligence models for crop yield prediction: Case study of the midwestern united states, 2006–2015. ISPRS International Journal of Geo-Information 8, 240.DOI: https://doi.org/10.3390/ijgi8050240

Kingma, D.P., Ba, J., 2014. Adam: A method for stochastic optimization. arXiv preprint arXiv:1412.6980.DOI: https://arxiv.org/abs/1412.6980v9

Lamonaca, A., Corona, P., Barbati, A., 2008. Exploring forest structural complexity by multi-scale segmentation of VHR imagery. Remote Sensing of Environment 112, 2839-2849.DOI: https://doi.org/10.1016/j.rse.2008.01.017

Landivar, J.A., Reddy, K.R., Hodges, H.F., 2010. Physiological simulation of cotton growth and yield, Physiology of Cotton. Springer, pp. 318-331. DOI: https://doi.org/10.1007/978-90-481-3195-2_28

Le, P., Zuidema, W., 2016. Quantifying the vanishing gradient and long distance dependency problem in recursive neural networks and recursive LSTMs. arXiv preprint arXiv:1603.00423.DOI: https://arxiv.org/abs/1603.00423

Lima-Cueto, F.J., Blanco-Sepúlveda, R., Gómez-Moreno, M.L., Galacho-Jiménez, F.B., 2019. Using Vegetation Indices and a UAV Imaging Platform to Quantify the Density of Vegetation Ground Cover in Olive Groves (Olea Europaea L.) in Southern Spain. Remote Sensing 11, 2564.DOI: https://doi.org/10.3390/rs11212564

Lipton, Z.C., Berkowitz, J., Elkan, C., 2015. A critical review of recurrent neural networks for sequence learning. arXiv preprint arXiv:1506.00019.DOI: https://arxiv.org/abs/1506.00019

Lowe, D.G., 2004. Distinctive image features from scale-invariant keypoints. International journal of computer vision 60, 91-110.DOI: https://doi.org/10.1023/B:VISI.0000029664.99615.94

Lucieer, A., Jong, S.M.d., Turner, D., 2014. Mapping landslide displacements using Structure from Motion (SfM) and image correlation of multi-temporal UAV photography. Progress in Physical Geography 38, 97-116.DOI: https://doi.org/10.1177/0309133313515293

Manfreda, S., McCabe, M.F., Miller, P.E., Lucas, R., Pajuelo Madrigal, V., Mallinis, G., Ben Dor, E., Helman, D., Estes, L., Ciraolo, G., 2018. On the use of unmanned aerial systems for environmental monitoring. Remote sensing 10, 641.DOI: https://doi.org/10.3390/rs10040641

Marcial-Pablo, M.d.J., Gonzalez-Sanchez, A., Jimenez-Jimenez, S.I., Ontiveros-Capurata, R.E., Ojeda-Bustamante, W., 2019. Estimation of vegetation fraction using RGB and multispectral images from UAV. International journal of remote sensing 40, 420-438.DOI: https://doi.org/10.1080/01431161.2018.1528017

Masjedi, A., 2020. Multi-Temporal Multi-Model Predictive Modelling of Plant Phenotypes. Purdue University Graduate School.

Masjedi, A., Carpenter, N.R., Crawford, M.M., Tuinstra, M.R., 2019. Prediction of Sorghum Biomass Using Uav Time Series Data and Recurrent Neural Networks, Proceedings of the IEEE Conference on Computer Vision and Pattern Recognition Workshops, pp. 0-0. DOI: 10.1109/CVPRW.2019.00327

Meng, L., Liu, H., Zhang, X., Ren, C., Ustin, S., Qiu, Z., Xu, M., Guo, D., 2019. Assessment of the effectiveness of spatiotemporal fusion of multi-source satellite images for cotton yield estimation. Computers and Electronics in Agriculture 162, 44-52.DOI: https://doi.org/10.1016/j.compag.2019.04.001

Miotto, R., Wang, F., Wang, S., Jiang, X., Dudley, J.T., 2018. Deep learning for healthcare: review, opportunities and challenges. Briefings in bioinformatics 19, 1236-1246.DOI: https://doi.org/10.1093/bib/bbx044

Moré, J.J., 1978. The Levenberg-Marquardt algorithm: implementation and theory, Numerical analysis. Springer, pp. 105-116. DOI: https://link.springer.com/content/pdf/10.1007/BFb0067700.pdf

Ndikumana, E., Ho Tong Minh, D., Baghdadi, N., Courault, D., Hossard, L., 2018. Deep recurrent neural network for agricultural classification using multitemporal SAR Sentinel-1 for Camargue, France. Remote Sensing 10, 1217.DOI: https://doi.org/10.3390/rs10081217

Nebiker, S., Lack, N., Abächerli, M., Läderach, S., 2016. LIGHT-WEIGHT MULTISPECTRAL UAV SENSORS AND THEIR CAPABILITIES FOR PREDICTING GRAIN YIELD AND DETECTING PLANT DISEASES. International Archives of the Photogrammetry, Remote Sensing & Spatial Information Sciences 41.DOI: 10.5194/isprsarchives-XLI-B1-963-2016

Nielsen, D.C., Miceli-Garcia, J.J., Lyon, D.J., 2012. Canopy cover and leaf area index relationships for wheat, triticale, and corn. Agronomy journal 104, 1569-1573.DOI: https://doi.org/10.2134/agronj2012.0107n

Nock, C., Taugourdeau, O., Delagrange, S., Messier, C., 2013. Assessing the potential of low-cost 3D cameras for the rapid measurement of plant woody structure. Sensors 13, 16216-16233.DOI: https://doi.org/10.3390/s131216216

Novelli, F., Spiegel, H., Sandén, T., Vuolo, F., 2019. Assimilation of sentinel-2 leaf area index data into a physically-based crop growth model for yield estimation. Agronomy 9, 255.DOI: https://doi.org/10.3390/agronomy9050255

Novikova, I.I., Popova, E.V., Kolesnikov, L.E., Priyatkin, N.S., Kolesnikova, Y.R., 2020. Biological effectiveness of polyfunctional biopreparations in soft wheat cultivation and assessment of crop quality based on NDVI index, BIO Web of Conferences. EDP Sciences, p. 00021. DOI: https://doi.org/10.1051/bioconf/20201800021

NWS, 2016. National Weather Service. National Oceanic and Atmospheric Administration, United States.

O'Malley, T., Bursztein, E., Long, J., Chollet, F., Jin, H., Invernizzi, L., 2019. Keras Tuner.

Pádua, L., Adão, T., Hruška, J., Sousa, J.J., Peres, E., Morais, R., Sousa, A., 2017. Very high resolution aerial data to support multi-temporal precision agriculture information management. Procedia Computer Science 121, 407-414.DOI: https://doi.org/10.1016/j.procs.2017.11.055

Pandey, A., Thapa, K.B., Prasad, R., Singh, K., 2012. General regression neural network and radial basis neural network for the estimation of crop variables of lady finger. Journal of the Indian Society of Remote Sensing 40, 709-715.DOI: https://doi.org/10.1007/s12524-011-0197-9

Pasolli, L., Notarnicola, C., Bruzzone, L., 2012. Multi-objective parameter optimization in support vector regression: General formulation and application to the retrieval of soil moisture from remote sensing data. IEEE Journal of Selected Topics in Applied Earth Observations and Remote Sensing 5, 1495-1508.DOI: 10.1109/JSTARS.2012.2197178

Patrignani, A., Ochsner, T.E., 2015. Canopeo: A powerful new tool for measuring fractional green canopy cover. Agronomy Journal 107, 2312-2320.DOI: https://doi.org/10.2134/agronj15.0150

Paulus, S., Behmann, J., Mahlein, A.-K., Plümer, L., Kuhlmann, H., 2014. Low-cost 3D systems: suitable tools for plant phenotyping. Sensors 14, 3001-3018.DOI: https://doi.org/10.3390/s140203001

Pauly, K., 2014. Applying conventional vegetation vigor indices to UAS-derived orthomosaics: issues and considerations. Proceedings of the International Society of Precision Agriculture (ICPA)

Pellikka, P.K., Lötjönen, M., Siljander, M., Lens, L., 2009. Airborne remote sensing of spatiotemporal change (1955–2004) in indigenous and exotic forest cover in the Taita Hills, Kenya. International Journal of Applied Earth Observation and Geoinformation 11, 221-232.DOI: https://doi.org/10.1016/j.jag.2009.02.002

Pittelkow, C.M., Liang, X., Linquist, B.A., Van Groenigen, K.J., Lee, J., Lundy, M.E., Van Gestel, N., Six, J., Venterea, R.T., Van Kessel, C., 2015a. Productivity limits and potentials of the principles of conservation agriculture. Nature 517, 365.DOI: 10.1038/nature13809

Pittelkow, C.M., Linquist, B.A., Lundy, M.E., Liang, X., Van Groenigen, K.J., Lee, J., Van Gestel, N., Six, J., Venterea, R.T., Van Kessel, C., 2015b. When does no-till yield more? A global meta-analysis. Field Crops Research 183, 156-168.DOI: https://doi.org/10.1016/j.fcr.2015.07.020

Propastin, P., Panferov, O., 2013. Retrieval of remotely sensed LAI using Landsat ETM+ data and ground measurements of solar radiation and vegetation structure: Implication of leaf inclination angle. International Journal of Applied Earth Observation and Geoinformation 25, 38-46.DOI: https://doi.org/10.1016/j.jag.2013.02.006

Raczko, E., Zagajewski, B., 2017. Comparison of support vector machine, random forest and neural network classifiers for tree species classification on airborne hyperspectral APEX images. European Journal of Remote Sensing 50, 144-154.DOI: https://doi.org/10.1080/22797254.2017.1299557

Ritchie, G.L., Bednarz, C.W., Jost, P.H., Brown, S.M., 2007. Cotton growth and development.

Rodriguez-Galiano, V., Sanchez-Castillo, M., Chica-Olmo, M., Chica-Rivas, M., 2015. Machine learning predictive models for mineral prospectivity: An evaluation of neural networks, random forest, regression trees and support vector machines. Ore Geology Reviews 71, 804-818.DOI: https://doi.org/10.1016/j.oregeorev.2015.01.001

Roth, L., Aasen, H., Walter, A., Liebisch, F., 2018. Extracting leaf area index using viewing geometry effects—a new perspective on high-resolution unmanned aerial system photography. ISPRS journal of photogrammetry and remote sensing 141, 161-175.DOI: https://doi.org/10.1016/j.isprsjprs.2018.04.012

Roth, L., Streit, B., 2018. Predicting cover crop biomass by lightweight UAS-based RGB and NIR photography: an applied photogrammetric approach. Precision Agriculture 19, 93-114.DOI: https://doi.org/10.1007/s11119-017-9501-1

Rouse, J., Haas, R., Schell, J., Deering, D., 1974. Monitoring vegetation systems in the Great Plains with ERTS. NASA special publication 351, 309

Rouse Jr, J.W., Haas, R., Schell, J., Deering, D., 1974. Monitoring vegetation systems in the Great Plains with ERTS.

Rudd, J.D., Roberson, G.T., Classen, J.J., 2017. Application of satellite, unmanned aircraft system, and ground-based sensor data for precision agriculture: a review, 2017 ASABE Annual International Meeting. American Society of Agricultural and Biological Engineers, p. 1. DOI: 10.13031/aim.201700272

Ruder, S., 2016. An overview of gradient descent optimization algorithms. arXiv preprint arXiv:1609.04747.DOI: https://arxiv.org/abs/1609.04747

Sapkota, T.B., 2012. Conservation tillage impact on soil aggregation, organic matter turnover and biodiversity, Organic Fertilisation, Soil Quality and Human Health. Springer, pp. 141-160. DOI: https://doi.org/10.1007/978-94-007-4113-3_6

Sargent, D.J., 2001. Comparison of artificial neural networks with other statistical approaches: results from medical data sets. Cancer: Interdisciplinary International Journal of the American Cancer Society 91, 1636-1642.DOI: https://doi.org/10.1002/1097-0142(20010415)91:8

Sayago, S., Bocco, M., 2018. Crop yield estimation using satellite images: comparison of linear and non-linear models. AgriScientia 35, 1-9. DOI: https://doi.org/10.31047/1668.298x.v1.n35.20447

Shaukat, S., Khan, T.M., Shakeel, A., Ijaz, S., 2013. Estimation of best parents and superior cross combinations for yield and fiber quality related traits in upland cotton (Gossypium hirsutum L.). Sci., Tech. and Dev 32, 281-284

Sheykhmousa, M., Mahdianpari, M., Ghanbari, H., Mohammadimanesh, F., Ghamisi, P., Homayouni, S., 2020. Support vector machine vs. random forest for remote sensing image classification: A meta-analysis and systematic review. IEEE Journal of Selected Topics in Applied Earth Observations and Remote Sensing.DOI: 10.1109/JSTARS.2020.3026724

Singh, K.K., Frazier, A.E., 2018. A meta-analysis and review of unmanned aircraft system (UAS) imagery for terrestrial applications. International journal of remote sensing 39, 5078-5098.DOI: https://doi.org/10.1080/01431161.2017.1420941

Singh, R., Semwal, D., Rai, A., Chhikara, R.S., 2002. Small area estimation of crop yield using remote sensing satellite data. International Journal of Remote Sensing 23, 49-56.DOI: https://doi.org/10.1080/01431160010014756

Sorokin, I., Seleznev, A., Pavlov, M., Fedorov, A., Ignateva, A., 2015. Deep attention recurrent Q-network. arXiv preprint arXiv:1512.01693.DOI: https://arxiv.org/abs/1512.01693

Stanton, C., Starek, M.J., Elliott, N., Brewer, M., Maeda, M.M., Chu, T., 2017. Unmanned aircraft system-derived crop height and normalized difference vegetation index metrics for sorghum yield and aphid stress assessment. Journal of Applied Remote Sensing 11, 026035.DOI: https://doi.org/10.1117/1.JRS.11.026035

Staropoli, N., 2016. No-till agriculture offers vast sustainability benefits. So why do many organic farmers reject it?, Genetic Literacy Project

Stewart, J.M., Oosterhuis, D., Heitholt, J.J., Mauney, J.R., 2009. Physiology of cotton. Springer Science & Business Media.

Stroppiana, D., Migliazzi, M., Chiarabini, V., Crema, A., Musanti, M., Franchino, C., Villa, P., 2015. Rice yield estimation using multispectral data from UAV: A preliminary experiment in northern Italy, Geoscience and Remote Sensing Symposium (IGARSS), 2015 IEEE International. IEEE, pp. 4664-4667. DOI: 10.1109/IGARSS.2015.7326869

Sun, C., Shrivastava, A., Singh, S., Gupta, A., 2017. Revisiting unreasonable effectiveness of data in deep learning era, Proceedings of the IEEE international conference on computer vision, pp. 843-852. DOI: 10.1109/ICCV.2017.97

Sun, J., Di, L., Sun, Z., Shen, Y., Lai, Z., 2019. County-level soybean yield prediction using deep CNN-LSTM model. Sensors 19, 4363.DOI: https://doi.org/10.3390/s19204363

Swain, K.C., Jayasuriya, H.P., Salokhe, V.M., 2007. Suitability of low-altitude remote sensing images for estimating nitrogen treatment variations in rice cropping for precision agriculture adoption. Journal of Applied Remote Sensing 1, 013547.DOI: https://doi.org/10.1117/1.2824287

Swain, K.C., Thomson, S.J., Jayasuriya, H.P., 2010. Adoption of an unmanned helicopter for low-altitude remote sensing to estimate yield and total biomass of a rice crop. Transactions of the ASABE 53, 21-27.DOI: 10.13031/2013.29493

Tattaris, M., Reynolds, M.P., Chapman, S.C., 2016. A direct comparison of remote sensing approaches for high-throughput phenotyping in plant breeding. Frontiers in plant science 7, 1131.DOI: https://doi.org/10.3389/fpls.2016.01131

Torres-Sánchez, J., Peña, J.M., de Castro, A.I., López-Granados, F., 2014. Multi-temporal mapping of the vegetation fraction in early-season wheat fields using images from UAV. Computers and Electronics in Agriculture 103, 104-113.DOI: https://doi.org/10.1016/j.compag.2014.02.009

Tri, N.C., Duong, H.N., Van Hoai, T., Van Hoa, T., Nguyen, V.H., Toan, N.T., Snasel, V., 2017. A novel approach based on deep learning techniques and UAVs to yield assessment of paddy fields, Knowledge and Systems Engineering (KSE), 2017 9th International Conference on. IEEE, pp. 257-262. DOI: 10.1109/KSE.2017.8119468

Triplett, G., Dick, W.A., 2008. No-tillage crop production: a revolution in agriculture! Agronomy journal 100, S-153-S-165

Trout, T.J., Johnson, L.F., Gartung, J., 2008. Remote sensing of canopy cover in horticultural crops. HortScience 43, 333-337.DOI: https://doi.org/10.21273/HORTSCI.43.2.333

Tu, J.V., 1996. Advantages and disadvantages of using artificial neural networks versus logistic regression for predicting medical outcomes. Journal of clinical epidemiology 49, 1225-1231.DOI: https://doi.org/10.1016/S0895-4356(96)00002-9

Tzeng, E., Hoffman, J., Saenko, K., Darrell, T., 2017. Adversarial discriminative domain adaptation, Proceedings of the IEEE conference on computer vision and pattern recognition, pp. 7167-7176. DOI: 10.1109/CVPR.2017.316

Valderrama-Landeros, L., Flores-de-Santiago, F., Kovacs, J., Flores-Verdugo, F., 2018. An assessment of commonly employed satellite-based remote sensors for mapping mangrove species in Mexico using an NDVI-based classification scheme. Environmental monitoring and assessment 190, 23.DOI: https://doi.org/10.1007/s10661-017-6399-z

Verrelst, J., Muñoz, J., Alonso, L., Delegido, J., Rivera, J.P., Camps-Valls, G., Moreno, J., 2012. Machine learning regression algorithms for biophysical parameter retrieval: Opportunities for Sentinel-2 and-3. Remote Sensing of Environment 118, 127-139.DOI: https://doi.org/10.1016/j.rse.2011.11.002

Wang, A., Lu, J., Cai, J., Cham, T.-J., Wang, G., 2015. Large-margin multi-modal deep learning for RGB-D object recognition. IEEE Transactions on Multimedia 17, 1887-1898.DOI: 10.1109/TMM.2015.2476655

Wang, A.X., Tran, C., Desai, N., Lobell, D., Ermon, S., 2018. Deep transfer learning for crop yield prediction with remote sensing data, Proceedings of the 1st ACM SIGCAS Conference on Computing and Sustainable Societies, pp. 1-5. DOI: https://doi.org/10.1145/3209811.3212707

Wang, Q., Li, B., Xiao, T., Zhu, J., Li, C., Wong, D.F., Chao, L.S., 2019. Learning deep transformer models for machine translation. arXiv preprint arXiv:1906.01787.DOI: https://arxiv.org/abs/1906.01787

Weiss, M., Baret, F., Smith, G., Jonckheere, I., Coppin, P., 2004. Review of methods for in situ leaf area index (LAI) determination: Part II. Estimation of LAI, errors and sampling. Agricultural and forest meteorology 121, 37-53.DOI: https://doi.org/10.1016/j.agrformet.2003.08.001

Weiss, M., Jacob, F., Duveiller, G., 2020. Remote sensing for agricultural applications: A meta-review. Remote Sensing of Environment 236, 111402.DOI: https://doi.org/10.1016/j.rse.2019.111402

Were, K., Bui, D.T., Dick, Ø.B., Singh, B.R., 2015. A comparative assessment of support vector regression, artificial neural networks, and random forests for predicting and mapping soil organic carbon stocks across an Afromontane landscape. Ecological Indicators 52, 394-403.DOI: https://doi.org/10.1016/j.ecolind.2014.12.028

Westoby, M., Brasington, J., Glasser, N., Hambrey, M., Reynolds, J., 2012. 'Structure-from-Motion'photogrammetry: A low-cost, effective tool for geoscience applications. Geomorphology 179, 300-314.DOI: https://doi.org/10.1016/j.geomorph.2012.08.021

Woebbecke, D.M., Meyer, G.E., Von Bargen, K., Mortensen, D., 1995. Color indices for weed identification under various soil, residue, and lighting conditions. Transactions of the ASAE 38, 259-269.DOI: 10.13031/2013.27838

Xiang, H., Tian, L., 2011. Development of a low-cost agricultural remote sensing system based on an autonomous unmanned aerial vehicle (UAV). Biosystems engineering 108, 174-190.DOI: https://doi.org/10.1016/j.biosystemseng.2010.11.010

Xiao-Hua, Y., Fu-Min, W., Huang, J.-F., Jian-Wen, W., Ren-Chao, W., Zhang-Quan, S., Xiu-Zhen, W., 2009. Comparison between radial basis function neural network and regression model for estimation of rice biophysical parameters using remote sensing. Pedosphere 19, 176-188.DOI: https://doi.org/10.1016/S1002-0160(09)60107-7

Xu, R., Li, C., Paterson, A.H., 2019. Multispectral imaging and unmanned aerial systems for cotton plant phenotyping. PloS one 14, e0205083.DOI: https://doi.org/10.1371/journal.pone.0205083

Yang, C., 2018. High resolution satellite imaging sensors for precision agriculture. Frontiers of Agricultural Science and Engineering 5, 393-405.DOI: 10.15302/J-FASE-2018226

Yang, C., Everitt, J.H., Du, Q., Luo, B., Chanussot, J., 2012. Using high-resolution airborne and satellite imagery to assess crop growth and yield variability for precision agriculture. Proceedings of the IEEE 101, 582-592.DOI: 10.1109/JPROC.2012.2196249

Yang, Y., Cao, C., Pan, X., Li, X., Zhu, X., 2017. Downscaling land surface temperature in an arid area by using multiple remote sensing indices with random forest regression. Remote Sensing 9, 789.DOI: 10.1109/JPROC.2012.2196249

Yap, B.W., Sim, C.H., 2011. Comparisons of various types of normality tests. Journal of Statistical Computation and Simulation 81, 2141-2155.DOI: https://doi.org/10.1080/00949655.2010.520163

Yi, F., Moon, I., 2012. Image segmentation: A survey of graph-cut methods, 2012 international conference on systems and informatics (ICSAI2012). IEEE, pp. 1936-1941. DOI: 10.1109/ICSAI.2012.6223428

You, J., Li, X., Low, M., Lobell, D., Ermon, S., 2017. Deep gaussian process for crop yield prediction based on remote sensing data, Thirty-First AAAI conference on artificial intelligence. DOI: https://dl.acm.org/doi/10.5555/3298023.3298229

Yu, N., Li, L., Schmitz, N., Tian, L.F., Greenberg, J.A., Diers, B.W., 2016. Development of methods to improve soybean yield estimation and predict plant maturity with an unmanned aerial vehicle based platform. Remote Sensing of Environment 187, 91-101.DOI: https://doi.org/10.1016/j.rse.2016.10.005

Yue, J., Yang, G., Tian, Q., Feng, H., Xu, K., Zhou, C., 2019. Estimate of winter-wheat above-ground biomass based on UAV ultrahigh-ground-resolution image textures and vegetation indices. ISPRS Journal of Photogrammetry and Remote Sensing 150, 226-244.DOI: https://doi.org/10.1016/j.isprsjprs.2019.02.022

Zaremba, W., Sutskever, I., Vinyals, O., 2014. Recurrent neural network regularization. arXiv preprint arXiv:1409.2329.DOI: https://arxiv.org/abs/1409.2329

Zhang, C., Kovacs, J.M., 2012. The application of small unmanned aerial systems for precision agriculture: a review. Precision agriculture 13, 693-712.DOI: https://doi.org/10.1007/s11119-012-9274-5

Zhang, Y., Liu, G., Dong, H., Li, C., 2021. Waterlogging stress in cotton: damage, adaptability, alleviation strategies, and mechanisms. The Crop Journal 9, 257-270.https://doi.org/10.1016/j.cj.2020.08.005S

Zhao, X., Jia, Y., Li, A., Jiang, R., Song, Y., 2020. Multi-source knowledge fusion: a survey. World Wide Web 23, 2567-2592.DOI: https://doi.org/10.1007/s11280-020-00811-0

Zhao, X., Liu, S.-L., Pu, C., Zhang, X.-Q., Xue, J.-F., Ren, Y.-X., Zhao, X.-L., Chen, F., Lal, R., Zhang, H.-L., 2017. Crop yields under no-till farming in China: A meta-analysis. European Journal of Agronomy 84, 67-75.DOI: https://doi.org/10.1016/j.eja.2016.11.009

Zheng, H., Cheng, T., Li, D., Zhou, X., Yao, X., Tian, Y., Cao, W., Zhu, Y., 2018. Evaluation of RGB, color-infrared and multispectral images acquired from unmanned aerial systems for the estimation of nitrogen accumulation in rice. Remote Sensing 10, 824.DOI: https://doi.org/10.3390/rs10060824

Zhou, X., Zheng, H., Xu, X., He, J., Ge, X., Yao, X., Cheng, T., Zhu, Y., Cao, W., Tian, Y., 2017. Predicting grain yield in rice using multi-temporal vegetation indices from UAV-based multispectral and digital imagery. ISPRS Journal of Photogrammetry and Remote Sensing 130, 246-255.DOI: https://doi.org/10.1016/j.isprsjprs.2017.05.003

Zhou, X., Zhu, X., Dong, Z., Guo, W., 2016. Estimation of biomass in wheat using random forest regression algorithm and remote sensing data. The Crop Journal 4, 212-219.DOI: https://doi.org/10.1016/j.cj.2016.01.008